

# Modular Architectures and Entanglement Schemes for Error-Corrected Distributed Quantum Computation

Siddhant Singh,<sup>1,2,\*</sup> Fenglei Gu,<sup>1,\*</sup> Sébastien de Bone,<sup>1,3</sup> Eduardo Villaseñor,<sup>4</sup> David Elkouss,<sup>1,2,†</sup> and Johannes Borregaard<sup>1,5,‡</sup>

<sup>1</sup>*QuTech, Delft University of Technology, Lorentzweg 1, 2628 CJ Delft, The Netherlands*

<sup>2</sup>*Networked Quantum Devices Unit, Okinawa Institute of Science and Technology Graduate University, Okinawa, Japan*

<sup>3</sup>*QuSoft, CWI, Science Park 123, 1098 XG Amsterdam, The Netherlands*

<sup>4</sup>*CSIRO, Research Way, Clayton, 3168 Victoria, Australia*

<sup>5</sup>*Department of Physics, Harvard University, Cambridge, Massachusetts 02138, USA*

(Dated: August 7, 2024)

Connecting multiple smaller qubit modules by generating high-fidelity entangled states is a promising path for scaling quantum computing hardware. The performance of such a modular quantum computer is highly dependent on the quality and rate of entanglement generation. However, the optimal architectures and entanglement generation schemes are not yet established. Focusing on modular quantum computers with solid-state quantum hardware, we investigate a distributed surface code's error-correcting threshold and logical failure rate. We consider both emission-based and scattering-based entanglement generation schemes for the measurement of non-local stabilizers. Through quantum optical modeling, we link the performance of the quantum error correction code to the parameters of the underlying physical hardware and identify the necessary parameter regime for fault-tolerant modular quantum computation. In addition, we compare modular architectures with one or two data qubits per module. We find that the performance of the code depends significantly on the choice of entanglement generation scheme, while the two modular architectures have similar error-correcting thresholds. For some schemes, thresholds nearing the thresholds of non-distributed implementations ( $\sim 0.4\%$ ) appear feasible with future parameters.

## I. INTRODUCTION

In the current pursuit of large-scale quantum computation, two major obstacles are encountered: hardware noise [1–4] and scalability limitations [5–7]. Error-corrected [8–10] modular quantum computers [11, 12] offer a promising route to overcome both these challenges. A modular quantum computer consists of individual computing modules with separate control, which are linked together by means of quantum entanglement [13–17]. This simplifies the engineering challenge of scaling the number of qubits and offers more flexibility in the connectivity of the device [18]. Modular architectures have been proposed for a plethora of quantum computing hardware such as superconducting qubits [19, 20], neutral atoms [21, 22] and color centers [23–25]. However, several outstanding questions about operating distributed quantum error-correction (QEC) codes across a modular quantum computer remain. Previous work has hinted that the performance of a distributed QEC code heavily depends on the degree of modularity [26] and the specific choice of quantum entanglement generation protocol [25]. Given the many suitable protocols for entanglement generation [27], as well as specific choice of modular architecture and QEC codes [28, 29], amounts to a largely unexplored space of optimal modular computing designs for specific quantum hardware.

In this article, we explore this space for quantum hardware with efficient spin-photon interfaces such as defect color centers in diamond and silicon [30–41] by investigating the performance of a distributed toric surface code [42–45] across two types of modular architectures considering both emission [46] and scattering based [37, 47] entanglement generation schemes. We consider both a fully modular architecture with a single data qubit per module and one with two data qubits per module and demonstrate significant differences in code performance for the two depending on the system parameters. We go beyond the generic circuit-level noise model and develop hardware-tailored noise models that allow us to link the QEC performance directly to the physical parameters of the quantum hardware and specific choice of entanglement scheme. From this investigation, we specify the requirements of key parameters such as qubit coherence times, photonic link efficiency, and quality of the spin-photon interface for the existence of circuit-level noise code threshold and break-even point where the QEC suppresses errors beyond the physical error rates. While we find that near-term experimental parameters are sufficient to realize fault-tolerant quantum computation, modest future improvements can lead to QEC thresholds as high as  $\sim 0.4\%$ , which is comparable to the thresholds found for monolithic architectures [48].

The article is organized as follows. In Sec. II, we describe the modular architectures inspired by the toric surface code. Next, in Sec. III, we describe the theory and analytical model of the entanglement generation schemes, including emission-based and scattering-based schemes. We construct detailed physical models for the

\* These authors contributed equally to this work

† david.elkouss@oist.jp

‡ borregaard@fas.harvard.edu

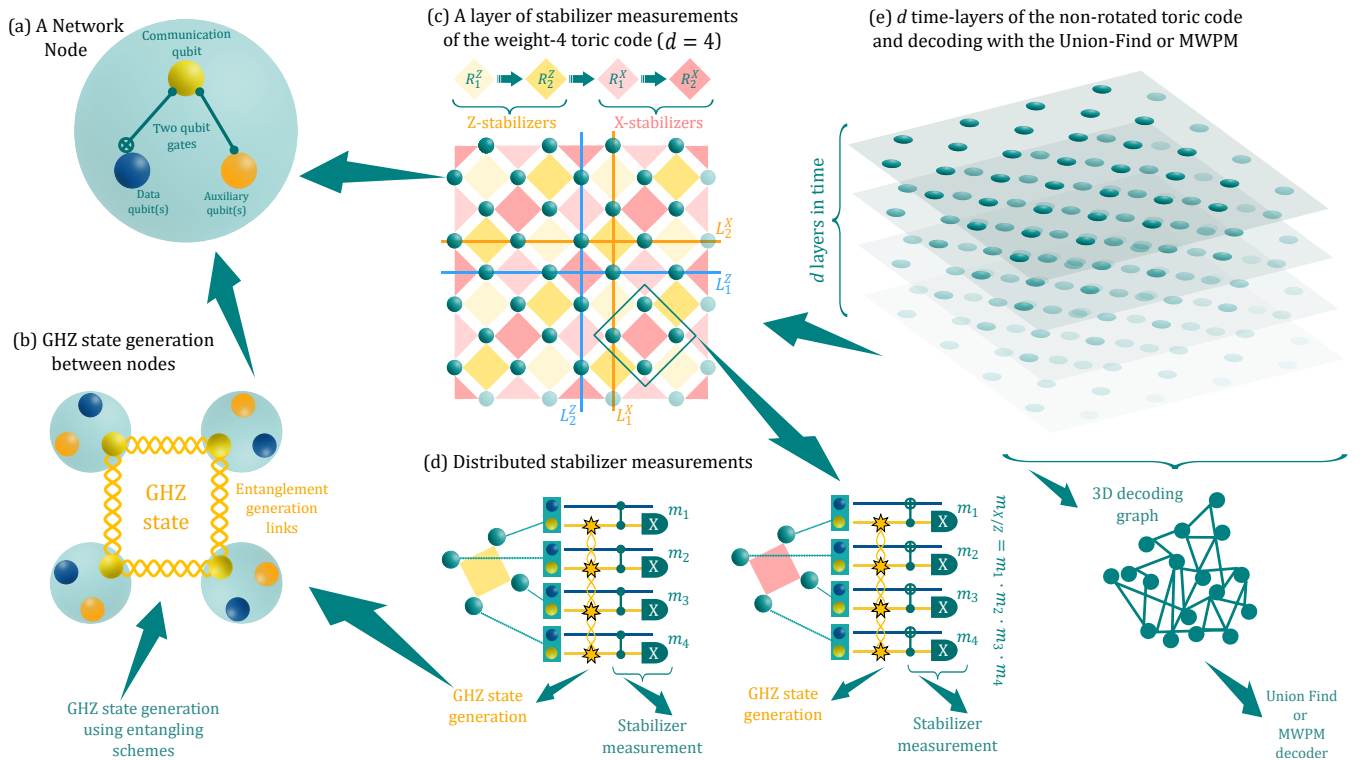


FIG. 1. Weight-4 architecture (one data qubit per node). (a) The structure of a module. It consists of a single communication qubit that allows for optical connection to the other modules and some memory qubits acting as either data qubits of the code or auxiliary qubits for the stabilizer measurements. Stabilizers between modules are read out using multi-qubit GHZ states, as shown schematically in (b). (c) One round of  $Z$  and  $X$  type stabilizer measurements, each divided into two sub-rounds. The sequence of the stabilizer sub-rounds is also shown, along with a choice for the logical operators for the two encoded logical qubits in the toric code ( $L_{1,2}^{X,Z}$ ). (d) The distributed stabilizer measurement circuits of the  $Z$  and  $X$  stabilizers, where a GHZ state is generated upon demand (indicated by stars) and used to measure the joint parity  $ZZZZ$  or  $XXXX$  on the stabilizer data qubits via the application of local controlled- $Z/X$  gate. The outcome of the stabilizer measurement is the joint parity outcome from the four measurements, i.e.,  $m_{X/Z} = m_1 \cdot m_2 \cdot m_3 \cdot m_4$ . (e) The stabilizer measurements are repeated  $d$  times where  $d$  is the distance of the square toric code. These  $d$  layers constitute one full QEC cycle, and all syndrome data is then sent to the decoder, whereafter suitable corrections are applied to the qubits.

hardware performance in Sec. IV. Finally, we describe the results on distributed code error thresholds and architecture implementation in Sec. V.

## II. DISTRIBUTED SURFACE CODE ARCHITECTURES

We consider a setup where each module of the computing architecture consists of a single communication qubit and a few memory qubits, as shown in Fig. 1(a). The modules are arranged on a square lattice, and the communication qubits can establish entanglement with the nearest neighboring modules through optical links. We will assign one or two of the memory qubits in a module as data qubits of the code, while additional memory qubits are assigned as auxiliary qubits that can be utilized for the stabilizer measurements [25].

Two qubit interactions are allowed between the communication and memory qubits within the same node.

We do not consider direct two-qubit gates between the memory qubits. Such gates have to be effectively mediated via the communication qubit. The same argument applies to the measurement; only the communication qubit can be directly measured. For the other memory qubit measurement, one has to swap the memory qubit state to the communication qubit and carry out the measurement. This model is tailored to a broad range of quantum hardware based on defect color centers such as Nitrogen-Vacancy (NV) [49], Silicon-Vacancy (SiV) [32–35, 37], Tin-Vacancy (SnV) [38–40], and Silicon defect centers [24], where the electronic spin states of the defect are optically addressable and can couple through a dipolar interaction to nearby nuclear memory spins.

The topological non-rotated toric surface code [19, 45, 50] that we consider in this work requires measurement of weight-4 stabilizers between neighboring data qubits. We do not consider the planar surface code explicitly, as its threshold performance is similar. The fully distributed implementation can be achieved in a non-fault-tolerant

way through a single auxiliary qubit interacting sequentially with the four data qubits via gate teleportation [51]. Such a scheme is, however, sub-optimal in our case since it requires repeated entanglement distribution between a single module and its neighbors while keeping the auxiliary qubit coherent, which is challenging in solid-state hardware [52–54]. Instead, we consider schemes where multi-qubit GHZ states are created between the modules either through direct GHZ state generation or fusion of Bell pairs, which lowers the coherence requirements of the auxiliary qubits. Furthermore, creating a weight- $n$  GHZ state requires only  $n - 1$  Bell pairs and fewer two-qubit gates and measurements for the stabilizer, in contrast to the gate-teleportation protocol. For the architecture with one data qubit per module, we require the generation of 4-qubit GHZ states, while 3-qubit GHZ states are needed when 2 data qubits are hosted per module. We will refer to these as the weight-4 (WT4) and weight-3 (WT3) architectures.

### Stabilizer measurements

Since each module only contains one communication qubit, it is not possible to measure all the stabilizers simultaneously. This constraint results in a checkerboard pattern of stabilizer measurement sub-rounds (each of X and Z types), which differs for the WT4 and WT3 architectures.

For the WT4 architecture, each X and Z-type stabilizer is divided into two sub-rounds, resulting in a four-sequence QEC cycle (see Fig. 1). The distributed implementation of the code is fault-tolerant by construction, given the fault-tolerant creation of the GHZ states, as there is no propagation of errors (hook errors) [55] from one node to another.

For the WT3 architecture, the modules are arranged obliquely on the code background array, such that one module contributes two data qubits on the code and exactly three modules span each stabilizer. We consider the even-distance (for each logical operator) WT3 toric code, as this allows all the modules to be the same. The bare WT3 architecture is not fault-tolerant w.r.t. hook errors, as there can be weight-2 error propagation from single qubits errors within each node due to local two-qubit controlled gates. A flagged version of the WT3 stabilizer measurement circuit could be considered to detect and correct for these hook errors [56] but for simplicity, we do not consider the flagged here.

The topology of the WT3 architecture means that four sub-rounds for each stabilizer type (X, Z) are required, resulting in an 8-sequence QEC cycle (see Fig. 2). The WT3 architecture, therefore, comes at a trade-off of longer QEC cycle times versus the lower weight of the GHZ state relative to the WT4 architecture. Also, the WT3 architecture has half the number of modules used in the WT4 architecture. The non-simultaneous sub-round stabilizer measurement sequence also leads to

additional errors between these sub-rounds for both architectures. This is explained in more detail in the App. C.

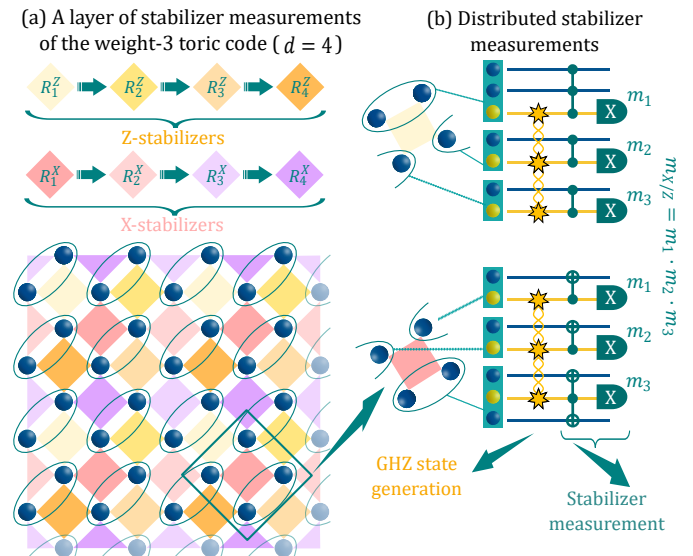


FIG. 2. Weight-3 surface code architecture layout, for distance  $d = 4$ . The structure of one round of stabilizer measurements, consisting of four sub-rounds for both the X and Z type stabilizers, is shown in (a). Logical qubits of the code are the same as for the WT4 architecture (see Fig. 1(c)). The stabilizer measurement circuits are shown in (b), where we now have two data qubits in one node for each stabilizer type. The notation is the same as in Fig. 1

### Cut-off times

The GHZ state generation is probabilistic for the distributed architecture due to photon loss and imperfect Bell measurements. To maintain the stabilizer synchronicity, we consider a cut-off time ( $t_{\text{cut}}$ ) that caps the maximum time duration allowed for GHZ state generation between the modules before stabilizers are measured. Suppose some stabilizers' GHZ state generation is unsuccessful within this time window. In that case, we abandon the stabilizer measurement and substitute the value from the latest successful stabilizer measurement before carrying on with the next sub-round of the stabilizer measurements. A low  $t_{\text{cut}}$  will lead to less syndrome measurement information and affect the detection of errors, and a larger  $t_{\text{cut}}$  will lead to more noise accumulation due to decoherence of the qubits while idle. Therefore, we optimize  $t_{\text{cut}}$  to find the highest error-correcting threshold of the code.

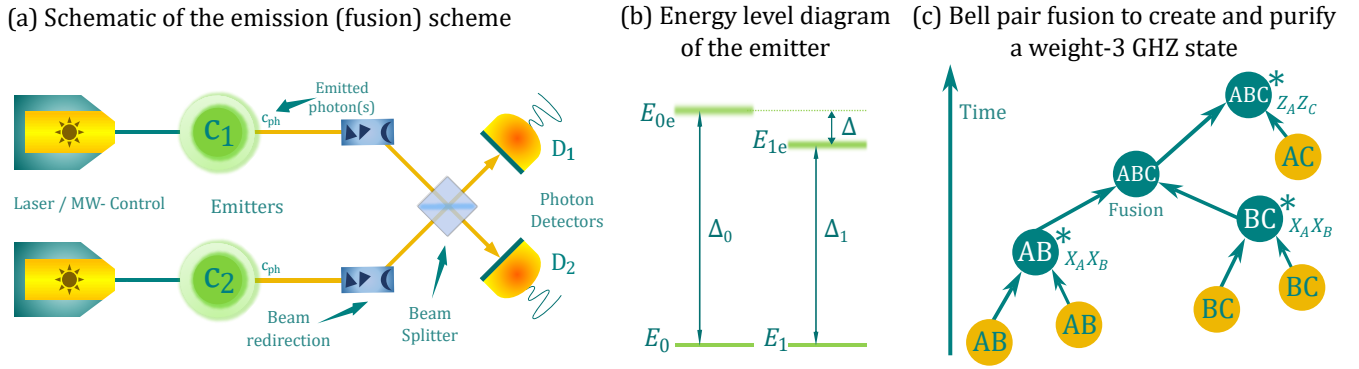


FIG. 3. Emission-based scheme. (a) An optical setup with two emitters as communication qubits can be initialized in an emitter-photon entangled state. Then, the emitted photons ( $c_{\text{ph}}$ ) are sent to a middle station where an optical Bell measurement is performed using a balanced beam splitter and single photon detection. The detection of an early and a late photon at the detectors successfully heralds a Bell pair between the two emitters ( $c_i$ ). (b) The energy levels of the photon-emitter system. The emitter has two sets of independent transitions:  $E_0 \leftrightarrow E_{0e}$  and  $E_1 \leftrightarrow E_{1e}$  with transition frequencies  $\Delta_0$  and  $\Delta_1$ , respectively. Here, state  $|1\rangle$  is the bright state that emits a photon upon excitation. (c) An example of a GHZ state fusion protocol with distillation used to create a high-fidelity WT3 GHZ state presented as a tree graph. Events in yellow indicate Bell pair generation between the respective modules, while the teal-colored arrows labeled with a multi-Pauli operator indicate a distillation event by measuring that operator. Modules with a teal color indicate the distilled entangled state.

### Decoherence model for QEC cycles

In addition to the circuit-level noise, we adopt a continuous decoherence model of all qubits, where the probability to decohere (modeled as an effective depolarizing channel) is  $1 - \exp(-t/T^{\text{dec}})$  where  $t$  measures time and  $T^{\text{dec}}$  is the characteristic decoherence time. Importantly, we consider two different decoherence times depending on whether a module is active in an entanglement generation attempt or not. During an entanglement generation attempt, the memory qubits have a decoherence time of  $T_{\text{link}}^{\text{dec}}$ . When there is no active entanglement generation attempts in a module, all qubits (including the communication qubit) have a decoherence time of  $T_{\text{idle}}^{\text{dec}}$ . In general,  $T_{\text{idle}}^{\text{dec}} \geq T_{\text{link}}^{\text{dec}}$  for the solid-state hardware considered in this work [52–54]. Sec. IV provides more details on this noise model.

## III. GHZ-STATE GENERATION

In this section, we describe the emission— and scattering-based entanglement generation schemes we consider for generating high-fidelity GHZ states between the modules. Each scheme can be adapted to generate either 4-qubit or 3-qubit GHZ states.

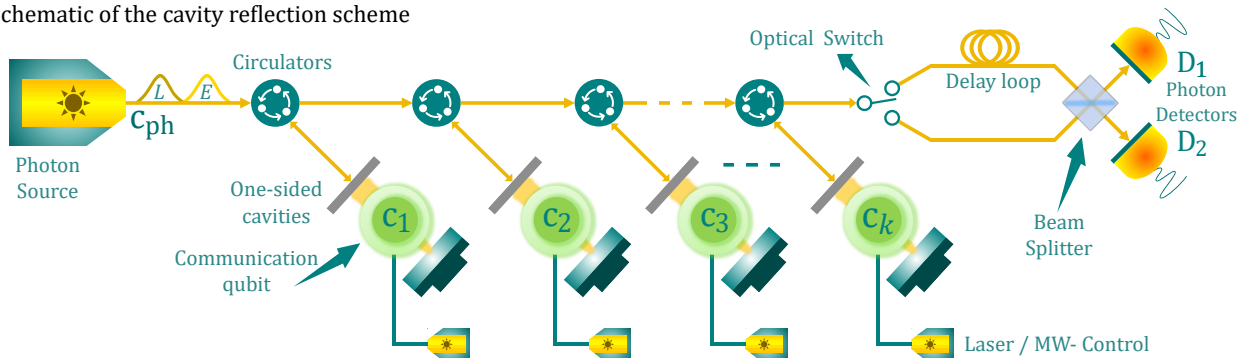
### A. Emission-based scheme

As an emission-based scheme, we consider the single-click [57] and double-click (Barrett-Kok [58]) protocols. For the near-term parameters, we use the single-click protocol. For the boosted future parameters, we use

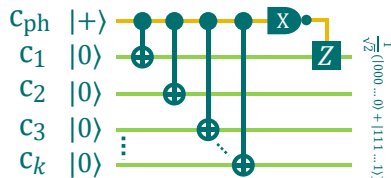
the double-click protocol for optimal performance (see Sec. IV for details on the parameters). We briefly describe only the double-click protocol here, with full analytical details in App. D. In this protocol, spin-photon entanglement is first created between two communication qubits (emitters) through selective excitation of only one of the qubit states, e.g.,  $|1\rangle$ . The communication qubits are initially prepared in an equal superposition  $(|0\rangle + |1\rangle)/\sqrt{2}$ . A laser pulse then makes the transformation  $|1\rangle \rightarrow |1\rangle|1\rangle_{\text{ph}}$ ,  $|0\rangle \rightarrow |0\rangle|0\rangle_{\text{ph}}$  by selectively exciting population in the  $|1\rangle$  (bright) state to an excited state which relaxes back to the  $|1\rangle$  state through emission of a photon,  $|1\rangle_{\text{ph}}$ . The other qubit state is not excited and thus results in a photonic vacuum state,  $|0\rangle_{\text{ph}}$ .

After the first excitation pulse, the emitted photons from each emitter are combined on a balanced beam splitter and detected. If a single click is registered, it results in an entangled state of the emitters  $(|01\rangle \pm |10\rangle)/\sqrt{2}$  for the emitter qubits, where the sign depends upon which photon detector clicked. However, in the presence of photon loss, there is a mixed state with the contribution from the bright state  $|11\rangle\langle 11|$ . The emitter qubit states are flipped via  $X$  gates to remove this component. Another selective excitation pulse and photon measurement is performed, leading to the creation of an entangled state of the form  $(|0\rangle|1\rangle + |1\rangle|0\rangle)/\sqrt{2}$ . Note that the successful Bell measurement is heralded by detecting one early and one late photon. The success probability ( $P_{\text{succ}}^{\text{link}}$ ) of creating a Bell pair link between two modules is quadratically dependent upon the effective photon detection probability, which includes both the collection efficiency of the photons, propagation loss, and inefficient single photon detectors. In addition, there are several imperfections in realistic hardware, such as unwanted photon emission from

(a) Schematic of the cavity reflection scheme



(b) Equivalent quantum circuit



(c) CNOT gate via cavity scattering



(d) Energy diagram of optical cavity and qubit

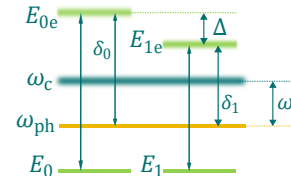


FIG. 4. Principles of the reflecting protocol. (a) System setup of the reflection protocol. It contains a series of atoms, each embedded within a single-side cavity. The fibers and circulators guide the photon to interact with each atom-cavity system successively. The delay loop, beam splitter, and photon detectors are used to detect the photonic qubit in the X basis. (b) Quantum circuit that the reflecting protocol implements. It contains CNOT gates and a photon measurement in its X basis. (c) Physical implementation for the CNOT gate. It contains four steps, including scattering the photon of the two time bins and implementing Hadamard gates on the atom. (d) The energy levels of the photon-atom-cavity system. The spin has two sets of independent transitions coupled to the input photon:  $E_0 \leftrightarrow E_{0e}$  and  $E_1 \leftrightarrow E_{1e}$ .  $\omega_c$ : cavity resonance frequency;  $\omega_{ph}$ : input photon frequency.

the  $|0\rangle$  state and two-photon emissions. We include this in our modeling by considering a four-level system with two ground states  $|0\rangle, |1\rangle$ , and excited states  $|0\rangle_e$  and  $|1\rangle_e$  with possible optical transitions  $|0\rangle \leftrightarrow |0\rangle_e$  and  $|1\rangle \leftrightarrow |1\rangle_e$  as shown in Fig. 3(b). We refer to App. D for in-depth details on the full analytical model of the emission-based scheme with imperfections, including circuit-level noise for the local gates acting on the emitters.

The Bell pairs generated between pairs of modules can be fused into GHZ states through local two-qubit gates and measurements [25]. Due to imperfections of both the Bell states and the local gate operations, it is necessary to employ distillation protocols to boost the final fidelity of the GHZ state. Similar to Ref. [25], we optimize over various distillation protocols where additional Bell pairs are used to increase the final GHZ state fidelity. Notably, we only consider distillation protocols where, at most, two auxiliary memory qubits per module are available. Details of this are presented in App. D 4.

As an example (shown in Fig. 3(c)), we consider how to generate a GHZ state between three modules, A, B, and C, while using auxiliary Bell pairs along the way to increase fidelity. First, a Bell pair,  $|\Phi^+\rangle_{AB}$ , is generated between the communication qubits of modules A and B and swapped to memory qubits within each module through local two-qubit gates. Another Bell pair  $|\Phi^+\rangle_{AB}$  is generated and is used to distill the prior one by measuring the

stabilizer  $X_A X_B$  (distilled state denoted by  $*$ ). Similarly, a Bell pair,  $|\Phi^+\rangle_{BC}$ , is generated between modules B and C and distilled. Finally, a CNOT operation is applied between the two Bell pair qubits at module B, followed by a measurement of one of the qubits (the communication qubit), which results in a three-qubit GHZ state  $|\Phi^+\rangle_{ABC}$  between A-B-C up to a local single qubit rotation. This GHZ state can be further distilled via a Bell pair  $|\Phi^+\rangle_{AC}$ .

## B. Reflection scheme

The emission-based protocol requires generations of Bell pairs in a sequence, intra-module two-qubit gates on the memory qubits, and multiple photonic measurements. These requirements present a significant time overhead in the QEC cycle with corresponding memory requirements on the data qubits. In particular, the spin-spin interactions [59] used to implement local two-qubit gates can be several orders of magnitude slower than the optical pulses and single-qubit gates for defect-based hardware [60]. Because of these drawbacks, we consider scattering-based entangling schemes where spin-dependent reflection/transmission is possible. This can be realized with a qubit-coupled waveguide/cavity system with Group-IV defect centers in diamond [61] and

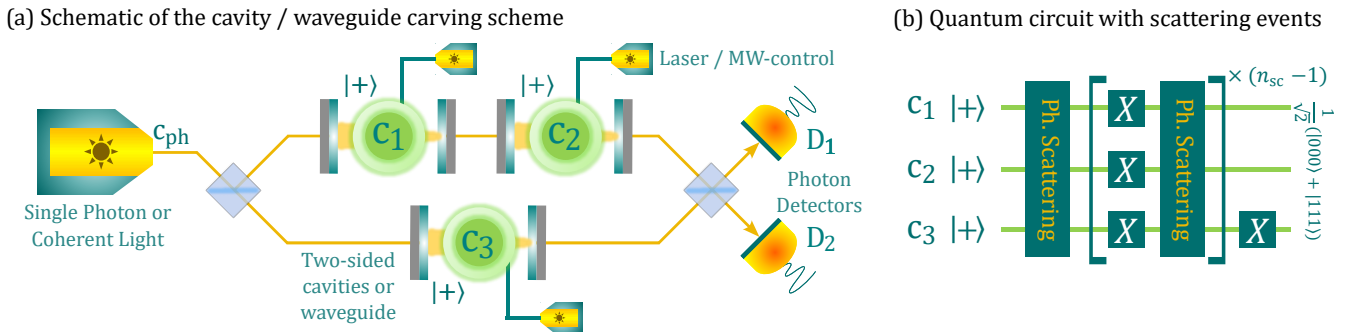


FIG. 5. Principle of the carving protocol. (a) System setup of the carving protocol. It consists of spins embedded inside a two-sided cavity (or waveguide), a light source, beam-splitters, and photon detectors. (b) The operating sequence of the carving protocol. All the spins are initialized in  $|+\rangle$  states. The operating sequence consists of scatterings of single photons through the optical circuit and NOT gates implemented on spins between each scattering.

silicon-based defect centers [62, 63].

Unlike the emission-based schemes, the reflection scheme allows for the direct generation of an inter-module GHZ state without requiring (slow) local two-qubit gate operations and measurements. In particular, a direct spin-photon CNOT operation can be achieved by reflecting a time-bin encoded single photonic qubit from a single-sided cavity with a strongly coupled communication qubit [64, 65]. Ideally, the photon is prepared in a state  $\frac{1}{\sqrt{2}}(|e\rangle_{\text{ph}} + |l\rangle_{\text{ph}})$  while the communication qubit is prepared in  $|0\rangle$ . Assuming that the  $|0\rangle$  state does not couple to the cavity field and that the incoming photon is on resonance with the cavity, scattering of the early photon result in the transformation  $\frac{1}{\sqrt{2}}(|e\rangle_{\text{ph}} + |l\rangle_{\text{ph}})|0\rangle \rightarrow \frac{1}{\sqrt{2}}(-|e\rangle_{\text{ph}} + |l\rangle_{\text{ph}})|0\rangle$ , i.e. the photon is reflected from the cavity with a  $\pi$ -phase shift. Before the scattering of the late photon, a Hadamard gate is applied to the communication qubit, transforming  $|0\rangle$  into  $\frac{1}{\sqrt{2}}(|0\rangle + |1\rangle) = |+\rangle$ . If the  $|1\rangle$  state is strongly coupled to the cavity field, scattering of the late photon will result in the transformation,  $\frac{1}{\sqrt{2}}(-|e\rangle_{\text{ph}} + |l\rangle_{\text{ph}})|+\rangle \rightarrow \frac{1}{\sqrt{2}}(|e\rangle_{\text{ph}}|+\rangle + |l\rangle_{\text{ph}}|-\rangle)$  up to a global phase where  $|-\rangle = \frac{1}{\sqrt{2}}(|0\rangle - |1\rangle)$ . This is because scattering from the  $|1\rangle$  state will reflect the photon without a  $\pi$ -phase shift in the strongly coupled regime. A final Hadamard gate on the communication qubit taking  $|+\rangle \rightarrow |0\rangle$  and  $|-\rangle \rightarrow |1\rangle$  completes the CNOT operation. By reflecting a single photonic qubit with consecutive modules, this scheme allows for the direct generation of a GHZ state as shown schematically in Fig. 4. The generation is heralded by a final measurement of the photonic qubit in the  $X$ -basis, which can be achieved with photonic switching and a fiber delay.

As with the emission-based scheme, we include various hardware imperfections in our modeling of the reflection-based scheme, such as photon loss, finite cavity coupling, and unwanted coupling of the  $|0\rangle$  state considering a four-level scheme as in Fig. 4(d). The details of our model are provided in App. E. However, note that we assume a

near-perfect single-photon source in our simulations.

### C. Carving scheme

The reflection scheme requires optical circulators to separate the incoming and outgoing fields from the cavities and an optical delay line for the heralding measurement. Currently, these elements are unavailable on-chip rendering integrated photonics implementations incompatible with the reflection scheme. We, therefore, consider another scattering-based protocol that exploits the same fundamental spin-photon interaction as the reflection scheme but circumvents the use of circulators and delay lines, allowing for an on-chip implementation. We refer to this scheme as the “carving” scheme since it is closely related to carving schemes for Bell state generation [66].

The carving scheme exploits the spin-dependent reflection/transmission from a qubit-coupled two-sided cavity or waveguide. Ideally, qubit state  $|0\rangle$  is uncoupled while state  $|1\rangle$  is strongly coupled to the incoming photon through the cavity/waveguide field as in the reflection scheme. Consequently, an incoming photon will be reflected if the qubit is in state  $|1\rangle$  and transmitted if the qubit is in state  $|0\rangle$  because of interference between the incoming and scattered fields [67]. This can be used to project an initially un-entangled multi-qubit state to a GHZ state probabilistically using a setup as depicted in Fig. 5(a).

The communication qubits are initially all prepared in the state  $|+\rangle$ , and a single photon is sent through the setup. The first beam splitter creates a superposition of the photon propagating in the upper (subscript “u”) or lower (subscript “l”) arm. Notably, the photon can only be transmitted through an arm if all communication qubits in that arm are in state  $|0\rangle$ . The final beam splitter erases the information about which arm the photon propagated through. The subsequent detection of the photon projects all communication qubits in the lower or

upper arm in state  $|0\rangle$ . Consequently, the detection of the photon will project the communication qubits into a state  $\frac{1}{\sqrt{2}}(|000 \dots\rangle_u |+++ \dots\rangle_1 \pm |+++ \dots\rangle_u |000 \dots\rangle_1)$ , with the phase determined by which detector recorded the photon. Each qubit state is flipped by applying NOT gates, and a second photon is sent through the setup. The detection of this photon will project the communication qubits into a GHZ state up to single qubit rotations.

Note that the carving scheme is inherently probabilistic, with a probability of success that decreases exponentially with the number of qubits. However, for low-weight GHZ states, this may not be too restrictive. The success probability for a 3-qubit GHZ state will be at most  $1/16$ , while a 4-qubit GHZ state will have a success probability of at most  $1/32$ . The actual success probability will be further lowered by photon loss and imperfect detection. We include this and additional hardware imperfections, such as finite coupling and unwanted transmission/reflection, in our modeling, considering the same four-level scheme as in the other protocols. We consider both a waveguide implementation and a cavity implementation. One crucial difference between the two is for the cavity. The input field can be detuned from the cavity resonance, while this is not possible with a waveguide, which we assume to have an effectively flat frequency response. Details of our analytical model of the hardware imperfections for the carving scheme are presented in App. F.

We also analyze the case of replacing the single-photon source with a weak coherent light source, as shown in App. G. However, we found that the fidelity of the resulting GHZ state is too low to realize modular quantum computing.

#### IV. SIMULATION PARAMETERS

In this section, we expand on the hardware parameters for the surface code architectures and the entanglement generation schemes utilized in their stabilizer measurements.

We consider a broad set of coherence and operation times parameters. This is shown in Fig. 6. Here,  $T_{\text{link}}^{\text{dec}}$  and  $T_{\text{idle}}^{\text{dec}}$  describe the coherence times applicable to the communication and memory qubits when entanglement generation is attempted and during idling, respectively, as described earlier. Next, we describe the operational times with  $t_{\text{link}}$  as the time for one entanglement generation attempt (either a Bell pair generation or direct GHZ state generation), and  $t_{\text{meas}}$  means the measurement time duration for the communication qubit. Further,  $t_P^{c/m}$  is the time duration of native single qubit gate  $P \in \{X, Y, Z, H\}$  acting on the communication (c)/memory (m) qubit. Then we have the two-qubit gate times for controlled -  $Z, X, iY$  rotations  $t_{CZ}, t_{CX}, t_{CiY}$  and SWAP operation  $t_{\text{SWAP}}$ . The two-qubit operations only apply between communication qubit (control) and

memory qubits (target).

Parameter Sets	Set - 1	Set - 2	Set - 3
$T_{\text{link}}^{\text{dec}}$	$10^4$	$10^5$	$10^6$
$T_{\text{idle}}^{\text{dec}}$	$10^5$	$10^5$	$10^6$
Operation times			
$t_{\text{link}}$	1	1	1
$t_{\text{meas}}$	1	1	1
$t_P^c$	0.01	0.01	0.01
$t_P^m$	100	100	100
$t_{CZ}, t_{CX}, t_{CiY}$	100	100	100
$t_{\text{SWAP}}$	300	300	300

FIG. 6. Table describing the coherence times and operation times. All values are expressed w.r.t.  $t_{\text{link}}$ , which is assumed to take one unit of time.

We express all the parameters w.r.t.  $t_{\text{link}}$  duration times. We consider three parameter sets with varying coherence times for link generation and idling. The first set has the lowest coherence times for which we find code thresholds. Set-2 has increased link coherence times by one order of magnitude, and finally, we consider Set-3, which has coherence times of  $10^6$ .

Although our simulation model allows for distinct  $T_1$  and  $T_2$  times, each for communication and memory qubits, we considered  $T_{1, \text{link}}^{\text{dec}} = T_{2, \text{link}}^{\text{dec}}$  and  $T_{1, \text{idle}}^{\text{dec}} = T_{2, \text{idle}}^{\text{dec}}$ , where 1,2 denote the  $T_1$  and  $T_2$  decay times. This model gives rise to an effective depolarizing noise on the qubits. We choose this noise model against the optimistic case of pure dephasing when  $T_{1, \text{link}}^{\text{dec}} = \infty$  and  $T_{1, \text{idle}}^{\text{dec}} = \infty$ . Moreover, our surface code architecture is not biased for  $X$  or  $Z$  type of errors; therefore, it is a natural choice for the noise model due to decoherence effects.

Next, we describe the parameter values for various entangling schemes that we consider. For each scheme, we have two sets of parameters: one inspired by experimental demonstrations, which seems within the reach of present quantum technology, the near-term parameters (NTP), and the future parameters (FP), where we boost some key parameters in the experiment. We describe these parameters for the emission-based (EM) scheme in Fig. 7. The relevant parameters of the physical setup for the reflection (RFL) scheme, carving (CAR) scheme with a single-photon source (SPS), and carving scheme with coherent light source (COH) are shown in Fig. 8, 9, and 10, respectively. We simulate the performance of the direct schemes based on the parameters of the diamond's silicon-vacancy (SiV) color center.

EM	NTP	FP
$F_{\text{prep}}$	0.99	0.999
$p_{\text{DE}}$	0.04	0.01
$\mu$	0.9	0.95
$\lambda$	0.984	1
$\eta$	0.0046	0.4472

FIG. 7. Parameter sets for the emission-based scheme. Here,  $F_{\text{prep}}$  [68, 69] describes the fidelity of emitter-photon state preparation,  $p_{\text{DE}}$  [70] is the probability of the double excitation error on the emitter caused during emitter-photon state preparation,  $\mu$  is the Hong-Ou-Mandel visibility of the photon interference [70][71],  $\lambda$  is the standard deviation in the path difference for the interference setup [70][72], and the effective photon detection probability is  $\eta_{\text{ph}}$  [73]. Furthermore, we have the probability of successful entanglement generation between two nodes  $p_{\text{succ}}^{\text{link}}$  which depends on  $\eta_{\text{ph}}$  and has the approximate value of  $p_{\text{succ}}^{\text{link}} \approx 10^{-4}$  and  $p_{\text{succ}}^{\text{link}} \approx 0.099$  for NTP and FP, respectively. The FP are inspired by potential improvements in the experiments.

RFL	Constrained parameters							Tuneable parameters	
	$\kappa_c/\gamma$	$P_{\text{dk}}$	$\frac{\kappa_c}{\kappa_c+\kappa_1}$	$\frac{\Delta}{\gamma}$	$\frac{\sigma}{\gamma}$	$C_1$	$\eta_c$	$\frac{\delta_1}{\gamma}$	$\frac{\omega}{\gamma}$
NTP	200	$10^{-6}$	0.90	16	0.46	30	0.5	16.3	283.0
FP	200	$10^{-6}$	0.95	122	0.32	40	0.9	32.2	130.7

FIG. 8. System parameters of the reflecting protocol (RFL). The constrained parameters are based on near-term parameters (NTP) and future parameters (FP), and the tuneable parameters are based on maximizing the final GHZ state fidelity. The near-term parameters are modelled from recent experimental demonstrations in Refs. [36, 37, 74]. The method for calculating the final GHZ state is shown in App. E. Symbol explanation:  $\kappa_c$  cavity loss rate from the cavity to the coupling fiber;  $P_{\text{dk}}$ : dark count rate of the photon detectors assuming the dark count happens at 1 Hz and the photon detection window is 1  $\mu\text{s}$ ;  $\gamma$ : natural linewidth of the spin;  $\kappa_1$ : cavity loss rate from the cavity to the environment;  $\Delta = \delta_0 - \delta_1$  with  $\delta_0 = E_{0e} - E_0 - \omega_{\text{ph}}$  and  $\delta_1 = E_{1e} - E_1 - \omega_{\text{ph}}$ ;  $\sigma$ : calibration error in  $\delta_1$  and  $\delta_0$ ;  $C_1$ : cooperativity between the spin and the one-side cavity, defined as  $C_1 = \frac{g_1^2}{\gamma(\kappa_c + \kappa_1)}$ , with  $g_1$  the coupling strength of the spin and the one-side cavity;  $\eta_c$ : circulator efficiency of preserving a photon;  $\omega = \omega_{\text{ph}} - \omega_c$ .

## V. RESULTS

We investigate the surface code architectures' code thresholds and sub-threshold behavior for each entangling scheme. We simulate a square toric surface code of even distance  $d$ , with  $d$  time layers. The code thresholds are calculated for the physical error probability  $p$ , parameterizing the circuit-level noise, i.e., each gate and measurement in the circuit has an error probability of failure  $p$ . The code thresholds were evaluated for different coherence time sets, each for NTP and FP scenarios. For each case, first, a threshold value  $p_{\text{th}}$  was found at some guessed value of the GHZ cut-off time  $t_{\text{cut}}$ , and

CAV CAR		Constrained parameters							Tuneable parameters					
		$\kappa_c/\gamma$	$P_{\text{dk}}$	$\frac{2\kappa_c}{2\kappa_c+\kappa_1}$	$\frac{\Delta}{\gamma}$	$\frac{\sigma}{\gamma}$	$C_2$	$\eta_f$	$\frac{\delta_1}{\gamma}$	$\frac{\omega}{\gamma}$	Weight-4		Weight-3	
		$n_{\text{sc}}$	$\alpha$	$n_{\text{sc}}$	$\alpha$									
NTP	SPS	200	$10^{-6}$	0.9	16	0.46	30	0.5	0	832.5	2	-	2	-
	COH										2	0.54	2	0.41
FP	SPS	200	$10^{-6}$	0.95	122	0.32	40	0.9	0	138.0	2	-	2	-
	COH										2	0.54	2	0.24

FIG. 9. System parameters of the cavity carving protocol (CAV CAR). The constrained parameters are based on near-term parameters (NTP) and future parameters (FP), and the tuneable parameters are based on maximizing the final GHZ state fidelity. The near-term parameters are modelled from recent experimental demonstrations in Refs. [36, 37, 74]. The method for calculating the final GHZ state with the single-photon source (SPS) is shown in App. F, and the one with coherent light (COH) is shown in App. G. Symbol explanation:  $C_2$ : cooperativity between the spin and the two-side cavity defined as  $C_2 = \frac{g_2^2}{\gamma(2\kappa_c + \kappa_1)}$ , with  $g_2$  the coupling strength of the spin and the two-side cavity;  $\eta_f$ : fiber efficiency of preserving a photon;  $n_{\text{sc}}$ : number of total scattering times;  $\alpha$ : parameters of the coherent state  $|\alpha\rangle$ . Other symbols are explained in the caption of Fig. 8.

WG CAR		Constrained parameters					Tuneable parameters				
		$P_{\text{dk}}$	$\frac{\Delta}{\gamma}$	$\frac{\sigma}{\gamma}$	$P$	$\eta_f$	$\frac{\delta_1}{\gamma}$	Weight-4		Weight-3	
		$n_{\text{sc}}$	$\alpha$	$n_{\text{sc}}$	$\alpha$						
NTP	SPS	$10^{-6}$	16	0.46	5	0.5	0	4	-	4	-
	COH							2	0.29	2	0.28
FP	SPS	$10^{-6}$	122	0.32	20	0.9	0	4	-	4	-
	COH							2	0.26	2	0.22

FIG. 10. System parameters of the waveguide carving protocol (WG CAR). The constrained parameters are based on near-term parameters (NTP) and future parameters (FP), and the tuneable parameters are based on maximizing the final GHZ state fidelity. The near-term parameters are modelled from recent experimental demonstrations in Refs. [36, 37, 74]. The method for calculating the final GHZ state with the single-photon source (SPS) is shown in App. F and the one with coherent light (COH) is shown in App. G. Symbol explanation:  $P = \Gamma/\gamma$  with  $\Gamma$  being the intensity of the light emitted from the spin and going into the waveguide. Other symbols are explained in the caption of Fig. 9.

once the threshold was found,  $t_{\text{cut}}$  was swept to find the optimal threshold for the physical error. This optimization was done via a binary search over  $p_{\text{th}}$  with respect to  $t_{\text{cut}}$ . We report the optimized code threshold for each case using the Union-Find decoder [75].

Based on the numerical investigation with different parameter sets, we, in general, required  $P_{\text{succ}}^{\text{link}} > 10^{-4}$  and a GHZ fidelity of at least 99%, for a threshold  $p_{\text{th}}$  to exist (see App. I). Coherence and operational times of Set-1 also serve as the lower bound for the existence of a threshold. Together, these bounds give a rough guide for the necessary hardware performance.

We report that we do not find any code thresholds using a coherent photon source (COH) as an approximate single-photon source for the carving scheme. To adequately suppress the probability of two-photon errors,

Weight - 4	Scheme	Parameters	$P_{\text{succ}}^{\text{link}}$	$p_{\text{th}}(\text{Set - 1})$	$p_{\text{th}}(\text{Set - 2})$	$p_{\text{th}}(\text{Set - 3})$
	Emission based	Near term	0.0001	NT	NT	NT
	Emission based	Future	0.0999	NT	NT	0.1323 % ( $k = 11$ ) ✓
	Direct Scheme	Parameters	$P_{\text{succ}}^{\text{GHZ}}$	$p_{\text{th}}(\text{Set - 1})$	$p_{\text{th}}(\text{Set - 2})$	$p_{\text{th}}(\text{Set - 3})$
	Reflection	Near term	0.0147	0.1707	0.2807 % ✓	0.3285 %
	Cavity Carving (SPS)	Near term	0.0013	NT	NT	0.3298 % ✓
	Waveguide Carving (SPS)	Near term	0.0003	NT	NT	0.0180 % ✓
	Reflection	Future	0.3782	0.3443 % ✓	0.3488 % ✓	0.3513 %
	Cavity Carving (SPS)	Future	0.0164	0.2387 % ✓	0.3450 % ✓	0.4072 % ✓
	Waveguide Carving (SPS)	Future	0.0047	NT	0.2158 % ✓	0.3541 % ✓

NT = No Threshold

FIG. 11. Weight-4 surface code thresholds. For every scheme and hardware parameter set, we report the code threshold for each coherence time set. We also report the optimal GHZ generation fusion-based protocol for the emission-based scheme via the number of Bell pairs ( $k$ ) used in that protocol. The reported code thresholds ( $p_{\text{th}}$ ) followed by a check mark are the ones that are higher than the corresponding WT3 surface code threshold. NT denotes that “no threshold” exists.

Weight - 3	Scheme	Parameters	$P_{\text{succ}}^{\text{link}}$	$p_{\text{th}}(\text{Set - 1})$	$p_{\text{th}}(\text{Set - 2})$	$p_{\text{th}}(\text{Set - 3})$
	Emission based	Near term	0.0001	NT	NT	NT
	Emission based	Future	0.0999	NT	NT	0.0928 % ( $k = 7$ )
	Direct Scheme	Parameters	$P_{\text{succ}}^{\text{GHZ}}$	$p_{\text{th}}(\text{Set - 1})$	$p_{\text{th}}(\text{Set - 2})$	$p_{\text{th}}(\text{Set - 3})$
	Reflection	Near term	0.0423	0.1717 % ✓	0.2353 %	0.3350 % ✓
	Cavity Carving (SPS)	Near term	0.0041	NT	0.0167 % ✓	0.3062 %
	Waveguide Carving (SPS)	Near term	0.0009	NT	NT	NT
	Reflection	Future	0.4823	0.2784 %	0.2849 %	0.3521 % ✓
	Cavity Carving (SPS)	Future	0.0366	0.1787 %	0.2603 %	0.3678 %
	Waveguide Carving (SPS)	Future	0.0098	NT	0.1522 %	0.3441 %

NT = No Threshold

FIG. 12. Weight-3 surface code thresholds. Refer to the caption of Fig. 11 for the explanation.

the probability of successful GHZ state generation was estimated to be as low as  $10^{-4}$ . The best GHZ state fidelity we obtained, assuming no gate error in the scheme execution, was only 96.9% and 97.8% for the CAV CAR scheme, WT4 and WT3, respectively. Since we expected similar performance for the reflection scheme, we did not pursue a simulation of the reflection scheme with a coherent photon source. In the next subsections, we only describe the threshold results for a perfect single photon source. Note, however, that the performance for a non-deterministic single-photon source can be estimated from this by absorbing the inefficiency of the photon source into the overall detection efficiency.

#### A. Weight-4 surface code thresholds

We present the WT4 architecture threshold results in Fig. 11. We found no threshold for the EM schemes for the NTP for any coherence times parameter set. The success probability ( $P_{\text{succ}}^{\text{link}}$ ) of Bell pair generation for NTP is only  $10^{-4}$ , which leads to very long waiting times during Bell pair generation that makes the decoherence noise dominant on the data qubits. And the Bell pair fidelity

is less than 90%. Even for the future parameters (with  $P_{\text{succ}}^{\text{link}} = 0.0999$ ), we get a code threshold for only the best coherence times for Set-3. This threshold was found for the protocol with  $k = 11$  Bell pairs. Refer to App. D 4 for details on EM fusion and distillation protocols.

For the direct schemes with NTP parameters, we find relatively high thresholds. For the RFL scheme ( $P_{\text{succ}}^{\text{GHZ}} = 0.0147$ ). Thresholds rapidly increase with the increasing coherence times. We only get a threshold value for the highest coherence times for the CAV CAR scheme with an ideal single photon source (SPS). We find no thresholds for Set-1 and Set-2. This fact is associated with the low probability of success for the CAV CAR scheme ( $P_{\text{succ}}^{\text{GHZ}} = 0.0013$ ), which is around an order of magnitude below the RFL scheme. In this regime, the decoherence noise becomes dominant. For the WG CAR scheme (SPS), the success probability is even lower ( $P_{\text{succ}}^{\text{GHZ}} = 0.0003$ ), and we see an even lower threshold for Set-3.

In contrast, we see higher thresholds for FP. The RFL scheme has the highest  $P_{\text{succ}}^{\text{GHZ}} = 0.3782$ , boosting the thresholds. The thresholds for the RFL scheme saturate around  $\sim 0.35\%$ , meaning further improvements on the coherence parameters do not increase the threshold due

to other noise sources present. Similarly, for the CAV CAR ( $P_{\text{succ}}^{\text{GHZ}} = 0.0164$ ), we see a boost in the thresholds, with the highest value of 0.4072% for Set-3. This happens because the CAV CAR scheme has higher GHZ state fidelity than the RFL scheme (see Fig. 13(d)), and with Set-3, the coherence times are high enough for both the schemes that the GHZ fidelity draws the difference in the performance. Finally, we get an even lower success probability for the WG CAR scheme ( $P_{\text{succ}}^{\text{GHZ}} = 0.0047$ ), with no thresholds for coherence times of Set-1. However, rapidly increasing thresholds for Set-2 and Set-3 indicate that the threshold is very sensitive to the coherence times in this regime.

### B. Weight-3 surface code thresholds

The WT3 threshold results are summarized in Fig. 12. The general trend is similar to the WT4 thresholds. We find no thresholds for NTP for emission-based schemes. Then, we find a threshold of 0.0928% only for the coherence times of Set-3 with FP (with  $P_{\text{succ}}^{\text{link}} = 0.0999$ ), which is lower than the corresponding WT4 threshold. This happens since emission-based schemes take longer as they are restricted by the slow two-qubit gate times on the auxiliary qubits involved in fusion, and this impacts the WT3 architecture more as it has twice as long QEC cycle times as WT4 QEC cycles. Therefore, it introduces more errors in the code.

The direct schemes' success probabilities for the WT3 GHZ states are higher than the WT4. We find very competitive thresholds for the RFL scheme ( $P_{\text{succ}}^{\text{GHZ}} = 0.0423$ ) with FTP. Here, we also get a threshold for the CAV CAR scheme ( $P_{\text{succ}}^{\text{GHZ}} = 0.0041$ ) for Set-2 coherence times, which is, however, small. But we found no threshold for the WG CAR ( $P_{\text{succ}}^{\text{GHZ}} = 0.0009$ ) with NTP. This relates to the low  $P_{\text{succ}}^{\text{GHZ}}$ , leading to long waiting times during GHZ state generation and increasing the impact of decoherence noise.

A significant boost is seen for FP. Amongst this block, Set-1 and Set-2 thresholds sit closely, while one can observe a significant rise in thresholds when the coherence times are increased by an order of magnitude from Set-2 to Set-3. The change is most sensitive for the RFL scheme (with highest  $P_{\text{succ}}^{\text{GHZ}} = 0.4823$ ) from Set-2 to Set-3. Meanwhile, for the CAV CAR scheme ( $P_{\text{succ}}^{\text{GHZ}} = 0.0366$ ) with a relatively much lower success probability, we see a uniform increase in the thresholds when increasing the coherence times. For the WG CAR scheme, even lower success probability ( $P_{\text{succ}}^{\text{GHZ}} = 0.0098$ ) leads to longer waiting times and no threshold for Set-1, but increased threshold with Set-2, and finally catches up close to the WT4 threshold for Set-3.

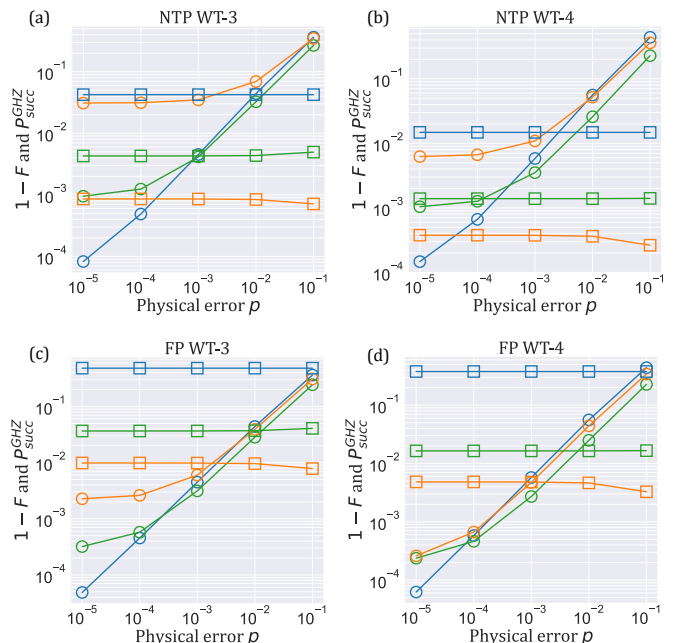


FIG. 13. Success rates  $P_{\text{succ}}^{\text{GHZ}}$  (squares) and GHZ state infidelity  $1 - F$  (circles) of RFL scheme (blue), CAV CAR (green) with SPS and WG CAR (orange) with SPS, as a function of physical error probability. The subtitles of the plots denote the parameter used (NTP/FP) and the surface code architecture (WT-3/4). Due to different state mixing in the protocol run via the depolarizing channel, there is a weak dependence of  $P_{\text{succ}}^{\text{GHZ}}$  on the physical error. This is numerically evident in the plots.

### C. Weight-4 vs. Weight-3 architecture

When comparing the WT3 and WT4 architectures, we see that they can have competitive code thresholds depending on the physical parameters. First, we must note that the WT3 architecture has half the number of modules compared to the WT4 architecture. However, the WT3 architecture has twice the data qubits per module. For the modules, we considered that the module can host multiple memory qubits that can be used as code data qubits. Therefore, when the number of modules is a bottleneck for the experiment, WT3 architecture can be chosen. Another way of looking at the construction would be to choose WT3 architecture when we want the largest code distance for the same number of available network modules.

Secondly, the QEC cycle times of the WT3 architecture are twice as long for the same distance of the code. WT4 would be preferred over WT3 architecture if many modules are available, without compromising the logical clock speed. If the physical measurement error rates are lower, one could afford to do fewer time layers for the code, bringing the runtime of the WT3 closer to that of the WT4 architecture.

The WT3 architecture has an adverse effect due to error propagation within each node, as it has two data

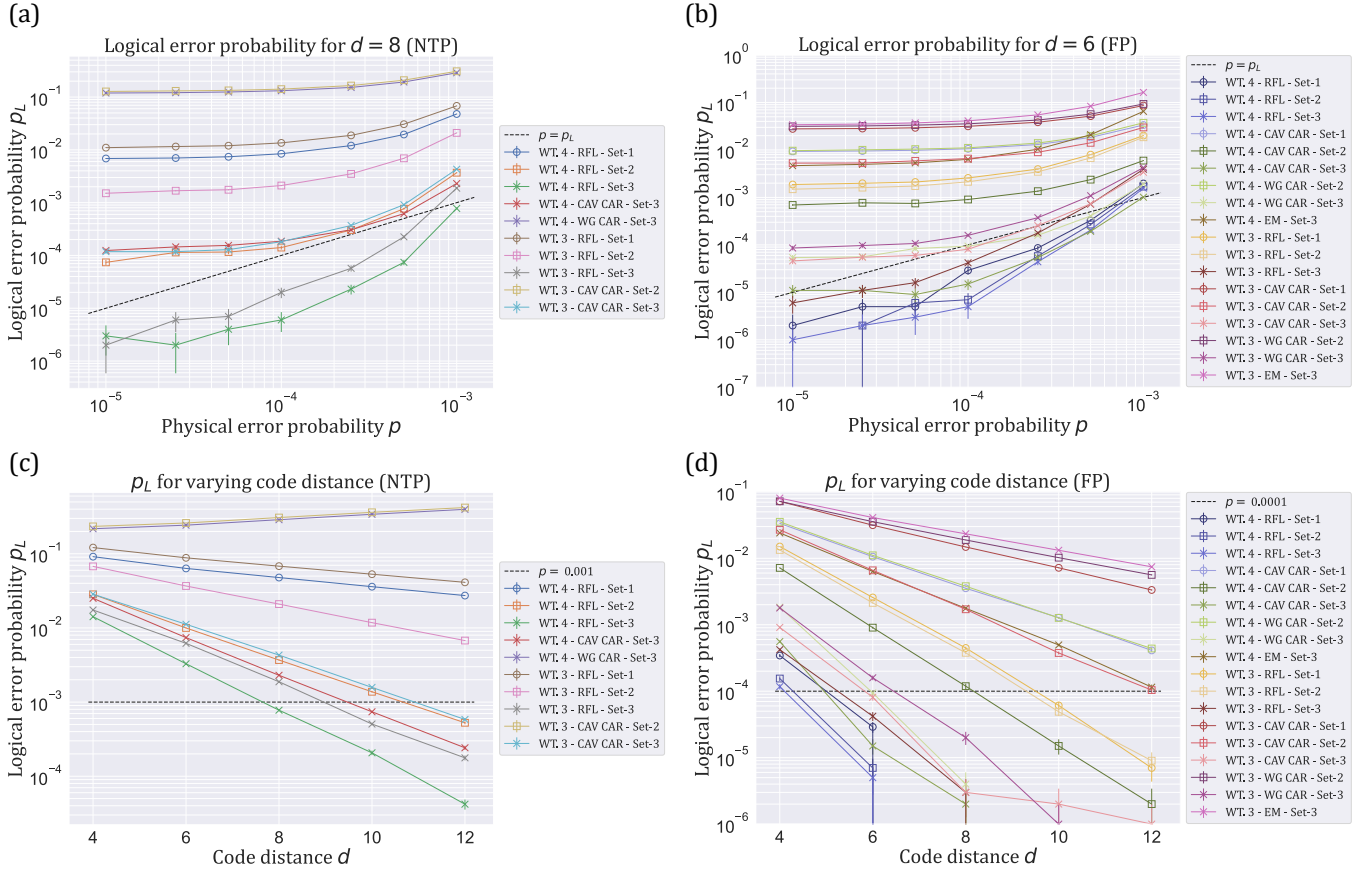


FIG. 14. Sub-threshold behavior of architectures that have an error threshold. For clarity, Set-1, Set-2, and Set-3 are shown with circle, square, and cross markers. All curves are checked for monotonicity, including the error bars. (a) Logical error probability ( $p_L$ ) for NTP for the smallest even-sized code distance  $d = 8$  shows better than break-even performance. (b)  $p_L$  with FP, for the smallest even-sized code distance  $d = 6$ , which shows better than break-even performance. (c)  $p_L$  for NTP, against varying code distance, with constant  $p = 10^{-3}$ . For WT.4 WG CAR Set-3 and WT.3 CAV CAR Set-2, we see an increase in  $p_L$  for an increase in  $p$  because the threshold for these architectures is less than  $10^{-3}$ , which is 0.0180% and 0.0167%, respectively. (d)  $p_L$  with FP, against varying code distance, with constant  $p = 10^{-4}$ . Some curves are discontinued after a certain code distance because no logical failure was recorded beyond this point, even with  $10^6$  iterations per data point. More iterations are required for accuracy, but it was beyond our computational resources' ability to estimate.

qubits per module. The locally controlled operations can propagate errors within each node. These error propagations can be tracked using flag qubits [76, 77] for improved performance, but only the bare stabilizer measurements are considered for this work. This is discussed in more detail in App. C3. Also, due to a sub-round structure of stabilizer measurements, errors can occur on the data qubits between two rounds, affecting the decoding. This leaves a heavier impact on the WT3 architecture as it has twice the sub-rounds. See App. C4 for details on these errors. We also report that the WT4 architecture generally has about 5% lower logical error rates, estimated numerically. For the reasons above, we associate this observation with the less-good decoding of WT3 surface code.

#### D. Comparison between entangling schemes

The threshold data shows that the direct schemes outperform the emission-based (fusion) schemes in code threshold performance. Two factors are responsible for this. One is that the emission-based schemes require noisy two-qubit gates involving the memory qubits for Bell pair fusion operations, while the direct schemes do not engage noisy two-qubit memory gates. The other factor is high  $P_{\text{succ}}^{\text{GHZ}}$  for direct schemes, which reduces the  $t_{\text{cut}}$  for the same ratio of GHZ generation rate. Thereby reducing the effect of decoherence noise on the memory qubits.

We did a separate investigation to verify the noise impact via the fusion process in the EM scheme. We considered a fictitious set of parameters for WT4 EM Set-3 (FP). We boosted  $P_{\text{succ}}^{\text{link}} = 0.3782$  and Bell-pair fidelity

$F_{\text{link}} = 99.75\%$  so that it matches the effective GHZ state fidelity and success probability to the WT4 RFL Set-3 (FP) (with  $p_{\text{th}} = 0.3513\%$ ). The new threshold only increased from 0.1323% to  $\approx 0.1600\%$ , and saturated around this value for any further parameter improvements. This lack of improvement in the EM threshold can be explained via the noisy fusion process, which suppresses the performance of the EM scheme. Further insight into comparing different direct schemes is achieved through Fig. 13. The success rates and state fidelity of the reflection scheme and the carving scheme with the single photon source are shown for the relevant physical error rates.

### E. Sub-threshold performance of the architectures

Most reported thresholds are near  $p = 10^{-3}$ . We simulated the logical error probability ( $p_L$ ) for physical error probability as low as  $p = 10^{-5}$  to see the sub-threshold performance of the schemes and architectures. We consider the smallest non-trivial even-sized code distance  $d = 4$ , up to  $d = 12$ , to study the logical error rates for all the architectures and schemes. We analyze the smallest code distance for each NTP and FP case, which gives break-even performance.

The logical error rates for code distance  $d = 8$  lattice size are shown in Fig. 14(a) for NTP. We see the logical error rates for all the coherence times sets (1,2,3) and schemes.  $d = 8$  is the smallest code distance for which we get  $p_L \ll p$  for at least one architecture. We show the logical error rates in the FP case in Fig. 14(b). We do this for distance  $d = 6$ , for which we get better than break-even performance for at least one architecture. For the smallest  $d = 4$ , WT4 RFL Set-3 shows just the break-even performance (with  $p_L \approx p$ ) near  $p = 10^{-4}$ . A preferred scheme and architecture combination can be chosen for the minimal logical error rates. The plot shows that the logical error rates saturate and do not decrease when going near  $10^{-5}$ . This is because the system has residual noise beyond the circuit-level noise, which comes from the hardware, mainly due to the noisy GHZ state preparation. We still have all the noise due to the noisy hardware implementation and decoherence on the data qubits, which are not varied in these plots.

Furthermore, we increase the code distance to see how the logical error rates improve for relevant and fixed physical error rates in the sub-threshold regime. We plot the logical error rates against the varying code distance in Fig. 14(c) for NTP parameters with  $p = 10^{-3}$  and Fig. 14(d) for NF parameters with  $p = 10^{-4}$ , respectively. As expected, the logical error rates fall exponentially upon increasing the distance below the code threshold. For the NTP parameters, we see break-even performance for WT4 RFL Set-3 with only  $d = 8$ , and a few other schemes catch up with lattice size  $d = 10$ . We see improved sub-threshold performance for the FP case with a break-even starting lattice size of just  $d = 6$ . Most of the FP schemes

demonstrate  $p_L \leq p$  for distance 12 onwards.

## VI. CONCLUSION AND DISCUSSION

Our work has outlined several feasible approaches for modular error-corrected quantum computations with solid-state quantum hardware. We demonstrated that architectures with a single or two data qubits per module have similar code thresholds, which, however, highly depend on the choice of GHZ state generation schemes. We found that, in general, the direct schemes result in higher thresholds due to the faster and higher quality GHZ state generation for the distributed stabilizer measurements. The reason for this is that they circumvent the noisy and slow two-qubit gates and measurements required for emission-based schemes. We have also provided bounds on the coherence times vs. operation times for the threshold performance of the modular architectures. Architectures with  $T_{\text{link}}^{\text{dec}}/t_{\text{link}} < 10^4$  will not be a reliable candidate for distributed modular architectures as defined in our framework. A GHZ state success probability  $P_{\text{succ}}^{\text{GHZ}} > 10^{-4}$  and GHZ fidelity  $F_{\text{GHZ}} > 99\%$  is strictly required for achieving a code threshold.

While we studied the surface code due to its established performance, it will be interesting to consider other codes that might better exploit the GHZ-state-enabled non-local stabilizer measurements. In particular, codes that could offer reduced qubit overhead, such as the recently introduced quantum low-density parity check (qLDPC) family known as the Bivariate Bicycle (BB) codes, by IBM [78]. Furthermore, extending the simulations to investigate the performance of logical gates and computation [79], even for the surface code, would be an interesting future direction.

## ACKNOWLEDGMENTS

The authors thank Tim Taminiau, Ronald Hanson, Erwin van Zwet, and Barbara Terhal for helpful discussions and feedback. We gratefully acknowledge support from the joint research program ‘‘Modular quantum computers’’ by Fujitsu Limited and Delft University of Technology, co-funded by the Netherlands Enterprise Agency under project number PPS2007. D.E. was partially supported by the JST Moonshot R&D program under Grant JPMJMS226C. J.B. acknowledges support from The AWS Quantum Discovery Fund at the Harvard Quantum Initiative. We thank SURF ([www.surf.nl](http://www.surf.nl)) for the support in using the National Supercomputer Snelius.

## SOURCE CODE AND DATA AVAILABILITY

The source code and simulation for this research’s findings are openly available in 4TU.ResearchData [80].

## Appendix A: Noise model for stabilizer measurements

In this appendix, we describe the noise modeling for the stabilizer circuits. As discussed before, the stabilizer circuit can be decomposed in two steps. The first step is the GHZ state generation using an entanglement generation scheme, and the second step is the application of locally controlled gates and measurement of the communication qubits. The detailed noise modeling of the entanglement generation is described in the respective appendices. We apply circuit-level noise and decoherence noise to all the qubits involved in the stabilizer circuit at all times. We describe these noise channels in detail here.

### 1. Circuit-level noise

We consider the gate set  $\{X^{c/m}, Y^{c/m}, Z^{c/m}, H^{c/m}, CZ, CiY, CNOT, SWAP\}$  as the native gate set for the module, where  $c/m$  denotes whether the single qubit gate is applied to the communication qubit or memory qubit. Circuit-level noise [81] implies that we apply noise during state preparation, single-qubit gates, two-qubit gates, and measurement operations. We model this as a depolarizing channel characterized by error probability  $p_g$ , which we call gate error. The measurement error, denoted as  $p_m$ , is modeled as the probability of a flipped measurement outcome. State preparation, idling, and single-qubit gate noise are modeled as the ideal operation followed by a single qubit depolarizing channel as [1]:

$$\mathcal{N}_{\text{gate}}^{\text{single-qubit}}(\rho) = (1 - p_g)\rho + \frac{p_g}{3} \sum_{P_j} P_j \rho P_j \quad (\text{A1})$$

where  $P_j \in \{X, Y, Z\}$  are the Pauli matrices for single qubit. While the two-qubit gate noise (here  $\rho$  is now a two-qubit density matrix) is modeled via the two-qubit depolarizing channel:

$$\mathcal{N}_{\text{gate}}^{\text{two-qubit}}(\rho) = (1 - p_g)\rho + \frac{p_g}{15} \sum_{(P_j, P_k) \notin (\mathbb{I}, \mathbb{I})} (P_j \otimes P_k) \rho (P_j \otimes P_k)^\dagger \quad (\text{A2})$$

This channel is applied after the noiseless application of any two-qubit gates involving a communication and memory qubit. We choose  $p_g = p_m = p$  as the physical error rate for the simulations and sweep  $p$  in our simulations to parameterize all the circuit-level noise.

### 2. Decoherence noise

Decoherence on the qubits is modeled as a continuous function of time with relevant coherence times as stated in Fig. 6, with all operations and gates tagged with their time duration. We implement the decoherence channel

in terms of its Kraus operator sum representation as [1]:

$$\mathcal{N}^{\text{dec}}(\rho) = \sum_{j=1}^{\kappa} K_j \rho K_j^\dagger \quad (\text{A3})$$

where  $\rho$  is any general single qubit density matrix and  $K_j$  are the Kraus operator elements, which satisfy  $\sum_{j=1}^{\kappa} K_j K_j^\dagger = \mathbb{I}$ .

The  $T_1$  time decay is described by the generalized amplitude damping (GAD) noise channel with Kraus operators:

$$\begin{aligned} K_1^{\text{GAD}} &= \frac{1}{\sqrt{2}} \begin{bmatrix} 1 & 0 \\ 0 & \sqrt{1 - \gamma_1} \end{bmatrix} \\ K_2^{\text{GAD}} &= \frac{1}{\sqrt{2}} \begin{bmatrix} 0 & \sqrt{\gamma_1} \\ 0 & 0 \end{bmatrix} \\ K_3^{\text{GAD}} &= \frac{1}{\sqrt{2}} \begin{bmatrix} \sqrt{1 - \gamma_1} & 0 \\ 0 & 1 \end{bmatrix} \\ K_4^{\text{GAD}} &= \frac{1}{\sqrt{2}} \begin{bmatrix} 0 & 0 \\ \sqrt{\gamma_1} & 0 \end{bmatrix} \end{aligned} \quad (\text{A4})$$

where  $\gamma_1 = 1 - e^{-t/T_1}$  is the decay factor with  $t$  the time duration of the operation and  $T_1$  the coherence time applicable.

$T_2$  time decay is the pure dephasing noise channel modeled via phase damping (PD) with coherence times  $T_2$ . This has the Kraus operators:

$$K_1^{\text{PD}} = \begin{bmatrix} 1 & 0 \\ 0 & \sqrt{1 - \gamma_2} \end{bmatrix}, \quad K_2^{\text{PD}} = \begin{bmatrix} 0 & 0 \\ 0 & \sqrt{\gamma_2} \end{bmatrix}. \quad (\text{A5})$$

Again with  $\gamma_2 = 1 - e^{-t/T_2}$ . These decoherence noise channels are applied for given operations or gate times, including link generation times, idling, and measurement times. When both these channels are applied together, they give rise to an effective depolarizing channel.

## Appendix B: Superoperator approach to QEC simulation

This appendix describes the core of our QEC simulations using the superoperator approach for the noisy stabilizer measurement circuits. This approach is adopted from the former work on fully distributed architectures from the references [19, 82]. We adopted this method to simulate our WT4 and WT3 architectures' noisy stabilizer measurements. To simulate noise beyond the circuit-level noise model, we need to simulate the full-density matrix of the noisy stabilizer circuit. For an  $n$  qubit system, we would need  $2^{2n}$  density matrix elements to be stored and would need very large matrix multiplications for applying any unitary operator. The problem becomes rapidly intractable as the number of qubits grows. This is where the superoperator representation is efficient. The idea is to estimate the noisy superoperator that describes the noisy stabilizer measurements

on a unit cell of the surface code architecture and then use that noisy superoperator to simulate the other many unit cells of the code, depending upon its distance in each logical operator. Here, the underlying assumption is that errors are not correlated between distant modules of the distributed code. This is true because all modules are independent and only interact during the entanglement generation protocols via their communication qubits.

As we will describe, the noise applied to the code via the superoperator application is done by sampling Pauli errors to align with the stabilizer simulations. This is computationally easy to decode, in contrast to full-density matrix simulations of all the code data qubits. This is equivalent to Pauli twirling the more general noisy channel. Since the stabilizer measurement operators then incorporate only Pauli errors, they give deterministic measurement outcomes that can be fed to the decoder of choice. Now, we describe the analytical treatment of the superoperator approach.

### 1. Superoperator analytical model

Represent the Hilbert space of all the qubits involved in the stabilizer measurement circuit as  $\mathcal{H}$ . This involves all the data qubits of the stabilizer and the communication qubits. We can see this total Hilbert space as the direct product of the subspace of data qubits, which undergo the unitary transformation during the stabilizer measurement, and the communication qubits, which are measured out at the end of this transformation, as  $\mathcal{H} = \mathcal{H}_D \otimes \mathcal{H}_c$ . Our stabilizer circuit involves a GHZ creation over the desired communication qubits of the nodes, followed by the application of controlled gates and measurements. The density matrix of the GHZ state created via a chosen scheme is the input to this circuit. The action of the noisy stabilizer circuit  $\mathcal{S}$  is to perform the transformation:

$$\mathcal{S}(\rho_D \otimes \rho_c) = \rho'_D \quad (\text{B1})$$

where  $\rho_D$  is the state of the data qubits,  $\rho_c$  state of the communication qubits. And  $\rho'_D$  is the reduced density matrix of the data qubits after the communication qubits are measured out. Suppose we figure out a Pauli decomposition of the effective transformation using Kraus operators on the post-measurement state and their corresponding probabilities. In that case, we can use these to sample errors on the code lattice for the decoding. Choi-Jamiolkowski isomorphism [83] can be exploited to find this desired decomposition of the stabilizer circuit action. Consider each of the incoming data qubits to be one qubit of the Bell pair  $|\Phi_+\rangle = \frac{1}{\sqrt{2}}(|00\rangle + |11\rangle)$ . The map  $\mathcal{S}$  acts only the data qubits, while their entangled counterparts remain unchanged. Then, the initial joint state to the stabilizer circuit can be expressed as:

$$|\rho\rangle = \frac{1}{\sqrt{2^{n_D}}} \sum_{i=0}^{2^{n_D}-1} |i\rangle|i\rangle \quad (\text{B2})$$

Where  $n_D$  is the total number of data qubits in a stabilizer unit cell. The noisy stabilizer circuit acts as:

$$\rho_S = (\mathcal{S} \otimes \mathbb{I})|\rho\rangle\langle\rho| = \sum_j p_j (K_j \otimes \mathbb{I})|\rho\rangle\langle\rho|(K_j \otimes \mathbb{I})^\dagger \quad (\text{B3})$$

where each Kraus operator  $K_j$  can be expressed in the computational basis as  $K_j = \sum_{x,y} [K_j]_{xy} |x\rangle\langle y|$ . Then, the action of each Kraus operator element yields an interesting fact:

$$\begin{aligned} [K_j]|\rho\rangle &= \frac{1}{\sqrt{2^{n_D}}} \sum_{x,y} [K_j]_{xy} |x\rangle\langle y| \sum_i |i\rangle|i\rangle \\ &= \frac{1}{\sqrt{2^{n_D}}} \sum_{x,y} \sum_i [K_j]_{xy} \delta_{yi} |x\rangle|i\rangle \\ &= \frac{1}{\sqrt{2^{n_D}}} \sum_{x,y} [K_j]_{xy} |x\rangle|y\rangle \end{aligned} \quad (\text{B4})$$

This equation reveals the relationship between the Kraus operators  $[K_j]$  and their action on a computational basis. The output state density matrix can be diagonalized to reveal the Kraus operators.

### 2. Using the superoperator decomposition

The idea in App. B1 can be readily applied to the noisy parity projections for the stabilizer measurements. If  $\rho_D$  is the state of incoming data qubits to the stabilizer measurement circuit, and  $\Pi_M$  is the associated projector of the measurement, then the output state is  $\rho'_D = \Pi_M(\rho_D)/\text{Tr}[\Pi_M(\rho_D)]$ . However, because the stabilizer measurement is noisy, we also get erroneous outcomes, which leads to the effective projector:

$$\begin{aligned} \Pi_M^{\text{eff}}(\rho_D) &= \sum_e (a_e^M E_e \Pi_M^{\text{ideal}}(\rho_D) E_e^\dagger \\ &\quad + b_e^{\bar{M}} E_e \Pi_M^{\text{ideal}}(\rho_D) E_e^\dagger) \end{aligned} \quad (\text{B5})$$

where  $\bar{M}$  denotes a faulty measurement, and  $e$  runs over all the possible Pauli errors on the data qubits. The errors on the data qubits  $E_e = P_1 P_2 \dots P_w$  with  $P_j \in \{I, X, Y, Z\}$  are the Pauli errors on the data qubits involved in the stabilizer measurement ( $w = 4$  for WT4 and  $w = 8$  for WT3 architecture, respectively; note that it is not the weight of the stabilizer but the number of data qubits involved in one unit cell of the architecture's lattice). Here, we assumed the Pauli basis decomposition for the Kraus operators in the spirit of the previous argument. However, instead of diagonalizing the resulting density matrix, we can instead find the coefficients  $a_e$  and  $b_e$  for known error permutation  $e$  on the data qubits. Assuming the form  $[K_j] = (P_1 P_2 \dots P_w) \Pi_{M/\bar{M}}^{\text{ideal}}$  and get the output state:

$$\rho_j = (K_j \otimes \mathbb{I})|\rho\rangle\langle\rho|(K_j \otimes \mathbb{I})^\dagger \quad (\text{B6})$$

Using this pre-computed output state, we can directly calculate the overlap with the noisy output state of the stabilizer circuit to get the error probabilities as:

$$p_j = F(\rho_S, \rho_j) = \text{Tr} \left[ \sqrt{\sqrt{\rho_j} \rho_S \sqrt{\rho_j}} \right] \quad (\text{B7})$$

This method fully decomposes data qubit, measurement errors, and their corresponding error probabilities. We use the software stack developed by us for these superoperator calculations, called CIRCUITSIMULATOR. We can randomly sample from this error probability distribution to apply errors on the code lattice and decode those errors using a decoder of choice [19, 25]. This part of the simulation is handled by our QEC simulator for surface codes, called QSURFACE, which can handle monolithic or distributed surface code simulations for an input superoperator. We describe this part of the simulations in the next subsection.

### Appendix C: Distributed surface code simulations

This appendix describes the QEC simulations for the WT4 and WT3 architecture. The input to these simulations is the superoperator in a tabular format using methods in the App. B to decompose the superoperator. Error probability for each Pauli string Kraus operator is calculated and arranged in a tabular form, along with measurement errors, either when there is GHZ success within the cutoff time  $t_{\text{cut}}$  or a GHZ state generation failure. For all these possible scenarios, it has a total number of rows equal to  $4^4 \times 2 \times 2 = 1024$ . Once we sample GHZ success, data qubit and measurement errors from this error-probability distribution based on the weights, the effective joint measurement outcome is deterministic, either  $\pm 1$ , for each sampled error. These stabilizer outcomes are fed to the decoder thereafter. Now, we describe how these Monte Carlo simulations are executed for each of our architectures, with examples.

#### 1. QEC simulations for WT4 architecture

The compact tabular format of the WT4 superoperator is shown in Fig. 15. The "Error" column describes the data qubit errors on the stabilizer data qubits, the "GHZ Success" column tells whether the GHZ generation was successful or not, and the "Meas. Error" column states whether there is a measurement error on the communication qubits during the stabilizer measurement, and the "Plaquette (Z)" and "Vertex (X)" columns describe the probability of these error combinations for each stabilizer type. This is a compact form of the tabular superoperator constructed in Ref. [25]. For a QEC cycle, we start with  $R_1^Z$  stabilizers. For each stabilizer, we sample for error probabilities from the "Plaquette (Z)" column and output one row. Say we sampled {IIII, TRUE, TRUE} (shown in light-red). This means there is no data qubit

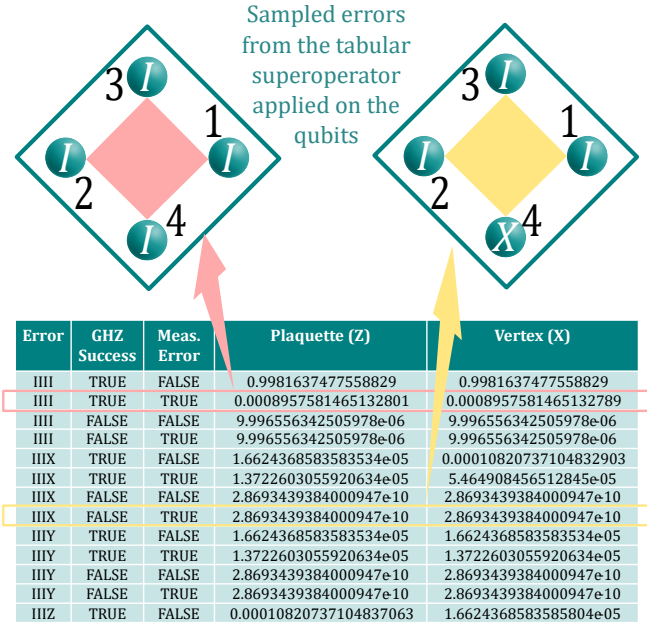


FIG. 15. Application of data qubit errors on the code WT4 lattice, using the tabular superoperator calculated from Sec. B 2. For each plaquette and vertex stabilizer, we sample errors from the superoperator based on the given error probability and apply the respected errors in the right order.

error on the stabilizer data qubits; the GHZ state was successfully generated, but there is a measurement error on the communication qubits. Therefore, we apply no data qubit error on the data qubits. We will flip the outcome when we measure the stabilizer due to the measurement error. Then, we move on to the next stabilizer and sample from the superoperator until the sub-round is completed.

Another instance can be understood from the X stabilizer measurements (shown in yellow); after sampling, we randomly output {IIIX, FALSE, TRUE}. This means the fourth data qubit has an X error. However, there was also a GHZ failure, so we cannot perform the stabilizer measurement. Therefore, we will copy the previous stabilizer outcome value to this current stabilizer, but we apply the X error on the data qubit caused due to noise during the stabilizer attempt. The measurement error does not matter when GHZ state generation fails, as we see that both TRUE/FALSE scenarios for measurement error have the same weight. This way, we apply all the different error combinations to the stabilizer data qubits. After all the sub-rounds in a layer are done, we measure that layer, including the measurement errors sampled for each stabilizer. For the final layer, we do perfect measurements to have an even number of syndromes (this is a simplification for the simulation purpose). Once all the layers are completed for the QEC cycle, we send the 3D syndrome graph data composed of the stabilizer outcomes to the decoder, either Minimum Weight Perfect Matching (MPWM) or Union-Find (UF) decoder.

## 2. QEC simulations for WT3 architecture

The WT3 superoperator is a little more complicated. It helps to first look at the WT3 unit cell structure and identify different data qubits involved, as shown in Fig. 16.

Let us look at one unit cell of the WT3 toric surface code, consisting of modules A, B, C, & D with the corresponding labeled data qubits. We consider the same noise model as the WT4 surface code. However, additional idling is involved on data qubits for WT3 surface code. Consider the current stabilizer measurement on the light-yellow, round-1 Z-type stabilizer. Modules A, B, and C are active in the stabilizer measurement. But module D is entirely idle during this sub-round. Here, we first point out the noise action on various qubits involved.

During the generation of the GHZ state by a chosen entanglement generation scheme, modules A, B, and C attempt entanglement generation; during this attempt, all the memory qubits (consisting of data qubits 1,2,3,4,5,6) are subjected to the decoherence with coherence times  $T_{\text{link}}^{\text{dec}}$  (labeled with \*\*). The attempt could be a Bell pair generation (EM scheme) or direct GHZ state (RFL and CAR schemes). We refer to data qubits 5 and 6 as active-idle qubits because they are idle in the active modules. While module D does not attempt any entanglement generation during this stabilizer sub-round (entirely idle module), and the memory qubits 7 and 8 are subjected to the decoherence  $T_{\text{idle}}^{\text{dec}}$  (labeled with \*) at all times. We refer to these qubits as fully idle data qubits. While certain neighboring round-1 Z stabilizers attempt GHZ generation, the considered  $R_1^Z$  stabilizer might succeed in GHZ generation. In which case, the stabilizer will be immediately measured out, and there will be some idling on all the eight data qubits, again with the coherence times  $T_{\text{idle}}^{\text{dec}}$ .

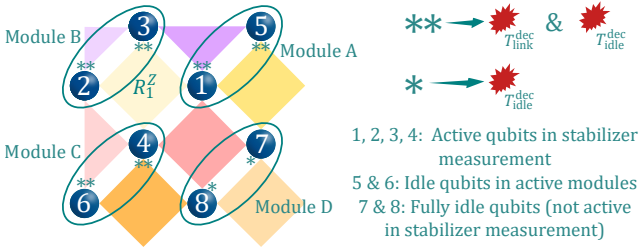
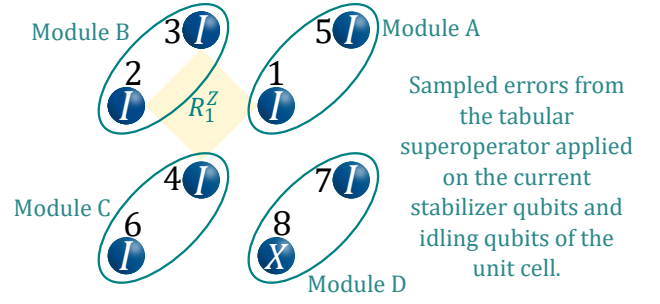


FIG. 16. Unit-cell for WT3 surface code layout, for a  $R_1^Z$  stabilizer. There are 8 data qubits involved in the current stabilizer measurement, out of which 4 are active stabilizer qubits and 4 are idling qubits. These qubits undergo different decoherence rates depending on GHZ success and failure of the current stabilizer.

The WT3 superoperator's tabular form has an additional column, "Idle", that indicates the noise on the four idling qubits. Instead of creating another idling superoperator, we use the compact form shown in Fig. 17, with the same number of rows as the WT4 superoperator. The



Error	GHZ Success	Meas. Error	Plaquette (Z)	Vertex (X)	Idle
IIII	TRUE	FALSE	0.99821944400618 15	0.99821944400618 15	0.499678796560266 6
IIII	TRUE	TRUE	0.00068176689417 16804	0.00068176689417 16755	0.499678796560266 6
IIII	FALSE	FALSE	4.497149643388714 e-06	4.49714964338871e -06	4.49714964338871e 06
IIII	FALSE	TRUE	4.497149643388714 e-06	4.49714964338871e -06	4.49714964338871e 06
IIIX	TRUE	FALSE	4.07683288902953 96e-05	4.77385864357036 17e-05	2.638568278730491e -05
IIIX	TRUE	TRUE	1.36526009933034 35e-05	2.00026385541906 8e-05	2.638568278730491e -05
IIIX	FALSE	FALSE	2.37473282345196 4e-10	2.37473282345196 4e-10	2.374732823451964e -10

FIG. 17. Application of data qubit errors on the WT3 code lattice, using the tabular superoperator calculated from Sec. B2. We show a  $R_1^Z$  stabilizer unit cell as an example where we apply the errors on data qubits of the current  $R_1^Z$  stabilizer and idling errors on other data qubits in the unit cell.

simulation works as follows. If we again consider the  $R_1^Z$  stabilizer, and we sample {IIII, TRUE, TRUE} for the "Plaquette (Z)" (shown in light-yellow), we can apply the noise on data qubits 1,2,3,4, following the same argument as WT4 simulations. However, we must also apply the idling noise on the idling data qubits 5,6,7,8. Given that the stabilizer has a GHZ success, we now sample using the "Idle" column only from the rows that have "GHZ Success = TRUE" (shown in red). Say we sampled the error configuration "IIIX", in which case we will serially apply this configuration to the idling data qubits (in the order 5,6,7,8). We loop over all the stabilizer unit cells within a sub-round to apply all the data qubit errors, and we repeat this for all the sub-rounds for each type of stabilizer. This completed one layer of measurements in the QEC cycle. After applying all the data qubit errors, we measure the layer, including the measurement errors that were previously recorded for each stabilizer. Finally, again, we do perfect measurements in the final layer and send the 3D syndrome graph to the decoder.

## 3. Flag fault-tolerance of the WT3 architecture

In the main text, we briefly mentioned that the bare stabilizer circuit of the WT3 architecture is not fault-tolerant as an undetectable weight-2 (two-qubit) error propagation is possible with only a weight-1 (single qubit) error within each module. This error propagation

is shown in Fig. 18(a). An  $X$  error can propagate from the communication qubit to both data qubits within the module, which goes undetectable. This error propagation can be detected using a flag qubit [76]. The error is intentionally propagated to the flag qubit, where it is detected upon the measurement. This flagged stabilizer

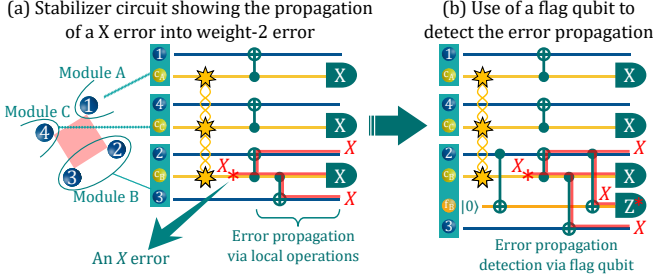


FIG. 18. Detection of error propagation (hook errors) using flag qubit within one module (Module B) of WT3 architecture stabilizer. (a) Shows the example of an  $X$  error on a communication qubit ( $c_B$ ) that propagates to two data qubits (2 & 3) within one module via local CNOT operations. (b) Depicts the usage of additional memory qubit (auxiliary) as flag qubit ( $f_B$ ) where the error also propagates to the flag qubit (initialized in  $|0\rangle$ ) and is detected via its  $Z$  measurement flip (shown as  $Z^*$ ).

circuit (Fig. 18(b)) can be used after the logical initialization (in the first layer of the first QEC cycle) of the code to detect such hook errors. Please note that this circuit does not provide a unique detection pattern for this error because, for instance, an  $X$  error on qubit-2 after the first CNOT would also lead to the same detection pattern (flip of  $f_B$  measurement outcome). However, detecting such errors helps to decode errors better as this information can be combined with additional syndrome data to improve the decoding. For instance, in case of a hook error (as shown), another  $Z$ -stabilizer of qubit-3 will also flip, and this condition can be pre-programmed in the decoder to improve the logical error rates of the surface code. However, for the scope of this work, we only limit ourselves to simulating the unflagged version of the WT3 architecture.

#### 4. Simultaneous stabilizer measurements vs. sub-round structure

A natural question arises: what is the impact of dividing the stabilizer measurement round into sub-rounds on decoding the QEC code? In a monolithic architecture, all the stabilizers in each layer are measured simultaneously via intertwined stabilizer circuits [55, 84]. We can consider a small example in the case of perfect measurements. For two neighboring  $Z$  type stabilizers  $Z_{abcd}$  and  $Z_{befg}$ , any incoming error  $X_b$  will flip both the stabilizers and is trivial to correct for the decoder. However, if we first measure  $Z_{abcd}$  in the first sub-round and  $Z_{befg}$  in the second sub-round, there may be  $X_b$  error that can

occur between the two sub-rounds, triggering only the later  $Z_{befg}$  stabilizer. This deceives the decoder to infer that a measurement error as occurred on one of the communication qubits b,e,f,g. Thereby missing the data qubit error correction via  $X_b$  and increasing the  $X$ -logical error probability. This kind of error occurs more often in the WT3 architecture as it has twice the number of sub-rounds, which makes catching easy recovery configurations challenging for the decoder. More detailed analytical or numerical analysis of these errors is beyond the scope of this present work, and we leave this for future work.

## Appendix D: Emission based scheme and distillation protocols

This section provides a full analytical treatment of the emission-based scheme and its performance evaluation in the presence of circuit-level noise. We first describe the entanglement generation through a Bell-pair between two modules via the single-click protocol [57].

### 1. Single-click protocol

Consider two modules as identical emitter setups, A and B, where each emitter (the communication qubit of each module acts as the emitter qubit) can be initialized in the arbitrary state

$$|\Psi\rangle_{\text{init}}^{A/B} = \sqrt{1-\alpha}|0\rangle + \sqrt{\alpha}|1\rangle \quad (\text{D1})$$

where  $\alpha$  is the bright state population parameter. This state can be initialized for each emitter with fidelity  $F_{\text{prep}}$ . This gives the density matrix

$$\begin{aligned} \rho_{\text{init}}^{A/B} = & (1-\alpha)|0\rangle\langle 0| + (2F_{\text{prep}}-1)\sqrt{\alpha(1-\alpha)}|0\rangle\langle 1| \\ & + (2F_{\text{prep}}-1)\sqrt{\alpha(1-\alpha)}|1\rangle\langle 0| + \alpha|1\rangle\langle 1| \end{aligned} \quad (\text{D2})$$

where the preparation infidelity noise is modelled as a dephasing channel over the state. Each of the emitters is now excited via a  $\pi$ -pulse, which causes the bright state  $|1\rangle$  to emit a photon ( $|1\rangle \rightarrow |11_{\text{ph}}\rangle$ ) while the dark state  $|0\rangle$  does not lead to any emission ( $|0\rangle \rightarrow |00_{\text{ph}}\rangle$ ), where the second ket is for the photon number, denoted with subscript 'ph'. The resulting density matrix for each emitter-photon is

$$\begin{aligned} \rho_{\text{emit}}^{A/B} = & (1-\alpha)|00_{\text{ph}}\rangle\langle 00_{\text{ph}}| + (2F_{\text{prep}}-1)\sqrt{\alpha(1-\alpha)} \\ & |00_{\text{ph}}\rangle\langle 11_{\text{ph}}| + (2F_{\text{prep}}-1)\sqrt{\alpha(1-\alpha)}|11_{\text{ph}}\rangle\langle 00_{\text{ph}}| \\ & + \alpha|11_{\text{ph}}\rangle\langle 11_{\text{ph}}| \end{aligned} \quad (\text{D3})$$

However, there could be an excitation error due to the application of this excitation pulse, which can occur due to

an extra photon being emitted or unintentionally exciting the dark state. We describe this as excitation error probability  $p_{EE}$ , and this phenomenon is modeled as a dephasing channel applied to either the emitter or the emitted photon state. The resulting density matrix is

$$\begin{aligned} \rho_{\text{emit}}^{\text{A/B}} = & (1 - \alpha)|00_{\text{ph}}\rangle\langle 00_{\text{ph}}| + (2F_{\text{prep}} - 1)(1 - 2p_{EE}) \\ & \sqrt{\alpha(1 - \alpha)}|00_{\text{ph}}\rangle\langle 11_{\text{ph}}| + (2F_{\text{prep}} - 1)(1 - 2p_{EE}) \\ & \sqrt{\alpha(1 - \alpha)}|11_{\text{ph}}\rangle\langle 00_{\text{ph}}| + \alpha|11_{\text{ph}}\rangle\langle 11_{\text{ph}}| \end{aligned} \quad (\text{D4})$$

for each emitter-photon setup. After this step, the flying photons are sent to a middle station where both photons are interfered with via a beam splitter. However, there is noise in the fiber, which carries the photons.

We consider the phase uncertainty  $\lambda$  due to the path length difference between the interferometer's two arms. This can be realized as a dephasing channel with some error probability  $\lambda$ . This is calculated as:

$$\lambda = \frac{1}{2} \left( 1 + \frac{I_1(\sigma(\varphi)^{-2})}{I_0(\sigma(\varphi)^{-2})} \right) \quad (\text{D5})$$

Where  $I_0$  and  $I_1$  are modified Bessel functions of the zeroth and first order, and  $\sigma(\varphi)$  is the standard deviation of the phase instability. Typically, this value is around 0.984 [25, 69, 70] for the relevant phase uncertainty in the recent experiments. This dephasing channel is applied to one of the photons (the one from emitter A). Then we obtain

$$\begin{aligned} \rho_{\text{em-ph}}^{\text{A}} = & (1 - \alpha)|00_{\text{ph}}\rangle\langle 00_{\text{ph}}| + (2F_{\text{prep}} - 1)(1 - 2p_{EE}) \\ & (2\lambda - 1)\sqrt{\alpha(1 - \alpha)}|00_{\text{ph}}\rangle\langle 11_{\text{ph}}| + (2F_{\text{prep}} - 1) \\ & (1 - 2p_{EE})(1 - 2\lambda)\sqrt{\alpha(1 - \alpha)}|11_{\text{ph}}\rangle\langle 00_{\text{ph}}| \\ & + \alpha|11_{\text{ph}}\rangle\langle 11_{\text{ph}}| \end{aligned} \quad (\text{D6})$$

Moreover, as the fiber is also noisy, we have photon loss through the fiber. We combine this effect with also the photon detector efficiency. Each excitation's total photon detection probability is parameterized by  $\eta_{\text{ph}}$ . This is a product of the total transmissivity between the emitter and the photon detector (accounts for photon loss), the detector efficiency, and the probability that the desired photon is emitted during the detection time window and within the zero-phonon line of the emitter. We model this overall effect as an amplitude-damping channel on both the emitter photons. The Kraus operators for the amplitude damping (AD) channel are:

$$K_1^{\text{AD}} = \begin{bmatrix} 1 & 0 \\ 0 & \sqrt{\eta_{\text{ph}}} \end{bmatrix}, \quad K_2^{\text{AD}} = \begin{bmatrix} 0 & \sqrt{1 - \eta_{\text{ph}}} \\ 0 & 0 \end{bmatrix} \quad (\text{D7})$$

According to Eqn. A3, operating with the amplitude-damping channel on the emitted photons from both the modules, we get the output states before the photon de-

tection as:

$$\begin{aligned} \rho_{\text{em-ph}}^{\text{A}} = & (1 - \alpha)|00_{\text{ph}}\rangle\langle 00_{\text{ph}}| + (2F_{\text{prep}} - 1)(1 - 2p_{EE}) \\ & \sqrt{\eta_{\text{ph}}}(2\lambda - 1)\sqrt{\alpha(1 - \alpha)}|00_{\text{ph}}\rangle\langle 11_{\text{ph}}| + \alpha(1 - \eta_{\text{ph}}) \\ & |10_{\text{ph}}\rangle\langle 10_{\text{ph}}| + (2F_{\text{prep}} - 1)(1 - 2p_{EE})\sqrt{\eta_{\text{ph}}}(1 - 2\lambda) \\ & \sqrt{\alpha(1 - \alpha)}|11_{\text{ph}}\rangle\langle 00_{\text{ph}}| + \alpha\eta_{\text{ph}}|11_{\text{ph}}\rangle\langle 11_{\text{ph}}| \end{aligned} \quad (\text{D8})$$

$$\begin{aligned} \rho_{\text{em-ph}}^{\text{B}} = & (1 - \alpha)|00_{\text{ph}}\rangle\langle 00_{\text{ph}}| + (2F_{\text{prep}} - 1)(1 - 2p_{EE}) \\ & \sqrt{\eta_{\text{ph}}}\sqrt{\alpha(1 - \alpha)}|00_{\text{ph}}\rangle\langle 11_{\text{ph}}| + \alpha(1 - \eta_{\text{ph}})|10_{\text{ph}}\rangle\langle 10_{\text{ph}}| \\ & + (2F_{\text{prep}} - 1)(1 - 2p_{EE})\sqrt{\eta_{\text{ph}}}\sqrt{\alpha(1 - \alpha)}|11_{\text{ph}}\rangle\langle 00_{\text{ph}}| \\ & + \alpha\eta_{\text{ph}}|11_{\text{ph}}\rangle\langle 11_{\text{ph}}| \end{aligned} \quad (\text{D9})$$

For the photon detector, we assume the regime with negligible dark count probability, similar to other schemes, about  $10^{-6}$ , and we neglect it. We consider the photon indistinguishability  $\mu$  for the joint Bell-pair measurement for the perfect interference. The measurement projector for the two-photon measurement can be described with the following POVMs acting only on the photonic degrees of freedom [72].

$$\begin{aligned} E_{00} = & |0_{\text{ph}}0_{\text{ph}}\rangle\langle 0_{\text{ph}}0_{\text{ph}}| \\ E_{01} = & \frac{1}{2} \left( \frac{\sqrt{1 + \sqrt{\mu}} + \sqrt{1 - \sqrt{\mu}}}{\sqrt{2}} (|0_{\text{ph}}1_{\text{ph}}\rangle\langle 0_{\text{ph}}1_{\text{ph}}| \right. \\ & + |1_{\text{ph}}0_{\text{ph}}\rangle\langle 1_{\text{ph}}0_{\text{ph}}|) + \frac{\sqrt{1 - \sqrt{\mu}} - \sqrt{1 + \sqrt{\mu}}}{\sqrt{2}} \\ & (|0_{\text{ph}}1_{\text{ph}}\rangle\langle 1_{\text{ph}}0_{\text{ph}}| + |1_{\text{ph}}0_{\text{ph}}\rangle\langle 0_{\text{ph}}1_{\text{ph}}|) \\ & \left. + \sqrt{1 + \mu}|1_{\text{ph}}1_{\text{ph}}\rangle\langle 1_{\text{ph}}1_{\text{ph}}| \right) \\ E_{10} = & \frac{1}{2} \left( \frac{\sqrt{1 + \sqrt{\mu}} + \sqrt{1 - \sqrt{\mu}}}{\sqrt{2}} (|0_{\text{ph}}1_{\text{ph}}\rangle\langle 0_{\text{ph}}1_{\text{ph}}| \right. \\ & + |1_{\text{ph}}0_{\text{ph}}\rangle\langle 1_{\text{ph}}0_{\text{ph}}|) + \frac{\sqrt{1 + \sqrt{\mu}} - \sqrt{1 - \sqrt{\mu}}}{\sqrt{2}} \\ & (|0_{\text{ph}}1_{\text{ph}}\rangle\langle 1_{\text{ph}}0_{\text{ph}}| + |1_{\text{ph}}0_{\text{ph}}\rangle\langle 0_{\text{ph}}1_{\text{ph}}|) \\ & \left. + \sqrt{1 + \mu}|1_{\text{ph}}1_{\text{ph}}\rangle\langle 1_{\text{ph}}1_{\text{ph}}| \right) \\ E_{11} = & \frac{\sqrt{1 - \mu}}{\sqrt{2}} |1_{\text{ph}}1_{\text{ph}}\rangle\langle 1_{\text{ph}}1_{\text{ph}}| \end{aligned} \quad (\text{D10})$$

Here  $E_{00}$  corresponds to no photon detection.  $E_{01}$  and  $E_{10}$  correspond to one photon detected in the right and left detector, respectively. And  $E_{11}$  means two photons being detected, one at each detector. For the successful entanglement generation, we herald on a single click, that is, one photon being detected at either the right or left detector. For a left/right detector click (via  $E_{10}/E_{01}$ ),

the output states would be

$$\rho_{\text{out}}^{\text{left/right}} = \frac{(\mathbb{I} \otimes E_{10/01})(\rho_{\text{em-ph}}^{\text{A}} \otimes \rho_{\text{em-ph}}^{\text{B}})(\mathbb{I} \otimes E_{10/01})^\dagger}{\text{Tr}[(\mathbb{I} \otimes E_{10/01})(\rho_{\text{em-ph}}^{\text{A}} \otimes \rho_{\text{em-ph}}^{\text{B}})(\mathbb{I} \otimes E_{10/01})^\dagger]} \quad (\text{D11})$$

where the tensor product  $\rho_{\text{em-ph}}^{\text{A}} \otimes \rho_{\text{em-ph}}^{\text{B}}$  follows the order  $|\text{emitter-1}\rangle|\text{emitter-2}\rangle|\text{photon-1}\rangle|\text{photon-2}\rangle$ . And we identify the denominator as the success probability  $P_{\text{single}}^{\text{left/right}}$  of the respective single-click. We get the raw output entangled state after performing a partial trace over the photons:

$$\begin{aligned} \rho_{\text{out}}^{\text{left}} = & \frac{1}{4 + \alpha\eta_{\text{ph}}(\mu - 3)} \left( 2(1 - \alpha)|01\rangle\langle 01| \right. \\ & + 2(2F_{\text{prep}} - 1)^2(1 - 2p_{\text{EE}})^2(1 - \alpha)(2\lambda - 1)\sqrt{\mu}(|01\rangle\langle 10| \\ & + |10\rangle\langle 01|) + 2(1 - \alpha)|10\rangle\langle 10| + \alpha(4 + \eta_{\text{ph}}(\mu - 3)) \\ & \left. |11\rangle\langle 11| \right) \end{aligned} \quad (\text{D12})$$

$$\begin{aligned} \rho_{\text{out}}^{\text{right}} = & \frac{\alpha\eta_{\text{ph}}}{2} \left( (1 - \alpha)|01\rangle\langle 01| + (2F_{\text{prep}} - 1)^2 \right. \\ & (1 - 2p_{\text{EE}})^2(1 - \alpha)(1 - 2\lambda)\sqrt{\mu}(|01\rangle\langle 10| + |10\rangle\langle 01|) \\ & \left. + (1 - \alpha)|10\rangle\langle 10| + \frac{\alpha}{2}(4 + \eta_{\text{ph}}(\mu - 3))|11\rangle\langle 11| \right) \end{aligned} \quad (\text{D13})$$

To convert these states into the desired Bell-state  $|\Psi^+\rangle$  we apply an  $X^c$  gate to one of the emitters and apply a phase correction on one of the emitters if the right detector clicks. Both these gates are noisy and characterized by depolarization noise with gate error  $p_g$ . We include gate error for the post-correction gates, in contrast, to Ref. [25]. This gives the corrected output density matrices  $\rho_{\text{final}}^{\text{left}}$  and  $\rho_{\text{final}}^{\text{right}}$ .

$$\begin{aligned} \rho_{\text{final}}^{\text{left}} &= (X^c \otimes \mathbb{I})\rho_{\text{out}}^{\text{left}}(X^c \otimes \mathbb{I}) \\ \rho_{\text{final}}^{\text{right}} &= (X^c \otimes Z^c)\rho_{\text{out}}^{\text{right}}(X^c \otimes Z^c) \end{aligned} \quad (\text{D14})$$

The average density matrix from the single click protocol is, therefore:

$$\begin{aligned} \rho_s = & P_{\text{single}}^{\text{left}}(\mathcal{N}_{\text{gate}}^{\text{single-qubit}} \otimes \mathbb{I})\rho_{\text{final}}^{\text{left}}(\mathcal{N}_{\text{gate}}^{\text{single-qubit}} \otimes \mathbb{I}) \\ & + P_{\text{single}}^{\text{right}}(\mathcal{N}_{\text{gate}}^{\text{single-qubit}} \otimes \mathcal{N}_{\text{gate}}^{\text{single-qubit}})\rho_{\text{final}}^{\text{right}} \\ & (\mathcal{N}_{\text{gate}}^{\text{single-qubit}} \otimes \mathcal{N}_{\text{gate}}^{\text{single-qubit}}) \end{aligned} \quad (\text{D15})$$

It turns out that  $P_{\text{single}}^{\text{left}} = P_{\text{single}}^{\text{right}}$  and the total success probability of the single-click protocol is the sum of both:

$$P_{\text{single}}^{\text{succ}} = \frac{1}{2}\alpha\eta_{\text{ph}}(4 - \alpha\eta_{\text{ph}}(3 - \mu)) \quad (\text{D16})$$

We calculate the overall fidelity of the single-click protocol as

$$F_{\text{single}} = \text{Tr} \left[ \sqrt{\sqrt{\Phi^+} \rho_s \sqrt{\Phi^+}} \right] \quad (\text{D17})$$

where  $\Phi^+ = |\Phi^+\rangle\langle\Phi^+|$  is the target Bell-pair density matrix. The full-analytical expression of the average fidelity is:

$$\begin{aligned} F_{\text{single}} = & \frac{\alpha\eta_{\text{ph}}}{36P_{\text{single}}^{\text{succ}}} \left( 36(1 - \alpha)(1 + \phi) + (9p_g - 4p_g^2)(36\phi \right. \\ & \left. - 4\alpha(8 + \eta_{\text{ph}}(\mu - 3))) \right) \end{aligned} \quad (\text{D18})$$

where

$$\phi = \sqrt{\mu}(2F_{\text{prep}} - 1)^2(2\lambda - 1)(1 - p_{\text{EE}})^2 \quad (\text{D19})$$

captures the overall noise in the photon generation and detection.

## 2. Double click protocol

The raw output state ( $\rho_{\text{out}}^{\text{left/right}}$ ) from the single-click protocol has a contribution from the pure bright-state term  $|11\rangle\langle 11|$ , which leads to an overall mixed state. See Eqn. D12 and Eqn. D13. Double-click (Barrett-Kok) protocol eliminates this term by the application of  $X^c$  gate on each emitter on the raw output state after the single click. Another round of single-click protocol is performed and heralded on the consecutive single-click. This eliminates the  $|00\rangle\langle 00|$  term (after  $X^c$  gates) because it does not emit photons in the second round. The detection pattern now has four possibilities: left  $\otimes$  left, left  $\otimes$  right, right  $\otimes$  left, and right  $\otimes$  right, as the photon detector click patterns. However, for the double-click protocol [58], we initialize the initial state with  $\alpha = 1/2$ , and the phase uncertainty  $\lambda$  gets eliminated due to the symmetry of the protocol. The total success probability for the double-click protocol is:

$$P_{\text{double}}^{\text{succ}} = \sum_{\text{a}} \left( P_{\text{single}}^{\text{a}} P_{\text{single}}^{\text{a}\otimes\text{a}} + P_{\text{single}}^{\text{a}} P_{\text{single}}^{\text{a}\otimes\bar{\text{a}}} \right) \quad (\text{D20})$$

where  $\text{a} \in \{\text{left}, \text{right}\}$ , and  $\bar{\text{left}} = \text{right}$ , and vice versa. All these terms are equal, and we get the total probability with post-correction with single-qubit gates as:

$$P_{\text{double}}^{\text{succ}} = \frac{\eta_{\text{ph}}^2}{36} \left( 18 + 12p_g(2 + \eta_{\text{ph}}(\mu - 3)) + p_g^2\eta_{\text{ph}}^2(\mu - 3)^2 \right) \quad (\text{D21})$$

This expression reduces to  $\eta_{\text{ph}}^2/2$  without gate error, as considered in Ref. [25]. The full analytical expression for the average fidelity of the double-click protocol is:

$$\begin{aligned} F_{\text{double}} = & 3p_g(-54(1 + \eta) + p_g(96 + 36\eta + p_g(-32 - (-9 \\ & + 4p_g)\eta(-8 + 3\eta)))) + 2p_g(2(1 - 2F_{\text{prep}})^2(1 - 2p_{\text{EE}})^4 \\ & (-189 + 4p_g(81 + 4p_g(-15 + 4p_g))) + (27 - 2p_g(9 \\ & + 2p_g(-9 + 4p_g)))\eta + 3p_g^2(-9 + 4p_g))\mu + (9 - 4p_g) \\ & p_g^3\eta^2\mu^2 + 162(1 + (1 - 2F_{\text{prep}})^2(1 - 2p_{\text{EE}})^4\mu)/18(18 + \\ & p_g(24 + \eta(12 + p_g\eta(-3 + \mu))(-3 + \mu))) \end{aligned} \quad (\text{D22})$$

We recover the limiting case stated in Ref. [25] of  $p_g = 0$ ,  $F_{\text{double}} = (1 + \phi^2)/2$ , given  $\lambda = 1$ .

### 3. Single-click versus double-click

The  $P_{\text{succ}}^{\text{link}}$  for single-click protocol depends on bright state parameter  $\alpha$ , and changing this parameter has a tradeoff between fidelity and success probability. This is evident from Eqn. D16 and Eqn. D18. For double-click, the  $P_{\text{succ}}^{\text{link}}$  is quadratically dependent on the effective photon detection probability  $\eta_{\text{ph}}$ , which is very small (for the NTP) and therefore unfavorable for threshold performance. Through the single-click protocol, the  $P_{\text{succ}}^{\text{link}}$  is linear in  $\eta_{\text{ph}}$  (which is higher) and we can trade in some  $P_{\text{succ}}^{\text{link}}$  to reduce the infidelity of the Bell state, and satisfy the numerical bounds on  $P_{\text{succ}}^{\text{link}}$  and fidelity as discussed in the results section. However, the fidelity was still low (less than 0.90) for the existence of a threshold (inclusive of the physical gate error), even for very low values of  $\alpha$ . A similar exploration was also done in Ref. [25] on single-click vs. the double-click protocol without the gate error. In this view, we use the single-click protocol for NTP and double-click for FP to optimize the logical error rates in these regimes.

### 4. Fusion and distillation protocols

In this subsection, we give explicit examples of the EM fusion protocols for which we found a threshold. These protocols were searched using the ‘dynamic program’ first introduced in Ref. [85] and later used in Ref. [25]. We searched the GHZ fusion and distillation protocols pool of WT4 and WT3 GHZ states for maximum stabilizer fidelity output. Following that, a threshold calculation was run for a set of the best protocols chosen based on stabilizer fidelity. Finally, the protocol with the highest threshold and least logical error rates was chosen for each case. These are the protocols we showcase in Fig. 19, for which we obtained thresholds. Using these binary tree diagrams, we sketch the operations involved in the GHZ creation chronologically via the EM protocol. Details of the protocol operations are provided in the caption of Fig. 19. It consists of elementary Bell-pair generation between the modules and their distillation and fusion with other modules. For each protocol, we report the maximum number of Bell-pairs used as its  $k$  value and the maximum number of memory qubits used by a node for that protocol (this includes memory qubits used as data qubits). In all these protocols, the maximum number of auxiliary qubits used is two, but WT4 architecture has one data qubit per node, while WT3 architecture has two data qubits per node. There are two extra coherence times parameter sets for which we obtained thresholds. These are not part of the main script, but we motivate these (Set-mix and Set-D) in App. I and App. H.

## Appendix E: Reflection scheme

Here, we describe the reflection scheme. We consider the scattering of a photonic time-bin qubit from a single spin-coupled cavity and then generalize this to the case where the photon scatters off multiple cavities. The spin is initialized in the  $|0\rangle$  state, and the photonic state is an equal superposition of the early and late time-bin states. Hence, the photon-spin state is  $\frac{1}{\sqrt{2}}(|E0\rangle + |L0\rangle)$ .

Let  $r_0$  and  $r_1$  denote the photonic reflection coefficients corresponding to the cases when the spin is in the uncoupled state  $|0\rangle$  and coupled state  $|1\rangle$ , respectively. After the early time-bin component of the photon scattered, the unnormalized state of the system becomes  $\frac{1}{\sqrt{2}}(r_0|E0\rangle + |L0\rangle)$ . Then, a Hadamard gate is executed on the spin, which transforms the direct product state into  $\frac{1}{\sqrt{2}}(r_0|E+\rangle + |L+\rangle)$ . Next, the late-time-bin component of the photon is scattered, and the state of the system becomes  $\frac{1}{\sqrt{2}}\left(r_0|E+\rangle + \frac{1}{\sqrt{2}}\left(r_0|L0\rangle + r_1|L1\rangle\right)\right)$ . Finally, a second Hadamard gate is executed on the spin, and the state of the system becomes

$$|\Psi_1\rangle = \frac{1}{\sqrt{2}}\left(r_0|E0\rangle + \frac{r_0 + r_1}{2}|L0\rangle + \frac{r_0 - r_1}{2}|L1\rangle\right). \quad (\text{E1})$$

For multiple cavities, the above procedure generalizes straightforwardly. Consequently, the final state of the multiple spin qubits and the photon will be

$$|\Psi_N\rangle = \frac{1}{\sqrt{2}}\left[r_0^n|E\rangle|0\rangle^{\otimes n} + |L\rangle\left(\frac{r_0 + r_1}{2}|0\rangle + \frac{r_0 - r_1}{2}|1\rangle\right)^{\otimes n}\right], \quad (\text{E2})$$

where  $n$  is the number of the spins.

At the final step, an optical switch and a delay line are used to measure the photon in the X basis ( $|\pm\rangle_{\text{ph}} = (|E\rangle \pm |L\rangle)/\sqrt{2}$ ). If the photon is detected in the  $|+\rangle_{\text{ph}}$  state, the spins will be projected into an (unnormalized) state

$$|\Psi_+\rangle = \frac{1}{2}\left[r_0^n|0\rangle^{\otimes n} + \left(\frac{r_0 + r_1}{2}|0\rangle + \frac{r_0 - r_1}{2}|1\rangle\right)^{\otimes n}\right]. \quad (\text{E3})$$

One can see from Eqn. (E3) that, when  $r_0 \approx -r_1$ , it resembles the GHZ state  $|\text{GHZ}\rangle = (|0\rangle^{\otimes n} + |1\rangle^{\otimes n})/\sqrt{2}$ . If the photon is detected in the  $|-\rangle$  state, the spins will be projected into a state

$$|\Psi_-\rangle = \frac{1}{2}\left[r_0^n|0\rangle^{\otimes n} - \left(\frac{r_0 + r_1}{2}|0\rangle + \frac{r_0 - r_1}{2}|1\rangle\right)^{\otimes n}\right]. \quad (\text{E4})$$

In this case, when  $r_0 \approx -r_1$ , the resulting state is close to the state  $(|0\rangle^{\otimes n} - |1\rangle^{\otimes n})/\sqrt{2}$ . In this case, a Z gate

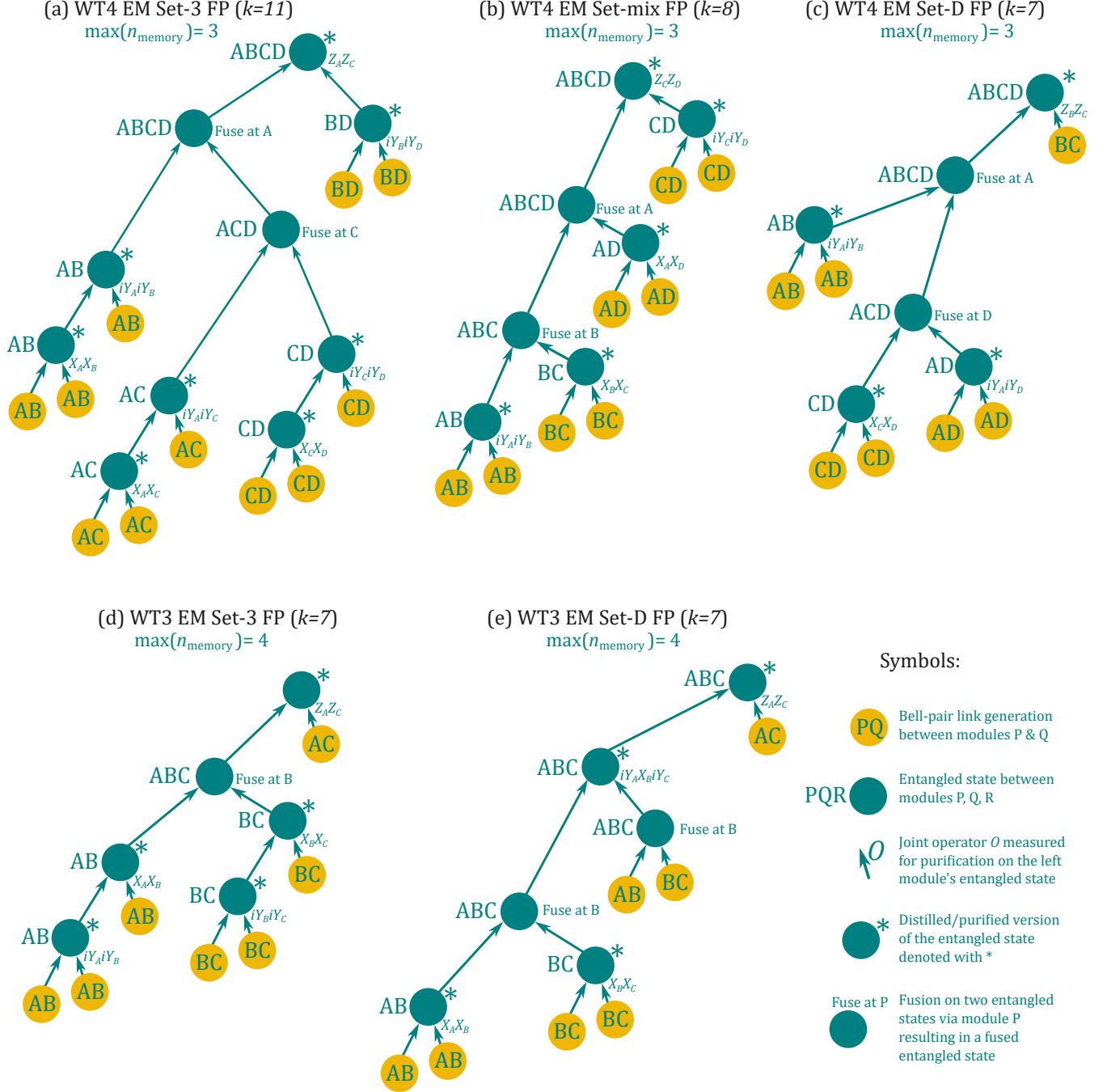


FIG. 19. Optimised emission-based (EM) scheme fusion and distillation protocols for various architectures and schemes, for which we obtained (highest) thresholds. We sketch these protocols as binary-tree diagrams, similar to Ref. [25], with time running vertically up. We also show optimized protocols for two extra coherence time sets, namely Set-mix and Set-D, introduced in App. I and App. H. (a), (b) and (c) show the protocols for WT4 architecture, while (d) and (e) show protocols for WT3 architecture. The total number of Bell-pairs used in a fusion protocol is shown as its  $k$  value. These protocols consist of operations such as the Bell-pair generation (via double-click protocol for all these examples), the fusion of Bell-pair with other entangled states to increase the weight of the resulting entangled state distributed between the modules, and purification/distillation operations by measuring some joint operators (stabilizers of that entangled state). Through these protocols, the total number of memory qubit requirements can be estimated for each case. We show the maximum number of memory qubits required (including the data qubits) for each reported protocol below its label.

can be applied on the first spin qubit to recover the state  $|\text{GHZ}\rangle$ . Note that the states in Eqs. (E3)-(E4) are not normalized. The sum of the norms of these two states gives the success probability of the protocol in the absence of additional photon loss:

$$P_{\text{succ}}^{\text{GHZ}} = \langle \Psi_+ | \Psi_+ \rangle + \langle \Psi_- | \Psi_- \rangle. \quad (\text{E5})$$

The reflection coefficients,  $r_0$  and  $r_1$  can be expressed in terms of the different spin-photon interface parameters as [86]:

$$r_{1,0} = 1 - \frac{2 \frac{\kappa_c}{\kappa_c + \kappa_1}}{1 + 2i \frac{\omega}{\kappa_c + \kappa_1} + \frac{4C_1}{1 + 2i\delta_{1,0}/\gamma}}, \quad (\text{E6})$$

where  $\delta_0$  and  $\delta_1$  are the detunings between the corresponding spin transition and the input photon frequency and  $\omega$  is the detuning between the cavity resonance frequency and the input photon. The two spin transitions have a fixed detuning  $\Delta$  hence  $\delta_0 - \delta_1 = \Delta$  (see Fig. 8 in the main text).

To determine the optimal performance, we optimize these two detunings and find a region where the fidelity of the GHZ state reaches a global maximum while the success rate is nearly flat, as shown in Fig. 20 and Fig. 21. Hence, the location of the maximum fidelity of the GHZ state determines the optimum values of  $\omega$  and  $\delta$  as listed in the table in Fig. 8 in the main text. For the simulation of the surface code performance, our simulation also includes faulty Hadamard gates and Z gates as well as additional photon loss from e.g. the optical circulators.

### Appendix F: Carving scheme with single photon source

Here, we describe our model of the carving protocol with a perfect single-photon source in more detail. For simplicity, we first consider a setup with only two spins, one at the upper and one at the lower optical route. We will later generalize to more spins. The initial state of the spin reads  $|\psi_0\rangle = \frac{1}{2}(|00\rangle + |01\rangle + |10\rangle + |11\rangle) = \frac{1}{2}(1, 1, 1, 1)^T$ . When the first photon from the single-photon source passes the first beam splitter, it turns into a superposition state  $\frac{1}{\sqrt{2}}(|U\rangle + |D\rangle)$ , where  $|U\rangle$  is the photon state traveling along the upper route and  $|D\rangle$  the lower route. The unnormalized state describing the transmission of the photon through the spin-cavity systems is:

$$|\psi_1^{\text{pre}}\rangle = \frac{1}{2\sqrt{2}} \left[ \begin{pmatrix} t_0 \\ t_0 \\ t_1 \\ t_1 \end{pmatrix} |U\rangle + \begin{pmatrix} t_0 \\ t_1 \\ t_0 \\ t_1 \end{pmatrix} |D\rangle \right] \quad (\text{F1})$$

where  $t_0$  and  $t_1$  are transmission coefficients for the  $|0\rangle$  and  $|1\rangle$  states of the spins, respectively.

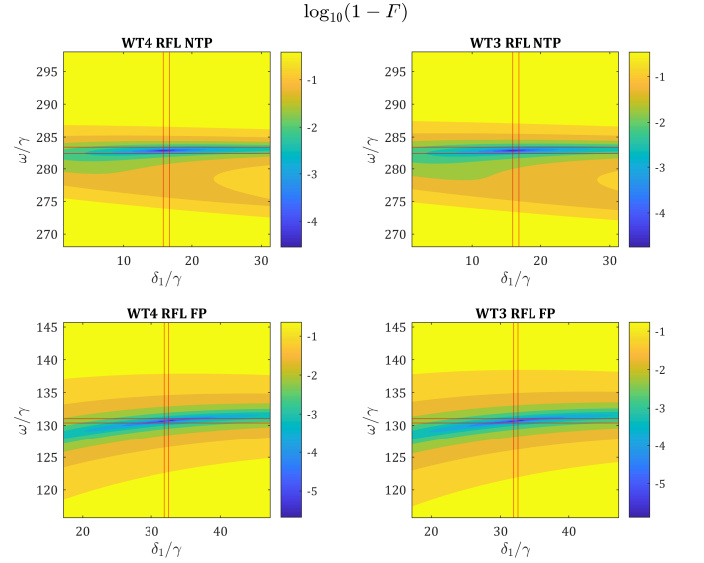


FIG. 20. Scanning of the base-10 logarithm of the infidelity of the GHZ state over the variables of  $\omega$  and  $\delta_1$ . The subtitles of the figures denote different cases of state-of-the-art parameters NTP and FP for WT4 and WT3 GHZ states. The found optimum  $\omega$  and  $\delta_1$  and their deviations of  $\sigma/\gamma$  are indicated with the two horizontal and two vertical red lines with the same separations of  $2\sigma/\gamma$ . The gate error is set to 0 in this calculation.

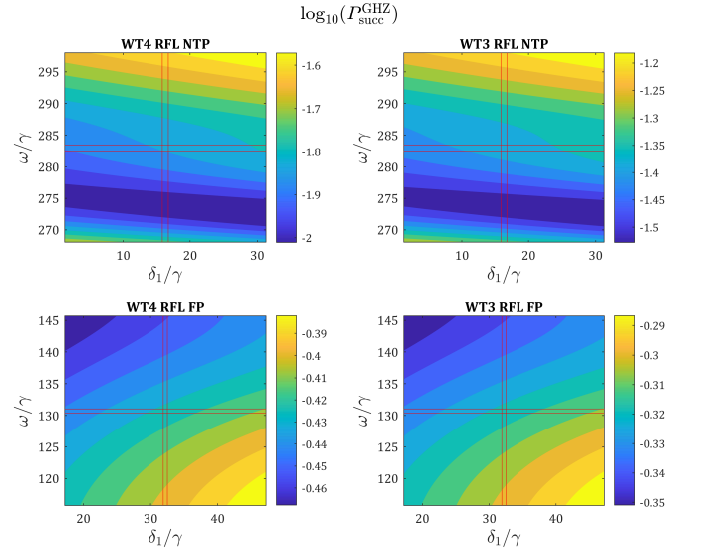


FIG. 21. Scanning of the base-10 logarithm of the success rate of the GHZ state generation over the variables of  $\omega$  and  $\delta_1$ . The plotting follows the same fashion as Fig. 20.

When the photon is detected after the second beam splitter, the state of the spins will be projected into

$$|\psi_1^+\rangle = \frac{1}{2} \begin{pmatrix} 2t_0 \\ t_0 + t_1 \\ t_0 + t_1 \\ 2t_1 \end{pmatrix} \quad (\text{F2})$$

if the photon is detected by detector  $d_+$  and

$$|\psi_1^-\rangle = \frac{1}{2} \begin{pmatrix} 0 \\ t_0 - t_1 \\ t_1 - t_0 \\ 0 \end{pmatrix} \quad (\text{F3})$$

if the photon is detected by detector  $d_-$ . We focus on the state  $|\psi_1^+\rangle$  state for now but a similar procedure is applied if the outcome is state  $|\psi_1^-\rangle$ . First, we apply NOT gates on the spins transforming the state to

$$|\psi_1^{+\text{NOT}}\rangle = \frac{1}{2} \begin{pmatrix} 2t_1 \\ t_0 + t_1 \\ t_0 + t_1 \\ 2t_0 \end{pmatrix}. \quad (\text{F4})$$

We then attempt to transmit a second photon. Assuming again that the second photon is transmitted and detected by detector  $d_+$ , the spin state is projected to

$$|\psi_2^{++}\rangle = \frac{1}{4} \begin{pmatrix} 2t_0 \\ t_0 + t_1 \\ t_0 + t_1 \\ 2t_1 \end{pmatrix} \odot \begin{pmatrix} 2t_1 \\ t_0 + t_1 \\ t_0 + t_1 \\ 2t_0 \end{pmatrix}, \quad (\text{F5})$$

where  $\odot$  is the symbol of the Hadamard product or element-wise product. Here one can see that if  $|t_0| \gg |t_1|$ , the normalized state  $|\psi_2^{++}\rangle$  will resemble a Bell state  $\frac{1}{\sqrt{2}}(0, 1, 1, 0)^T$ . This is also true for the other detection patterns up to single-qubit gate corrections. Note that the protocol is heralded by the detection of both photons. If either the first or the second photon is not detected, the protocol is re-initialized.

Above, we only considered the transmission and detection of two photons. However, more photons could be scattered in order to increase the fidelity of the state at the expense of a lower success probability. For the general case with  $n_{\text{wt}}$  spins and  $n_{\text{sc}}$  scattered photons, one can write an iterative relationship between the spin states after the  $(n_{\text{sc}} - 1)$ th and  $n_{\text{sc}}$ th scatterings as

$$|\psi_{n_{\text{sc}}}\rangle = \begin{cases} \mathbf{T} \odot |\psi_{n_{\text{sc}}-1}\rangle, & n_{\text{sc}} = 1. \\ \mathbf{T} \odot O_{\text{not}} |\psi_{n_{\text{sc}}-1}\rangle, & n_{\text{sc}} \geq 2. \end{cases} \quad (\text{F6})$$

where  $|\psi_{n_{\text{sc}}}\rangle$  is the spin state after  $n_{\text{sc}}$ th photon scatterings, and  $O_{\text{not}}$  is an operation with NOT gates on every spin. The  $\mathbf{T}$  is a vector of transmission coefficients defined as

$$\mathbf{T} = \begin{cases} \frac{\mathbf{t}_u + \mathbf{t}_d}{2}, & \text{photon detected by detector } d_+, \\ \frac{\mathbf{t}_u - \mathbf{t}_d}{2}, & \text{photon detected by detector } d_-, \end{cases} \quad (\text{F7})$$

where

$$\mathbf{t}_u = \begin{pmatrix} t_0 \\ t_1 \end{pmatrix}^{\otimes n_u} \otimes \begin{pmatrix} 1 \\ 1 \end{pmatrix}^{\otimes n_d} \quad (\text{F8})$$

$$\mathbf{t}_d = \begin{pmatrix} 1 \\ 1 \end{pmatrix}^{\otimes n_u} \otimes \begin{pmatrix} t_0 \\ t_1 \end{pmatrix}^{\otimes n_d} \quad (\text{F9})$$

where  $n_u$  and  $n_d$  are number of spins in the upper and lower optic routes, respectively.

After at least two rounds of photon scattering, the state of the spins will resemble the state  $(|111 \dots\rangle_u |000 \dots\rangle_l \pm |000 \dots\rangle_u |111 \dots\rangle_l) / \sqrt{2}$  with the  $\pm$  sign depending on the parity of the number of photons detected at detector  $d_-$ . To recover the GHZ state  $|\phi_+\rangle$ , NOT gates can be applied on the spins at one of the optical routes, and a Z gate may be used on one of the spins to correct the  $\pm$  sign. The corresponding gate errors will be added to the density matrix of the resulting GHZ state. The success possibility of the protocol is the trace of the unnormalized density matrix multiplied by the efficiency of the single photon detectors, single-photon source, and in/out coupling losses.

The different transmission coefficients  $t_0$  and  $t_1$  correspond to two different optical transitions. Therefore, the two transitions have different detuning,  $\delta_0$  and  $\delta_1$ , with respect to the input photons. For the cavity-included setup, according to Ref. [86], the transmission coefficient formula reads

$$t_{0,1}^{\text{cav}}(\delta) = \frac{\frac{2\kappa_c}{2\kappa_c + \kappa_1}}{1 + 2i\frac{\omega}{2\kappa_c + \kappa_1} + \frac{4C_2}{1 + 2i\delta_{0,1}/\gamma}}, \quad (\text{F10})$$

For the waveguide-included setup, according to Ref. [87], the transmission coefficient formula reads

$$t_{0,1}^{\text{wg}}(\delta) = \frac{1 + 2i\delta_{0,1}/\gamma}{1 + P + 2i\delta_{0,1}/\gamma}. \quad (\text{F11})$$

Notably, the  $t^{\text{wg}}$  can be viewed as  $t^{\text{cav}}$  when taking the limit of  $\kappa_c \rightarrow \infty$ .

The symbols in Eqn. (F10) and (F11) are explained in Fig. 9 and 10 in the main text.

To maximize the GHZ state fidelity,  $t(\delta_0)$  should take the maximum modulus and  $t(\delta_1)$  the minimum modulus. Besides, the two spin transitions have a fixed detuning  $\Delta$  hence  $\delta_0 - \delta_1 = \Delta$ . Based on these, the optimum values of  $\delta_1$  and  $\omega$  can be determined analytically which gives  $\delta_1 = 0$  for both the cavity and waveguide cases and  $\omega = \frac{4C_2\Delta(2\kappa_a + \kappa_c)}{1 + 4\Delta^2}$  for the cavity case. As in the reflection scheme,  $\delta_1$  and  $\omega$  are also assumed to fluctuate following Gaussian distributions with the same deviations  $\sigma$  around the optimal values. The density matrix of the resulting GHZ state is calculated as an average over  $\delta_1$  and  $\omega$ .

The optimal number of scattering times  $n_{\text{sc}}$  is determined by looking for the lowest infidelity in the regime where the success rate is above  $10^{-4}$ . We found the optima by scanning the GHZ fidelity and success rates over the number of scattering times, as shown in Fig. 22.

### Appendix G: Carving scheme with coherent light source

Here, we describe the calculation method for the carving scheme with coherent light. We will use the following

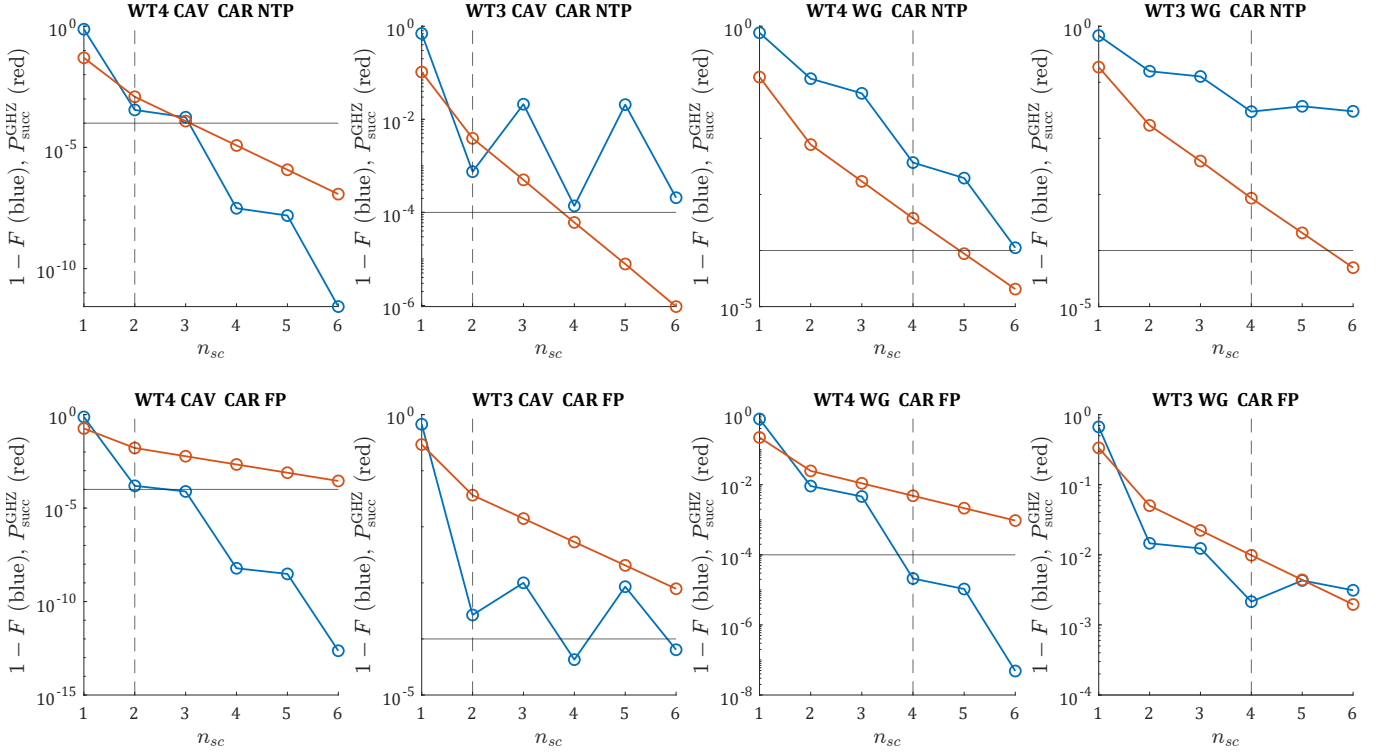


FIG. 22. The scan of fidelity and success rate over the number of scattering times in the carving scheme with a single photon source. The title in each plot denotes different architectures, entangling schemes, and parameter sets. The red curves represent the success rate, and the blue curves represent the infidelity. The horizontal solid black lines denote the minimum requirement of the success rate of  $10^{-4}$ . The vertical dashed black lines denote the selected optimum numbers of scattering times. They are also listed in the table in Fig. 9 and 10 in the main text.

properties of the coherent light. (1) A beam splitter converts a coherent light beam into two independent beams of coherent light:  $|\alpha\rangle \rightarrow \left| \frac{\alpha}{\sqrt{2}} \right\rangle_+ \left| \frac{\alpha}{\sqrt{2}} \right\rangle_-$ . (2) If there are two coherent light beams incident on both input ports of the beam splitter, the conversion of the beam splitter is:  $|\alpha\rangle |\beta\rangle \rightarrow \left| \frac{\alpha+\beta}{\sqrt{2}} \right\rangle_+ \left| \frac{\alpha-\beta}{\sqrt{2}} \right\rangle_-$ . (3) A coherent light beam after scattering from a spin-system will be split into three independent coherent light beams in the linear regime considered here (i.e. the pulse is assumed long enough that only a single photon from the beam scatters from the spin at a time):  $|\alpha\rangle \rightarrow |r\alpha\rangle |d\alpha\rangle |t\alpha\rangle$ , where  $r$ ,  $d$  and  $t$  are the reflection, dissipation, and transmission coefficients of the spin. They have the relationships  $|r|^2 + |d|^2 + |t|^2 = 1$ .

We first take the case with two spins, one at the upper route and one at the lower routes, as an example to demonstrate the calculation method and then generalize to the case with  $n_{\text{wt}}$  spins. The spins are initially in a

state  $|\psi_0\rangle = \frac{1}{\sqrt{2}}(1, 1, 1, 1)^T$ . When the coherent light beam  $|\alpha\rangle$  from the light source passes the first beam splitter, it turns into the state  $\left| \frac{\alpha}{\sqrt{2}} \right\rangle_u \left| \frac{\alpha}{\sqrt{2}} \right\rangle_d$ , where the subscripts denote the upper ("u") and lower ("d") routes. Next, when the beams have passed through the spin-systems, the state of the spins-systems and light field becomes:

$$|\psi_1^p\rangle = \frac{1}{2} \left( \begin{array}{c} \left| \frac{r_0\alpha}{\sqrt{2}} \right\rangle_u \left| \frac{d_0\alpha}{\sqrt{2}} \right\rangle_u \left| \frac{t_0\alpha}{\sqrt{2}} \right\rangle_u \left| \frac{r_0\alpha}{\sqrt{2}} \right\rangle_d \left| \frac{d_0\alpha}{\sqrt{2}} \right\rangle_d \left| \frac{t_0\alpha}{\sqrt{2}} \right\rangle_d \\ \left| \frac{r_0\alpha}{\sqrt{2}} \right\rangle_u \left| \frac{d_0\alpha}{\sqrt{2}} \right\rangle_u \left| \frac{t_0\alpha}{\sqrt{2}} \right\rangle_u \left| \frac{r_1\alpha}{\sqrt{2}} \right\rangle_d \left| \frac{d_1\alpha}{\sqrt{2}} \right\rangle_d \left| \frac{t_1\alpha}{\sqrt{2}} \right\rangle_d \\ \left| \frac{r_1\alpha}{\sqrt{2}} \right\rangle_u \left| \frac{d_1\alpha}{\sqrt{2}} \right\rangle_u \left| \frac{t_1\alpha}{\sqrt{2}} \right\rangle_u \left| \frac{r_0\alpha}{\sqrt{2}} \right\rangle_d \left| \frac{d_0\alpha}{\sqrt{2}} \right\rangle_d \left| \frac{t_0\alpha}{\sqrt{2}} \right\rangle_d \\ \left| \frac{r_1\alpha}{\sqrt{2}} \right\rangle_u \left| \frac{d_1\alpha}{\sqrt{2}} \right\rangle_u \left| \frac{t_1\alpha}{\sqrt{2}} \right\rangle_u \left| \frac{r_1\alpha}{\sqrt{2}} \right\rangle_d \left| \frac{d_1\alpha}{\sqrt{2}} \right\rangle_d \left| \frac{t_1\alpha}{\sqrt{2}} \right\rangle_d \end{array} \right) \quad (\text{G1})$$

where the subscripts "0" and "1" of the reflection, dissipation, and transmission coefficients are regarding the  $|0\rangle$  and  $|1\rangle$  states of the spin, respectively.

When the beams are interfered at the second beam splitter, the state of the spin-systems and photonic field becomes:

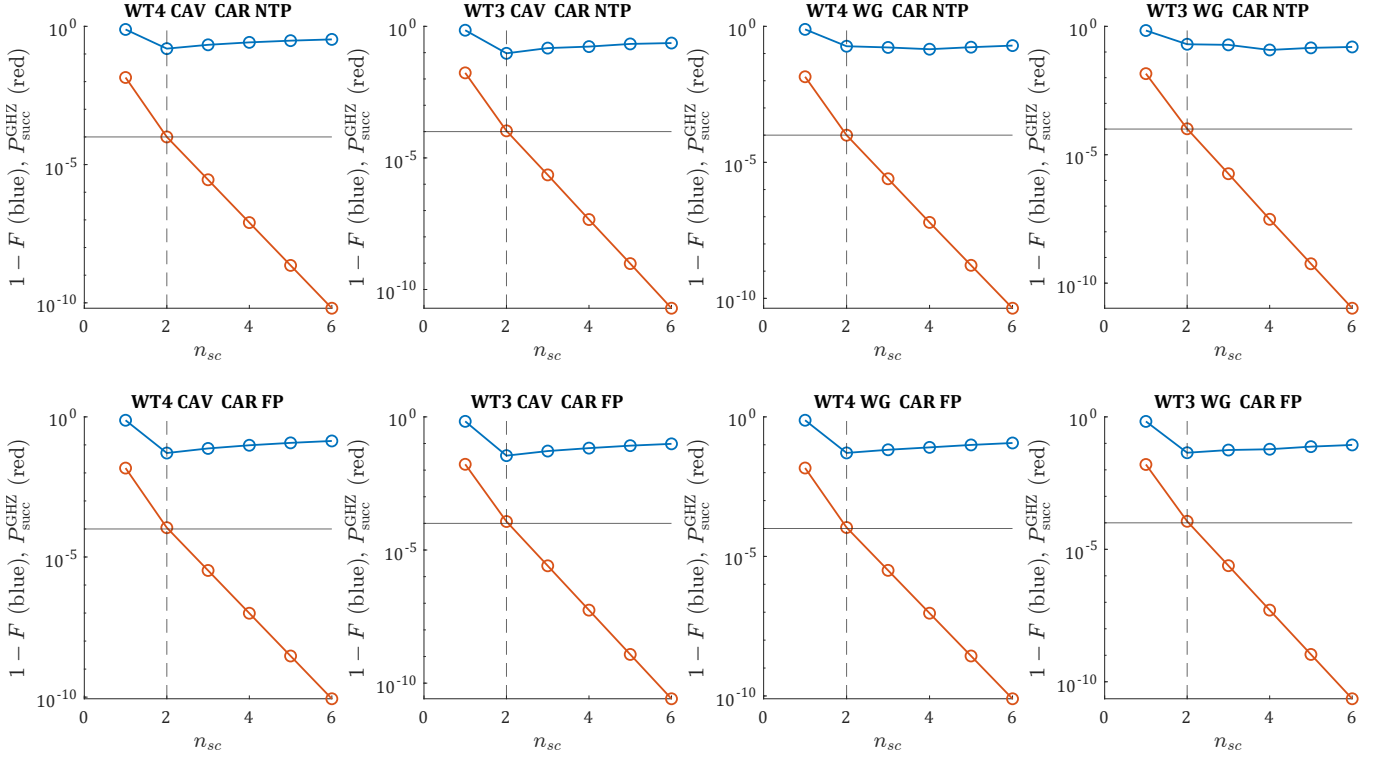


FIG. 23. The scan of fidelity and success rate over the number of scattering times in the carving scheme with a single photon source. The title in each plot denotes different architectures, entangling schemes, and parameter sets. The red curves represent the success rate, and the blue curves represent the infidelity. The horizontal solid black lines denote the minimum requirement of the success rate of  $10^{-4}$ . The vertical dashed black lines denote the selected optimum numbers of scattering times. They are also listed in the table in Fig. 9 and 10 in the main text.

$$|\psi_1^b\rangle = \frac{1}{2} \left( \begin{array}{c} \left| \frac{r_0\alpha}{\sqrt{2}} \right\rangle_u \left| \frac{d_0\alpha}{\sqrt{2}} \right\rangle_u \left| \frac{r_0\alpha}{\sqrt{2}} \right\rangle_d \left| \frac{d_0\alpha}{\sqrt{2}} \right\rangle_d \left| \frac{2t_0\alpha}{\sqrt{2}} \right\rangle_+ |0\rangle_- \\ \left| \frac{r_0\alpha}{\sqrt{2}} \right\rangle_u \left| \frac{d_0\alpha}{\sqrt{2}} \right\rangle_u \left| \frac{r_1\alpha}{\sqrt{2}} \right\rangle_d \left| \frac{d_1\alpha}{\sqrt{2}} \right\rangle_d \left| \frac{t_0+t_1}{\sqrt{2}} \alpha \right\rangle_+ \left| \frac{t_0-t_1}{\sqrt{2}} \alpha \right\rangle_- \\ \left| \frac{r_1\alpha}{\sqrt{2}} \right\rangle_u \left| \frac{d_1\alpha}{\sqrt{2}} \right\rangle_u \left| \frac{r_0\alpha}{\sqrt{2}} \right\rangle_d \left| \frac{d_0\alpha}{\sqrt{2}} \right\rangle_d \left| \frac{t_1+t_0}{\sqrt{2}} \alpha \right\rangle_+ \left| \frac{t_1-t_0}{\sqrt{2}} \alpha \right\rangle_- \\ \left| \frac{r_1\alpha}{\sqrt{2}} \right\rangle_u \left| \frac{d_1\alpha}{\sqrt{2}} \right\rangle_u \left| \frac{r_1\alpha}{\sqrt{2}} \right\rangle_d \left| \frac{d_1\alpha}{\sqrt{2}} \right\rangle_d \left| \frac{2t_1\alpha}{\sqrt{2}} \right\rangle_+ |0\rangle_- \end{array} \right) \quad (\text{G2})$$

where the subscripts "+" and "-" denote the two sides of the second beam splitter.

We now perform partial traces over the reflection and dissipation modes and project the transmission modes onto the cases where only detector  $d_+$  or  $d_-$  records a photon. One may use the following formula to accomplish the calculation: for arbitrary coherent states  $|\beta\rangle$  and  $|\gamma\rangle$ ,

$$\sum_{l=0}^{\infty} \langle l|\beta\rangle \langle \gamma|l\rangle = e^{-\frac{|\beta-\gamma|^2}{2}} e^{\frac{\beta\gamma^* - \beta^*\gamma}{2}}, \quad (\text{G3})$$

and

$$\begin{aligned} \sum_{l=1}^{\infty} \langle l|\beta\rangle \langle \gamma|l\rangle &= \sum_{l=0}^{\infty} \langle l|\beta\rangle \langle \gamma|l\rangle - \langle 0|\beta\rangle \langle \gamma|0\rangle \\ &= e^{-\frac{|\beta-\gamma|^2}{2}} e^{\frac{\beta\gamma^* - \beta^*\gamma}{2}} - e^{-\frac{|\beta|^2 + |\gamma|^2}{2}}. \end{aligned} \quad (\text{G4})$$

where  $|l\rangle$  are the Fock states.

After one traces out the reflection and dissipation modes and projects the transmission modes on the corresponding bases, one gets the density matrix of the spin systems after the first round of light scattering. One can then apply NOT gates on it and calculate the effect of another round of photon scattering on top of this similar to the procedure for a perfect single photon source described above.

Based on the calculation above, one can see that the overall effect of photon scattering is that it multiplies each entry of the spin density matrix with a certain coefficient. Therefore, one can derive an iteration relationship

of the density matrix of the spin as

$$\rho_{n_{sc}} = \begin{cases} \mathbf{T}_{\text{coh}} \odot \rho_{n_{sc}-1}, & n_{sc} = 1 \\ \mathbf{T}_{\text{coh}} \odot (O_{\text{not}} \rho_{n_{sc}-1} O_{\text{not}}), & n_{sc} \geq 2 \end{cases} \quad (\text{G5})$$

where  $\rho_{n_{sc}}$  is the density matrix after scattering  $n_{sc}$ th coherent states, and  $O_{\text{not}}$  is the operation of NOT gates on every spin. The coefficient matrix  $\mathbf{T}_{\text{coh}}$  is defined as

$$\mathbf{T}_{\text{coh}} = \begin{cases} \left( \bigodot_{j=1}^{n_{\text{wt}}} S_j^{\text{R}} \odot S_j^{\text{D}} \right) \odot S^+, & \text{detection on "+" side} \\ \left( \bigodot_{j=1}^{n_{\text{wt}}} S_j^{\text{R}} \odot S_j^{\text{D}} \right) \odot S^-, & \text{detection on "-" side} \end{cases} \quad (\text{G6})$$

where  $n_{\text{wt}}$  is the total number of spins,

$$S_j^{\text{R}} = \sum_{l=0}^{\infty} ([\langle l |] \odot \mathbf{R}_j) \left( \mathbf{R}_j^\dagger \odot [|\langle l \rangle]^{\text{T}} \right), \quad (\text{G7})$$

$$S_j^{\text{D}} = \sum_{l=0}^{\infty} ([\langle l |] \odot \mathbf{D}_j) \left( \mathbf{D}_j^\dagger \odot [|\langle l \rangle]^{\text{T}} \right), \quad (\text{G8})$$

$$S^+ = \sum_{l=1}^{\infty} ([\langle l |] \odot \mathbf{T}_+) \left( \mathbf{T}_+^\dagger \odot [|\langle l \rangle]^{\text{T}} \right) \odot ([\langle 0 |] \odot \mathbf{T}_-) \left( \mathbf{T}_-^\dagger \odot [|\langle 0 \rangle]^{\text{T}} \right), \quad (\text{G9})$$

and

$$S^- = ([\langle 0 |] \odot \mathbf{T}_+) \left( \mathbf{T}_+^\dagger \odot [|\langle 0 \rangle]^{\text{T}} \right) \odot \sum_{l=1}^{\infty} ([\langle l |] \odot \mathbf{T}_-) \left( \mathbf{T}_-^\dagger \odot [|\langle l \rangle]^{\text{T}} \right), \quad (\text{G10})$$

where  $[\langle l |]$  is a column vector whose elements are all  $\langle l |$ . And,  $\mathbf{R}_j$ ,  $\mathbf{D}_j$ ,  $\mathbf{T}_+$ , and  $\mathbf{T}_-$  are vectors whose entries are wavefunctions of the reflection, dissipation, and transmission coherent light beams. Similar to Eqn. G2, they form a relationship

$$|\psi_1^{\text{b}}\rangle = \left( \bigodot_{j=1}^{n_{\text{wt}}} \mathbf{R}_j \odot \mathbf{D}_j \right) \odot \mathbf{T}_+ \odot \mathbf{T}_- \odot |\psi_0\rangle. \quad (\text{G11})$$

Their entries are defined as

$$\begin{aligned} \mathbf{R}_j[k] &= |\bar{\alpha}_j^{\text{r}}[k]\rangle \\ \mathbf{D}_j[k] &= |\bar{\alpha}_j^{\text{d}}[k]\rangle \\ \mathbf{T}_+[k] &= |\bar{\alpha}_{\text{t}+}[k]\rangle \\ \mathbf{T}_-[k] &= |\bar{\alpha}_{\text{t}-}[k]\rangle \end{aligned} \quad (\text{G12})$$

where  $\bar{\alpha}_j^{\text{r}}$  is defined as

$$\bar{\alpha}_j^{\text{r}} = \begin{cases} \frac{\alpha}{\sqrt{2}} \begin{pmatrix} t_0 \\ t_1 \end{pmatrix}^{\otimes(j-1)} \otimes \begin{pmatrix} r_0 \\ r_1 \end{pmatrix} \otimes \begin{pmatrix} 1 \\ 1 \end{pmatrix}^{\otimes(n_{\text{wt}}-j)}, & j \leq n_{\text{u}} \\ \frac{\alpha}{\sqrt{2}} \begin{pmatrix} 1 \\ 1 \end{pmatrix}^{\otimes(n_{\text{u}})} \otimes \begin{pmatrix} t_0 \\ t_1 \end{pmatrix}^{\otimes(j-n_{\text{u}}-1)} \otimes \begin{pmatrix} r_0 \\ r_1 \end{pmatrix} \otimes \begin{pmatrix} 1 \\ 1 \end{pmatrix}^{\otimes(n_{\text{wt}}-j)}, & j \geq n_{\text{u}} \end{cases}. \quad (\text{G13})$$

The vector  $\bar{\alpha}_j^{\text{d}}$  follows a similar definition as  $\bar{\alpha}_j^{\text{r}}$ , which can be derived by replacing  $r_0$  and  $r_1$  with  $d_0$  and  $d_1$ . And,  $\bar{\alpha}_{\text{t}\pm} = \frac{1}{\sqrt{2}} (\bar{\alpha}_{\text{u}} \pm \bar{\alpha}_{\text{d}})$  with

$$\bar{\alpha}_{\text{u}} = \frac{\alpha}{\sqrt{2}} \begin{pmatrix} t_0 \\ t_1 \end{pmatrix}^{\otimes n_{\text{u}}} \otimes \begin{pmatrix} 1 \\ 1 \end{pmatrix}^{\otimes n_{\text{d}}} \quad (\text{G14})$$

$$\bar{\alpha}_{\text{d}} = \frac{\alpha}{\sqrt{2}} \begin{pmatrix} 1 \\ 1 \end{pmatrix}^{\otimes n_{\text{u}}} \otimes \begin{pmatrix} t_0 \\ t_1 \end{pmatrix}^{\otimes n_{\text{d}}}, \quad (\text{G15})$$

with  $n_{\text{u}}$  and  $n_{\text{d}}$  the number of spins in the upper and lower optical routes, respectively. By now, we get the unnormalized density matrix of the spin after  $n_{\text{sc}}$  rounds of light scattering. The trace of the density matrix gives the success rate for generating the GHZ state.

The optimum values of  $\delta_1$  and  $\omega$  are the same as in the carving scheme with a single-photon source as discussed

in App. F. However, the optimal values of  $\alpha$  and the number of scattering times  $n_{\text{sc}}$  must be determined.

On the one hand, having more light-scattering rounds can potentially increase the GHZ fidelity, as in the carving scheme with a deterministic single-photon source. On the other hand, it also means more reflection and dissipation modes that will leak the quantum information of the system into the environment. We found that for all the cases in the carving scheme with coherent light, the optimum number of light-scattering rounds is  $n_{\text{sc}} = 2$  because the fidelity gain from more scattering rounds doesn't outweigh the information leakage.

Regarding the determination of  $\alpha$ , the larger the  $\alpha$ , the larger the success rate, but the lower the fidelity. For small  $\alpha$ , the coherent light resembles a probabilistic single-photon source. Hence, the fidelity of this scheme

will approach the scheme with a deterministic single-photon source. However, the success rate will be much lower than it. On the other hand, when  $\alpha$  is large, the success rate will approach the scheme with a deterministic single-photon source, but the fidelity will decrease. To get the maximum fidelity, we set the  $\alpha$ , letting the success rate take the minimum requirement value of  $10^{-4}$  at  $n_{sc} = 2$  as shown in Fig. 23. However, the fidelities in that circumstance are still too low to realize modular quantum computing with surface code. Hence, the carving scheme with a coherent light source is not promising.

### Appendix H: Example: Diamond defect center implementation

To demonstrate a particular physical implementation of our formalism, we give an example of diamond defect center-based hardware. We define a coherence times parameter set (called Set-D) inspired by nitrogen-vacancy (NV) centers in diamond [30, 31, 49, 69, 71, 72]. NV centers may, however, not be suited for the direct entangling schemes due to the difficulty of coupling these defect centers to nanophotonic cavities and waveguides. Nonetheless, we anticipate that other defect centers, such as SnV or SiV, where strong coupling to nanophotonic cavities and waveguides has been experimentally demonstrated, can achieve similar coherence and operational times.

Parameter Sets	Set - 1	Set - 2	Set - 3	Set - mix	Set - D
$T_{\text{link}}^{\text{dec}}$	$10^4$	$10^5$	$10^6$	$10^4$	$T_{1,\text{link}}^m = 0.3 \text{ s}$ $T_{2,\text{link}}^m = 0.075 \text{ s}$
$T_{\text{idle}}^{\text{dec}}$	$10^5$	$10^5$	$10^6$	$10^6$	$T_{1,\text{idle}}^c = 300 \text{ s}$ $T_{2,\text{idle}}^c = 1 \text{ s}$ $T_{1,\text{idle}}^m = 300 \text{ s}$ $T_{2,\text{idle}}^m = 10 \text{ s}$
Operation times					
$t_{\text{link}}$	1	1	1	1	$6 \times 10^{-6} \text{ s}$
$t_{\text{meas}}$	1	1	1	1	$4 \times 10^{-6} \text{ s}$
$t_p^{\phi}$	0.01	0.01	0.01	0.01	$t_{X,Y}^{\phi} = 0.14 \times 10^{-6} \text{ s}$ $t_{Z,H}^{\phi} = 10^{-6} \text{ s}$
$t_p^m$	100	100	100	100	$t_{X,Y}^m = 10^{-3} \text{ s}$ $t_{Z,H}^m = 0.5 \times 10^{-3} \text{ s}$
$t_{CZ}, t_{CX}, t_{CIY}$	100	100	100	100	$0.5 \times 10^{-3} \text{ s}$
$t_{\text{SWAP}}$	300	300	300	300	$1.5 \times 10^{-3} \text{ s}$

FIG. 24. Table describing the coherence and operation times, including two additional parameter sets, Set-mix and Set-D. All values except Set-D are expressed w.r.t. absolute value of  $t_{\text{link}} = 10^{-5} \text{ s}$ , which is assumed to take one unit of time. Set-D is a special set with absolute values in seconds.

The coherence parameters' values for Set-D are inspired by Ref. [71] and shown in Fig. 24. We consider separate  $T_1$  and  $T_2$  times for the generalized amplitude and phase damping channels inspired by the experiments. The values indicate a relatively strong dephasing noise

(Z-biased). Set-D is also a special set for the inclusion of dynamical decoupling (DD) methods that reduce noise during gate pulse sequences [88]. In this model, gate pulses can only be applied during the focusing point between two DD pulses. This refocusing time is expressed as  $t_{\text{DD}} = t_{\text{pulse}} + 2n_{\text{DD}}t_{\text{link}}$ , where  $t_{\text{pulse}}$  is the time duration of a  $\pi$ -pulse for DD sequence. For a given value of  $t_{\text{pulse}}$  inspired from the experiments,  $n_{\text{DD}}$  was optimized in Ref. [25]. We also use the same values of  $t_{\text{pulse}} = 10^{-3} \text{ s}$  and  $n_{\text{DD}} = 18$  for Set-D. These parameters are not used for other sets in the simulations.

Another quantity for more insight into the distributed systems is link efficiency  $\eta^*$ , as also explored in Ref. [25] in the context of NV centers using an EM scheme. We can express the entanglement generation efficiency (EGE) for EM or direct GHZ generation schemes as:

$$\eta^* = \frac{2P_{\text{succ}}^{\text{link/GHZ}}}{t_{\text{link/GHZ}} \left( (T_{1,\text{link/GHZ}}^{\text{dec}})^{-1} + (T_{2,\text{link/GHZ}}^{\text{dec}})^{-1} \right)} \quad (\text{H1})$$

The entanglement generation efficiency captures the average number of Bell pairs or GHZ states that can be generated within the coherence times of the memory qubits. We also calculate the link (entanglement generation) efficiency for all schemes in App. I via tables in Fig. 28 and Fig. 29.

### Appendix I: Threshold simulation details

In this appendix, we provide details on the numerical calculations of the distributed surface code thresholds. We also introduce two additional parameter sets for the coherence and operational times: Set-mix and Set-D. Set-mix is a set composed of  $T_{\text{link}}^{\text{dec}}$  from Set-1 and  $T_{\text{idle}}^{\text{dec}}$  from Set-3. The motivation is to analyze the performance of technologies that exhibit excellent quantum memory capabilities with long-lasting  $T_{\text{idle}}^{\text{dec}}$  times. Set-D is inspired by nitrogen-vacancy (NV) center implementation of distributed surface code, explored in Ref. [25]. See App. H for more details on the physical model based on defect centers in diamond. Fig. 24 presents a summary of all the five parameter sets together. For Set-D, we use the absolute values of the parameters and not relative numbers w.r.t.  $t_{\text{link}}$  times. We use different  $T_{1/2,\text{idle/link}}^{\text{dec}}$  times as shown, inspired via the experiments with dynamical decoupling (DD) incorporated gates.

#### 1. Cut-off time optimization

As described in the main text, the cut-off time  $t_{\text{cut}}$  caps the maximum time allowed for GHZ generation for any scheme during the stabilizer measurement. Assuming  $t_{\text{cut}}^{100\%}$  is the average time allowed for successful GHZ for a certain number of attempts, we can define some  $t_{\text{cut}}^{x\%}$  where we get a GHZ success within  $x\%$  attempts for entanglement generation using any scheme.  $t_{\text{cut}}^{100\%}$  is

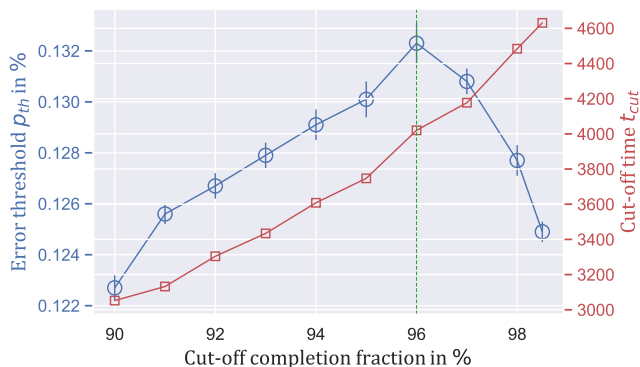


FIG. 25. Distributed surface code threshold  $p_{\text{th}}$  (blue) and cut-off time  $t_{\text{cut}}$  (red) w.r.t. GHZ cut-off completion fraction  $x$ . For each value of  $x$ , we find  $t_{\text{cut}}^{x\%}$ , which gives a certain threshold. A binary search for the highest value of  $p_{\text{th}}$  results in an optimal value of  $x$ . The optimal value (highest) is shown in green. This plot was created for WT4 EM Set-3 FP.

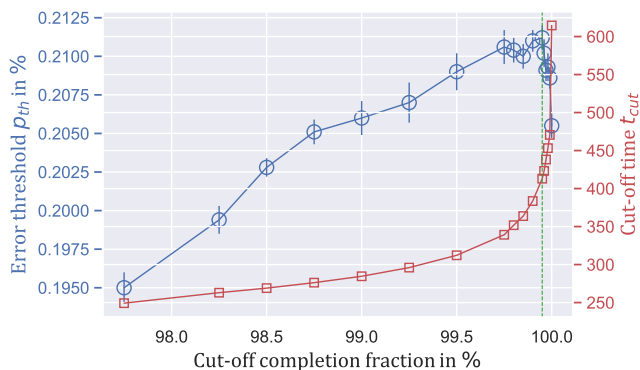


FIG. 26. Distributed surface code threshold  $p_{\text{th}}$  (blue) and cut-off time  $t_{\text{cut}}$  (red) w.r.t. GHZ cut-off completion fraction  $x$  for WT4 RFL Set-mix NTP. Read Fig. 25's caption for details.

computed in prior in our simulations. Then, we start with a trial value of  $x$  (typically around 98% – 99% for direct schemes or lower for EM schemes) to estimate logical error rates ( $p_L$ ) in a wide spectrum of physical error rates  $p$ . We sweep  $x$  in our noisy stabilizer simulator and deduce the  $t_{\text{cut}}^{x\%}$  value. For each fixed value of  $t_{\text{cut}}^{x\%}$ , we perform the threshold simulations to get the logical error rates and estimate the threshold for the code. If the logical error rates are low enough (typically less than 0.2), we search ahead for a threshold. If the logical error rates are greater than 0.90, we abandon the search as there is a negligible chance of threshold within that regime, which we verified numerically.

$t_{\text{cut}}^{x\%}$  increases exponentially as  $x$  increases (see Fig. 25 and Fig. 26). Starting from a low value of  $x$ , first, the code threshold  $p_{\text{th}}$  increases with  $x$ , because more  $t_{\text{cut}}$  allows for more error syndrome collection. However, if we keep increasing  $x$ , the code threshold starts to saturate to a maximum where more  $t_{\text{cut}}$  does not assist in more

syndrome data collection but starts contributing to more noise via decoherence. If we increase  $x$  further, we see a rapid fall in the threshold near very high values of  $x$ . We perform a binary search over the variable  $x$  to find the highest value of  $p_{\text{th}}$ , including the error bars. Using the respective entanglement generation scheme, we report the highest value as the code threshold  $p_{\text{th}}$  for that architecture.

## 2. Threshold estimation

Now, we describe the threshold estimation in detail. A trial (guessed) value of  $t_{\text{cut}}^{x\%}$  is chosen. Using a superoperator table for a certain input physical error probability  $p$ , we calculate the logical error probability  $p_L$  (or logical success probability/rate  $1 - p_L$ ). A wide range of input  $p$  values is considered such that a threshold lies within this range by numerically observing the behavior of  $p_L$  with increasing lattice sizes (6,8,10,12). When a threshold exists, we narrow the search to a small range of  $p$  values for the fitting procedure. We use the fitting function of the form [89]:

$$p_L = A + B\gamma + C\gamma^2 \quad (11)$$

where  $\gamma = (p - p_{\text{th}})L^{1/\nu_0}$ , with  $L$  as different lattice sizes for different curves. The fitting parameters  $A, B, C, p_{\text{th}}, \nu_0$  are found from numerical optimization using the least-squares method. This is discussed in great detail in Ref. [25].

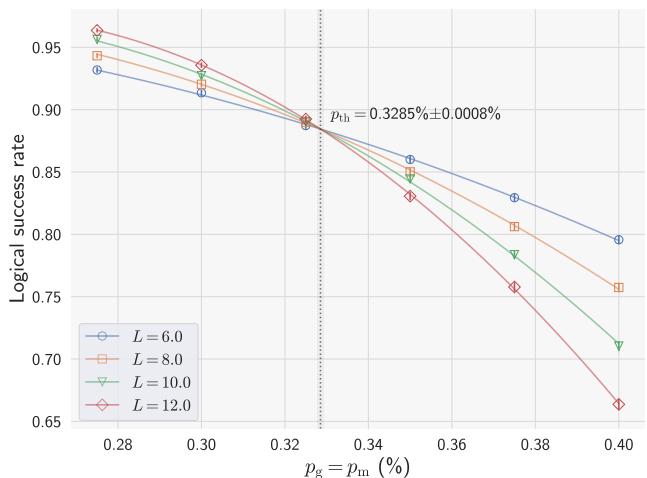


FIG. 27. Example threshold plot for WT4 RFL (Set-3) NTP. The plot shows the logical success rates  $1 - p_L$  against physical error rates  $p = p_g = p_m$  for different even-valued distances for the distributed surface code. The fitting function reveals the code threshold within some error bar.

Here, we show an example of threshold estimation in 27 where we perform the fitting procedure for logical success curves for various even-sized code distances.

### 3. Detailed threshold simulation data

Finally, we provide all the simulation data for all the architectures and schemes in combination with all the coherence parameter sets, including the recently introduced Set-mix and Set-D. This is presented via full-page tables in Fig. 28 (WT4) and Fig. 29 (WT3). Each block of rows describes the simulation results for a particular coherence parameter set. The columns describe different combinations of architecture layout, scheme, and NTP/FP parameters.

The first row within each block describes the success probability  $P_{\text{succ}}^{\text{link/GHZ}}$ , which has been introduced earlier. While previously we reported thresholds found using the Union-Find (UF) decoder [75] by optimizing the binary search for threshold values, we report a much higher threshold ( $p_{\text{th}}$  at MWPM) in this data using the minimum-weight perfect matching (MWPM) decoder [90]. The UF threshold value is listed next, also the threshold value we reported in the main text. This was preferred because the UF decoder is fast with linear time complexity in the number of qubits. We find the logical success rate ( $1 - p_L$ ) at the threshold value using the MWPM decoder for more insight into the threshold performance. The optimal GHZ cut-off completion fraction ( $x\%$ ) is also listed. This is the completion fraction at which the peak performance of the architecture was found using the respective scheme. The completion fraction is relatively less for EM schemes as these require fusion operations that take longer for GHZ generation. The decoherence vs. syndrome data rate trade-off is satisfied much earlier for EM schemes during QEC cycles. This can also be seen in Fig. 25 for the EM scheme and Fig. 26 for the RFL scheme. After that, we report the entanglement generation efficiency ( $\eta^*$ , described in Eqn. H1). The next number is the cut-off time  $t_{\text{cut}}$  at the optimal GHZ cut-off completion rate. The cut-off time is crucial to define the logical clock speed of the quantum computer via the duration of the QEC cycle. It is decided by  $t_{\text{cut}}$  or the two-qubit gate times  $t_P^2$  (on the memory qubits), whichever is higher. GHZ fidelity at the threshold value using the UF decoder is also reported, which indicates the quality of the entanglement generation scheme used. The fidelity is calculated for only the direct schemes where the average fidelity was calculated using the average density matrix of the output GHZ state from the scheme. For the EM scheme, this was not possible due to the different protocols used for fusion. However, we can calculate the output Bell pair fidelity for any physical error rate using Eqn. D18 and Eqn. D22, as the case may be. Finally, we report the stabilizer fidelity (at the UF threshold) for the entire stabilizer circuit protocol using any scheme considering the noisy two-qubit gates on the memory and noisy measurements. An improvement in two-qubit gate times or fidelity will drastically improve the stabilizer fidelity.

Scheme	EM		REL		CAV CAR SGL		WG CAR SGL		RFL		CAV CAR SGL		WG CAR SGL	
	WT-4	NTP	WT-4	NTP	WT-4	NTP	WT-4	NTP	WT-4	FP	WT-4	FP	WT-4	FP
Set-1 $P_{\text{succ}}^{\text{GHZ}}$	0.0001		0.0147		0.0013		0.0003		0.3782		0.0164		0.0048	
Set-1 ( $P_{\text{th}}$ in %) using MWPM	NT		0.1907 % $\pm$ 0.0018 %		NT		NT		0.3683 % $\pm$ 0.0012 %		0.2689 % $\pm$ 0.0011 %		0.0048	
Set-1 ( $P_{\text{th}}$ in %) using UF	NT		0.1707 % $\pm$ 0.0013 %		NT		NT		0.3443 % $\pm$ 0.0010 %		0.2387 % $\pm$ 0.0015 %		NT	
Set-1 (LSR at MWPM $P_{\text{th}}$ )	NT		0.8552 $\pm$ 0.0040		NT		NT		0.8698 $\pm$ 0.0026		0.8632 $\pm$ 0.0021		NT	
Set-1 (optimal $t_{\text{cut}}$ completion in %)	NT		98.00 %		NT		NT		99.82 %		98.56 %		NT	
Set-1 EGE ( $t^*$ )	NT		147		NT		NT		3782		164		NT	
Set-1 ( $t_{\text{cut}}$ )	NT		258.81		NT		NT		108.81		250.41		NT	
Set-1 (GHZ fidelity at UF $P_{\text{th}}$ )	NT		99.37 %		NT		NT		99.00		99.44 %		NT	
Set-1 (Stabilizer fidelity at UF $P_{\text{th}}$ )	NT		93.51 %		NT		NT		94.13		93.42 %		NT	
Set-2 $P_{\text{succ}}^{\text{GHZ}}$	0.0001		0.0147		0.0013		0.0003		0.3782		0.0164		0.0048	
Set-2 ( $P_{\text{th}}$ in %) using MWPM	NT		0.3040 % $\pm$ 0.0013 %		NT		NT		0.3730 % $\pm$ 0.0010 %		0.3813 % $\pm$ 0.0013 %		0.2431 % $\pm$ 0.0010 %	
Set-2 ( $P_{\text{th}}$ in %) using UF	NT		0.2807 % $\pm$ 0.0008 %		NT		NT		0.3488 % $\pm$ 0.0008 %		0.3450 % $\pm$ 0.0011 %		0.2158 % $\pm$ 0.0011 %	
Set-2 (LSR at MWPM $P_{\text{th}}$ )	NT		0.8663 $\pm$ 0.0029		NT		NT		0.8703 $\pm$ 0.0021		0.8682 $\pm$ 0.0024		0.8665 $\pm$ 0.0020	
Set-2 (optimal $t_{\text{cut}}$ completion in %)	NT		98.50 %		NT		NT		99.82 %		99.75 %		98.26 %	
Set-2 EGE ( $t^*$ )	NT		1470		NT		NT		37820		1640		480	
Set-2 ( $t_{\text{cut}}$ )	NT		269.01		NT		NT		108.81		317.01		603.21	
Set-2 (GHZ fidelity at UF $P_{\text{th}}$ )	NT		99.07 %		NT		NT		98.99 %		99.22 %		99.25 %	
Set-2 (Stabilizer fidelity at UF $P_{\text{th}}$ )	NT		93.18 %		NT		NT		94.10 %		93.83 %		92.95 %	
Set-3 $P_{\text{succ}}^{\text{GHZ}}$	0.0001		0.0147		0.0013		0.0003		0.3782		0.0164		0.0048	
Set-3 ( $P_{\text{th}}$ in %) using MWPM	NT		0.3538 % $\pm$ 0.0010 %		0.3626 % $\pm$ 0.0022 %		0.0226 % $\pm$ 0.0012 %		0.1449 % $\pm$ 0.0008 %		0.4462 % $\pm$ 0.0022 %		0.3885 % $\pm$ 0.0010 %	
Set-3 ( $P_{\text{th}}$ in %) using UF	NT		0.3285 % $\pm$ 0.0008 %		0.3298 % $\pm$ 0.0011 %		0.0180 % $\pm$ 0.0011 %		0.1323 % $\pm$ 0.0008 %		0.4072 % $\pm$ 0.0010 %		0.3541 % $\pm$ 0.0007 %	
Set-3 (LSR at MWPM $P_{\text{th}}$ )	NT		0.8656 $\pm$ 0.0022		0.8750 $\pm$ 0.0038		0.8327 $\pm$ 0.0025		0.8656 $\pm$ 0.0032		0.8806 $\pm$ 0.0037		0.8938 $\pm$ 0.0018	
Set-3 (optimal $t_{\text{cut}}$ completion in %)	NT		99.93 %		98.10 %		96.03 %		100 %		99.90 %		99.25 %	
Set-3 EGE ( $t^*$ )	NT		14700		1300		300		378200		16400		4800	
Set-3 ( $t_{\text{cut}}$ )	NT		398.61		1901.01		5339.01		114.81		350.01		704.61	
Set-3 (GHZ fidelity at UF $P_{\text{th}}$ )	NT		98.93 %		99.21 %		98.86 %		98.97 %		99.09 %		98.82 %	
Set-3 (Stabilizer fidelity at UF $P_{\text{th}}$ )	NT		94.23 %		92.52 %		92.57 %		94.21 %		93.64 %		92.93 %	
Set-mix $P_{\text{succ}}^{\text{GHZ}}$	0.0001		0.0147		0.0013		0.0003		0.3782		0.0164		0.0048	
Set-mix ( $P_{\text{th}}$ in %) using MWPM	NT		0.2340 % $\pm$ 0.0013 %		NT		NT		0.3704 % $\pm$ 0.0013 %		0.3146 % $\pm$ 0.0013 %		NT	
Set-mix ( $P_{\text{th}}$ in %) using UF	NT		0.2112 % $\pm$ 0.0008 %		NT		NT		0.3455 % $\pm$ 0.0010 %		0.2820 % $\pm$ 0.0013 %		NT	
Set-mix (LSR at MWPM $P_{\text{th}}$ )	NT		0.8453 $\pm$ 0.0032		NT		NT		0.8707 $\pm$ 0.0028		0.8612 $\pm$ 0.0025		NT	
Set-mix (optimal $t_{\text{cut}}$ completion in %)	NT		99.95 %		NT		NT		99.82 %		99.80 %		NT	
Set-mix EGE ( $t^*$ )	NT		147		NT		NT		3782		164		NT	
Set-mix ( $t_{\text{cut}}$ )	NT		413.01		NT		NT		108.81		322.41		NT	
Set-mix (GHZ fidelity at UF $P_{\text{th}}$ )	NT		99.25 %		NT		NT		98.99 %		99.35 %		NT	
Set-mix (Stabilizer fidelity at UF $P_{\text{th}}$ )	NT		94.89 %		NT		NT		94.11 %		94.32 %		NT	
Set-D $P_{\text{succ}}^{\text{GHZ}}$	0.0001		0.0147		0.0013		0.0003		0.3782		0.0164		0.0048	
Set-D ( $P_{\text{th}}$ in %) using MWPM	NT		0.2626 % $\pm$ 0.0015 %		NT		NT		0.3740 % $\pm$ 0.0012 %		0.3483 % $\pm$ 0.0010 %		0.0556 % $\pm$ 0.0026 %	
Set-D ( $P_{\text{th}}$ in %) using UF	NT		0.2411 % $\pm$ 0.0008 %		NT		NT		0.3484 % $\pm$ 0.0005 %		0.3144 % $\pm$ 0.0014 %		0.0380 % $\pm$ 0.0024 %	
Set-D (LSR at MWPM $P_{\text{th}}$ )	NT		0.8716 $\pm$ 0.0030		NT		NT		0.8687 $\pm$ 0.0026		0.8788 $\pm$ 0.0016		0.8878 $\pm$ 0.0039	
Set-D (optimal $t_{\text{cut}}$ completion in %)	NT		99.23 %		NT		NT		100 %		99.86 %		98.00 %	
Set-D EGE ( $t^*$ )	NT		294		NT		NT		7564		328		96	
Set-D ( $t_{\text{cut}}$ in s)	NT		0.0114481		NT		NT		0.0006421		0.0138801		0.0284721	
Set-D (GHZ fidelity at UF $P_{\text{th}}$ )	NT		99.18 %		NT		NT		98.98 %		99.29 %		99.82 %	
Set-D (Stabilizer fidelity at UF $P_{\text{th}}$ )	NT		94.14 %		NT		NT		94.25 %		94.19 %		94.83 %	

FIG. 28. Weight-4 full threshold simulations data. We give code thresholds for each architecture and scheme using two decoders, success probabilities, entanglement generation efficiency, cut-off times, GHZ, and stabilizer fidelity. NT denotes no threshold.

Scheme	EM		RFL		CAV CAR SGL		WG CAR SGL		EM		RFL		CAV CAR SGL		WG CAR SGL	
	WT-3	NTP	WT-3	NTP	WT-3	NTP	WT-3	NTP	WT-3	FP	WT-3	FP	WT-3	FP	WT-3	FP
Set-1 $P_{\text{succ}}^{\text{link}/\text{GHZ}}$	0.0001		0.0423		0.0041		0.0009		0.1		0.4823		0.0366		0.0098	
Set-1 ( $p_{\text{th}}$ in %) using MWPM	NT		0.1841 % $\pm$ 0.0013 %		NT		NT		NT		0.2906 % $\pm$ 0.0010 %		0.1935 % $\pm$ 0.0012 %		NT	
Set-1 ( $p_{\text{th}}$ in %) using UF	NT		0.1717 % $\pm$ 0.0011 %		NT		NT		NT		0.2784 % $\pm$ 0.0009 %		0.1787 % $\pm$ 0.0007 %		NT	
Set-1 (LSR at MWPM $p_{\text{th}}$ )	NT		0.8174 $\pm$ 0.0013		NT		NT		NT		0.8305 $\pm$ 0.0024		0.8158 $\pm$ 0.0029		NT	
Set-1 (optimal $t_{\text{cut}}$ completion in %)	NT		99.25 %		NT		NT		NT		100 %		99.25 %		NT	
Set-1 EGE ( $t^*$ )	NT		423		NT		NT		NT		4823		366		NT	
Set-1 ( $t_{\text{cut}}$ )	NT		268.81		NT		NT		NT		211.21		279.61		NT	
Set-1 (GHZ fidelity at UF $p_{\text{th}}$ )	NT		99.53 %		NT		NT		NT		99.39 %		99.56 %		NT	
Set-1 (Stabilizer fidelity at UF $p_{\text{th}}$ )	NT		95.51 %		NT		NT		NT		95.95 %		95.80 %		NT	
Set-2 $P_{\text{succ}}^{\text{link}/\text{GHZ}}$	0.0001		0.0423		0.0041		0.0009		0.1		0.4823		0.0366		0.0098	
Set-2 ( $p_{\text{th}}$ in %) using MWPM	NT		0.2453 % $\pm$ 0.0014 %		0.0309 % $\pm$ 0.0011 %		NT		NT		0.2954 % $\pm$ 0.0012 %		0.2717 % $\pm$ 0.0012 %		0.1701 % $\pm$ 0.0021 %	
Set-2 ( $p_{\text{th}}$ in %) using UF	NT		0.2353 % $\pm$ 0.0010 %		0.0167 % $\pm$ 0.0010 %		NT		NT		0.2849 % $\pm$ 0.0010 %		0.2603 % $\pm$ 0.0009 %		0.1522 % $\pm$ 0.0020 %	
Set-2 (LSR at MWPM $p_{\text{th}}$ )	NT		0.8355 $\pm$ 0.0033		0.8256 $\pm$ 0.0026		NT		NT		0.8312 $\pm$ 0.0028		0.8349 $\pm$ 0.0028		0.8396 $\pm$ 0.0045	
Set-2 (optimal $t_{\text{cut}}$ completion in %)	NT		98.57 %		93.00 %		NT		NT		100 %		99.012 %		97.518 %	
Set-2 EGE ( $t^*$ )	NT		4230		410		NT		NT		48230		3660		980	
Set-2 ( $t_{\text{cut}}$ )	NT		260.41		583.21		NT		NT		211.21		275.41		421.21	
Set-2 (GHZ fidelity at UF $p_{\text{th}}$ )	NT		99.41 %		99.84 %		NT		NT		99.38 %		99.39 %		99.38 %	
Set-2 (Stabilizer fidelity at UF $p_{\text{th}}$ )	NT		94.88 %		91.11 %		NT		NT		95.92 %		95.01 %		93.96 %	
Set-3 $P_{\text{succ}}^{\text{link}/\text{GHZ}}$	0.0001		0.0423		0.0041		0.0009		0.1		0.4823		0.0366		0.0098	
Set-3 ( $p_{\text{th}}$ in %) using MWPM	NT		0.3412 % $\pm$ 0.0011 %		0.3132 % $\pm$ 0.0013 %		NT		0.1024 % $\pm$ 0.0008 %		0.3624 % $\pm$ 0.0008 %		0.3775 % $\pm$ 0.0010 %		0.3613 % $\pm$ 0.0008 %	
Set-3 ( $p_{\text{th}}$ in %) using UF	NT		0.3350 % $\pm$ 0.0010 %		0.3062 % $\pm$ 0.0009 %		NT		0.0928 % $\pm$ 0.0008 %		0.3521 % $\pm$ 0.0010 %		0.3678 % $\pm$ 0.0007 %		0.3441 % $\pm$ 0.0007 %	
Set-3 (LSR at MWPM $p_{\text{th}}$ )	NT		0.8486 $\pm$ 0.0022		0.8519 $\pm$ 0.0027		NT		0.8292 $\pm$ 0.0030		0.8451 $\pm$ 0.0018		0.8528 $\pm$ 0.0020		0.8683 $\pm$ 0.0015	
Set-3 (optimal $t_{\text{cut}}$ completion in %)	NT		99.80 %		99.00 %		NT		97 %		100 %		99.90 %		99.25 %	
Set-3 EGE ( $t^*$ )	NT		42300		4100		NT		100000		482300		36600		9800	
Set-3 ( $t_{\text{cut}}$ )	NT		288.61		852.61		NT		4042.16		211.21		315.01		492.01	
Set-3 (GHZ fidelity at UF $p_{\text{th}}$ )	NT		99.21 %		99.18 %		NT		-		99.24 %		99.16 %		98.89 %	
Set-3 (Stabilizer fidelity at UF $p_{\text{th}}$ )	NT		95.29 %		94.56 %		NT		93.70 %		95.39 %		94.99 %		93.93 %	
Set-mix $P_{\text{succ}}^{\text{link}/\text{GHZ}}$	0.0001		0.0423		0.0041		0.0009		0.1		0.4823		0.0366		0.0098	
Set-mix ( $p_{\text{th}}$ in %) using MWPM	NT		0.2739 % $\pm$ 0.0009 %		NT		NT		NT		0.3534 % $\pm$ 0.0009 %		0.2923 % $\pm$ 0.0009 %		0.0350 % $\pm$ 0.0012 %	
Set-mix ( $p_{\text{th}}$ in %) using UF	NT		0.2629 % $\pm$ 0.0006 %		NT		NT		NT		0.3457 % $\pm$ 0.0010 %		0.2806 % $\pm$ 0.0009 %		0.0132 % $\pm$ 0.0011 %	
Set-mix (LSR at MWPM $p_{\text{th}}$ )	NT		0.8292 $\pm$ 0.0021		NT		NT		NT		0.8465 $\pm$ 0.0019		0.8348 $\pm$ 0.0019		0.7929 $\pm$ 0.0032	
Set-mix (optimal $t_{\text{cut}}$ completion in %)	NT		99.9 %		NT		NT		NT		100 %		99.80 %		99.00 %	
Set-mix EGE ( $t^*$ )	NT		423		NT		NT		NT		4823		366		98	
Set-mix ( $t_{\text{cut}}$ )	NT		300.01		NT		NT		NT		211.21		302.41		474.61	
Set-mix (GHZ fidelity at UF $p_{\text{th}}$ )	NT		99.35 %		NT		NT		NT		99.26 %		99.34 %		99.74	
Set-mix (Stabilizer fidelity at UF $p_{\text{th}}$ )	NT		95.85 %		NT		NT		NT		95.46 %		95.50 %		96.46 %	
Set-D $P_{\text{succ}}^{\text{link}/\text{GHZ}}$	0.0001		0.0423		0.0041		0.0009		0.1		0.4823		0.0366		0.0098	
Set-D ( $p_{\text{th}}$ in %) using MWPM	NT		0.2962 % $\pm$ 0.0019 %		NT		NT		0.1063 % $\pm$ 0.0012 %		0.3612 % $\pm$ 0.0012 %		0.3180 % $\pm$ 0.0010 %		0.0898 % $\pm$ 0.0023 %	
Set-D ( $p_{\text{th}}$ in %) using UF	NT		0.2877 % $\pm$ 0.0035 %		NT		NT		0.0981 % $\pm$ 0.0007 %		0.3528 % $\pm$ 0.0010 %		0.3079 % $\pm$ 0.0009 %		0.0694 % $\pm$ 0.0021 %	
Set-D (LSR at MWPM $p_{\text{th}}$ )	NT		0.8473 $\pm$ 0.0040		NT		NT		0.8695 $\pm$ 0.0038		0.8506 $\pm$ 0.0026		0.8561 $\pm$ 0.0020		0.8761 $\pm$ 0.0039	
Set-D (optimal $t_{\text{cut}}$ completion in %)	NT		99.777 %		NT		NT		99.135 %		99.998 %		99.55 %		98.705 %	
Set-D EGE ( $t^*$ )	NT		846		NT		NT		2000		9646		732		196	
Set-D ( $t_{\text{cut}}$ in s)	NT		0.0065841		NT		NT		0.0467120		0.0017201		0.0065841		0.0163121	
Set-D (GHZ fidelity at UF $p_{\text{th}}$ )	NT		99.30 %		NT		NT		-		99.25 %		99.29 %		99.60 %	
Set-D (Stabilizer fidelity at UF $p_{\text{th}}$ )	NT		95.54 %		NT		NT		95.65 %		95.40 %		95.04 %		95.91 %	

FIG. 29. Weight-3 full threshold simulations data. We give code thresholds for each architecture and scheme using two decoders, success probabilities, entanglement generation efficiency, cut-off times, GHZ, and stabilizer fidelity. NT denotes no threshold.

- [1] M. A. Nielsen and I. L. Chuang, *Quantum Computation and Quantum Information: 10th Anniversary Edition* (Cambridge University Press, 2010).
- [2] J. Preskill, *Quantum* **2**, 79 (2018).
- [3] A. Clerk, 61quantum noise and quantum measurement (2014).
- [4] K. Hornberger, Introduction to decoherence theory, in *Entanglement and Decoherence: Foundations and Modern Trends*, edited by A. Buchleitner, C. Viviescas, and M. Tiersch (Springer Berlin Heidelberg, Berlin, Heidelberg, 2009) pp. 221–276.
- [5] D. J. Reilly, Challenges in scaling-up the control interface of a quantum computer (2019), arXiv:1912.05114 [quant-ph].
- [6] R. Acharya, I. Aleiner, R. Allen, T. I. Andersen, M. Ansmann, F. Arute, K. Arya, A. Asfaw, J. Atalaya, R. Babush, D. Bacon, J. C. Bardin, J. Basso, A. Bengtsson, S. Boixo, G. Bortoli, A. Bourassa, J. Bovaird, L. Brill, M. Broughton, B. B. Buckley, D. A. Buell, T. Burger, B. Burkett, N. Bushnell, Y. Chen, Z. Chen, B. Chiaro, J. Cogan, R. Collins, P. Conner, W. Courtney, A. L. Crook, B. Curtin, D. M. Debroy, A. Del Toro Barba, S. Demura, A. Dunsworth, D. Eppens, C. Erickson, L. Faoro, E. Farhi, R. Fatemi, L. Flores Burgos, E. Forati, A. G. Fowler, B. Foxen, W. Giang, C. Gidney, D. Gilboa, M. Giustina, A. Grajales Dau, J. A. Gross, S. Habegger, M. C. Hamilton, M. P. Harrigan, S. D. Harrington, O. Higgott, J. Hilton, M. Hoffmann, S. Hong, T. Huang, A. Huff, W. J. Huggins, L. B. Ioffe, S. V. Isakov, J. Iveland, E. Jeffrey, Z. Jiang, C. Jones, P. Juhas, D. Kafri, K. Kechedzhi, J. Kelly, T. Khattar, M. Khezri, M. Kieferová, S. Kim, A. Kitaev, P. V. Klimov, A. R. Klots, A. N. Korotkov, F. Kostritsa, J. M. Kreikebaum, D. Landhuis, P. Laptev, K.-M. Lau, L. Laws, J. Lee, K. Lee, B. J. Lester, A. Lill, W. Liu, A. Locharla, E. Lucero, F. D. Malone, J. Marshall, O. Martin, J. R. McClean, T. McCourt, M. McEwen, A. Megrant, B. Meurer Costa, X. Mi, K. C. Miao, M. Mohseni, S. Montazeri, A. Morvan, E. Mount, W. Mruczkiewicz, O. Naaman, M. Neeley, C. Neill, A. Nersisyan, H. Neven, M. Newman, J. H. Ng, A. Nguyen, M. Nguyen, M. Y. Niu, T. E. O’Brien, A. Opremcak, J. Platt, A. Petukhov, R. Potter, L. P. Pryadko, C. Quintana, P. Roushan, N. C. Rubin, N. Saei, D. Sank, K. Sankaragomathi, K. J. Satzinger, H. F. Schurkus, C. Schuster, M. J. Shearn, A. Shorter, V. Shvarts, J. Skrzynny, V. Smelyanskiy, W. C. Smith, G. Sterling, D. Strain, M. Szalay, A. Torres, G. Vidal, B. Villalonga, C. Vollgraf Heidweiller, T. White, C. Xing, Z. J. Yao, P. Yeh, J. Yoo, G. Young, A. Zalcman, Y. Zhang, N. Zhu, and G. Q. AI, *Nature* **614**, 676 (2023).
- [7] L. Gyongyosi and S. Imre, *Scientific Reports* **11**, 5172 (2021).
- [8] S. J. Devitt, W. J. Munro, and K. Nemoto, *Reports on Progress in Physics* **76**, 076001 (2013).
- [9] J. Roffe, *Contemporary Physics* **60**, 226–245 (2019).
- [10] D. Bluvstein, S. J. Evered, A. A. Geim, S. H. Li, H. Zhou, T. Manovitz, S. Ebadi, M. Cain, M. Kalinowski, D. Hangleiter, J. P. Bonilla Ataides, N. Maskara, I. Cong, X. Gao, P. Sales Rodriguez, T. Karolyshyn, G. Semeghini, M. J. Gullans, M. Greiner, V. Vuletić, and M. D. Lukin, *Nature* **626**, 58 (2024).
- [11] T. Figueiredo Roque, A. A. Clerk, and H. Ribeiro, *npj Quantum Information* **7**, 28 (2021).
- [12] S. J. Evered, D. Bluvstein, M. Kalinowski, S. Ebadi, T. Manovitz, H. Zhou, S. H. Li, A. A. Geim, T. T. Wang, N. Maskara, H. Levine, G. Semeghini, M. Greiner, V. Vuletić, and M. D. Lukin, *Nature* **622**, 268 (2023).
- [13] R. VAN METER, T. D. LADD, A. G. FOWLER, and Y. YAMAMOTO, *International Journal of Quantum Information* **08**, 295 (2010).
- [14] J. I. Cirac, A. K. Ekert, S. F. Huelga, and C. Macchiavello, *Phys. Rev. A* **59**, 4249 (1999).
- [15] M. Caleffi, M. Amoretti, D. Ferrari, D. Cuomo, J. Iliano, A. Manzalini, and A. S. Cacciapuoti, Distributed quantum computing: a survey (2022), arXiv:2212.10609 [quant-ph].
- [16] R. Van Meter and D. Horsman, *Commun. ACM* **56**, 84–93 (2013).
- [17] D. Ferrari, S. Carretta, and M. Amoretti, *IEEE Transactions on Quantum Engineering* **4**, 1 (2023).
- [18] D. Awschalom, K. K. Berggren, H. Bernien, S. Bhave, L. D. Carr, P. Davids, S. E. Economou, D. Englund, A. Faraon, M. Fejer, S. Guha, M. V. Gustafsson, E. Hu, L. Jiang, J. Kim, B. Korzh, P. Kumar, P. G. Kwiat, M. Lončar, M. D. Lukin, D. A. Miller, C. Monroe, S. W. Nam, P. Narang, J. S. Orcutt, M. G. Raymer, A. H. Safavi-Naeini, M. Spiropulu, K. Srinivasan, S. Sun, J. Vučković, E. Waks, R. Walsworth, A. M. Weiner, and Z. Zhang, *PRX Quantum* **2**, 017002 (2021).
- [19] N. H. Nickerson, Y. Li, and S. C. Benjamin, *Nature Communications* **4**, 1756 (2013).
- [20] S. Bravyi, O. Dial, J. M. Gambetta, D. Gil, and Z. Nazario, *Journal of Applied Physics* **132**, 160902 (2022), [https://pubs.aip.org/aip/jap/article-pdf/doi/10.1063/5.0082975/19808793/160902\\_1\\_online.pdf](https://pubs.aip.org/aip/jap/article-pdf/doi/10.1063/5.0082975/19808793/160902_1_online.pdf).
- [21] J. Ramette, J. Sinclair, Z. Vendeiro, A. Rudelis, M. Cetina, and V. Vuletić, *PRX Quantum* **3**, 010344 (2022).
- [22] Y. Li and J. Thompson, High-rate and high-fidelity modular interconnects between neutral atom quantum processors (2024), arXiv:2401.04075 [quant-ph].
- [23] L. Li, L. D. Santis, I. B. W. Harris, K. C. Chen, Y. Gao, I. Christen, H. Choi, M. Trusheim, Y. Song, C. Errando-Herranz, J. Du, Y. Hu, G. Clark, M. I. Ibrahim, G. Gilbert, R. Han, and D. Englund, *Nature* 10.1038/s41586-024-07371-7 (2024).
- [24] F. Afzal, M. Akhlaghi, S. J. Beale, O. Bedroya, K. Bell, L. Bergeron, K. Bonsma-Fisher, P. Bychkova, Z. M. E. Chaisson, C. Chartrand, C. Clear, A. Darcie, A. DeAbreu, C. DeLisle, L. A. Duncan, C. D. Smith, J. Dunn, A. Ebrahimi, N. Evetts, D. F. Pinheiro, P. Fuentes, T. Georgiou, B. Guha, R. Haenel, D. Higginbottom, D. M. Jackson, N. Jahed, A. Khorshidmahmad, P. K. Shandilya, A. T. K. Kurkjian, N. Lauk, N. R. Lee-Hone, E. Lin, R. Litynsky, D. Lock, L. Ma, I. MacGilp, E. R. MacQuarrie, A. Mar, A. M. Khah, A. Matias, E. Meyer-Scott, C. P. Michaels, J. Motira, N. K. Noori, E. Ospadov, E. Patel, A. Patscheider, D. Paulson, A. Petruk, A. L. Ravindranath, B. Reznichenko, M. Ruether, J. Ruscica, K. Saxena, Z. Schaller, A. Seidlitz, J. Senger, Y. S. Lee, O. Sevoyan, S. Sim-

- mons, O. Soykal, L. Stott, Q. Tran, S. Tserkis, A. Ulhaq, W. Vine, R. Weeks, G. Wolfowicz, and I. Yoneda, Distributed quantum computing in silicon (2024), arXiv:2406.01704 [quant-ph].
- [25] S. de Bone, P. Möller, C. E. Bradley, T. H. Taminiau, and D. Elkouss, Thresholds for the distributed surface code in the presence of memory decoherence (2024), arXiv:2401.10770 [quant-ph].
- [26] J. Ramette, J. Sinclair, N. P. Breuckmann, and V. Vuletić, Fault-tolerant connection of error-corrected qubits with noisy links (2023), arXiv:2302.01296 [quant-ph].
- [27] H. K. Beukers, M. Pasini, H. Choi, D. Englund, R. Hanson, and J. Borregaard, PRX Quantum **5**, 010202 (2024).
- [28] B. M. Terhal, Rev. Mod. Phys. **87**, 307 (2015).
- [29] N. P. Breuckmann and J. N. Eberhardt, PRX Quantum **2**, 040101 (2021).
- [30] M. H. Abobeih, Y. Wang, J. Randall, S. J. H. Loenen, C. E. Bradley, M. Markham, D. J. Twitchen, B. M. Terhal, and T. H. Taminiau, Nature **606**, 884 (2022).
- [31] C. E. Bradley, S. W. de Bone, P. F. W. Möller, S. Baier, M. J. Degen, S. J. H. Loenen, H. P. Bartling, M. Markham, D. J. Twitchen, R. Hanson, D. Elkouss, and T. H. Taminiau, npj Quantum Information **8**, 122 (2022).
- [32] A. Sipahigil, R. E. Evans, D. D. Sukachev, M. J. Burek, J. Borregaard, M. K. Bhaskar, C. T. Nguyen, J. L. Pacheco, H. A. Atikian, C. Meuwly, R. M. Camacho, F. Jelezko, E. Bielejec, H. Park, M. Lončar, and M. D. Lukin, Science **354**, 847 (2016), <https://www.science.org/doi/pdf/10.1126/science.aah6875>.
- [33] D. D. Sukachev, A. Sipahigil, C. T. Nguyen, M. K. Bhaskar, R. E. Evans, F. Jelezko, and M. D. Lukin, Phys. Rev. Lett. **119**, 223602 (2017).
- [34] C. T. Nguyen, D. D. Sukachev, M. K. Bhaskar, B. Machielse, D. S. Levonian, E. N. Knall, P. Stroganov, C. Chia, M. J. Burek, R. Riedinger, H. Park, M. Lončar, and M. D. Lukin, Phys. Rev. B **100**, 165428 (2019).
- [35] C. T. Nguyen, D. D. Sukachev, M. K. Bhaskar, B. Machielse, D. S. Levonian, E. N. Knall, P. Stroganov, R. Riedinger, H. Park, M. Lončar, and M. D. Lukin, Phys. Rev. Lett. **123**, 183602 (2019).
- [36] P.-J. Stas, Y. Q. Huan, B. Machielse, E. N. Knall, A. Suleymanzade, B. Pingault, M. Sutula, S. W. Ding, C. M. Knaut, D. R. Assumpcao, Y.-C. Wei, M. K. Bhaskar, R. Riedinger, D. D. Sukachev, H. Park, M. Lončar, D. S. Levonian, and M. D. Lukin, Science **378**, 557 (2022), <https://www.science.org/doi/pdf/10.1126/science.add9771>.
- [37] C. M. Knaut, A. Suleymanzade, Y. C. Wei, D. R. Assumpcao, P. J. Stas, Y. Q. Huan, B. Machielse, E. N. Knall, M. Sutula, G. Baranes, N. Sinclair, C. De-Eknamkul, D. S. Levonian, M. K. Bhaskar, H. Park, M. Lončar, and M. D. Lukin, Nature **629**, 573 (2024).
- [38] T. Iwasaki, Y. Miyamoto, T. Taniguchi, P. Siyushev, M. H. Metsch, F. Jelezko, and M. Hatano, Phys. Rev. Lett. **119**, 253601 (2017).
- [39] A. E. Rugar, S. Aghaeimeibodi, D. Riedel, C. Dory, H. Lu, P. J. McQuade, Z.-X. Shen, N. A. Melosh, and J. Vučković, Phys. Rev. X **11**, 031021 (2021).
- [40] R. Debroux, C. P. Michaels, C. M. Purser, N. Wan, M. E. Trusheim, J. Arjona Martínez, R. A. Parker, A. M. Stramma, K. C. Chen, L. de Santis, E. M. Alexeev, A. C. Ferrari, D. Englund, D. A. Gangloff, and M. Atatüre, Phys. Rev. X **11**, 041041 (2021).
- [41] S. Simmons, PRX Quantum **5**, 010102 (2024).
- [42] A. Kitaev, Annals of Physics **303**, 2 (2003).
- [43] S. B. Bravyi and A. Y. Kitaev, Quantum codes on a lattice with boundary (1998), arXiv:quant-ph/9811052 [quant-ph].
- [44] E. Dennis, A. Kitaev, A. Landahl, and J. Preskill, Journal of Mathematical Physics **43**, 4452 (2002), [https://pubs.aip.org/aip/jmp/article-pdf/43/9/4452/19183135/4452\\_1\\_online.pdf](https://pubs.aip.org/aip/jmp/article-pdf/43/9/4452/19183135/4452_1_online.pdf).
- [45] A. G. Fowler, M. Mariantoni, J. M. Martinis, and A. N. Cleland, Phys. Rev. A **86**, 032324 (2012).
- [46] H. Bernien, B. Hensen, W. Pfaff, G. Koolstra, M. S. Blok, L. Robledo, T. H. Taminiau, M. Markham, D. J. Twitchen, L. Childress, and R. Hanson, Nature **497**, 86 (2013).
- [47] S. Welte, B. Hacker, S. Daiss, S. Ritter, and G. Rempe, Phys. Rev. X **8**, 011018 (2018).
- [48] B. Heim, K. M. Svore, and M. B. Hastings, Optimal circuit-level decoding for surface codes (2016), arXiv:1609.06373 [quant-ph].
- [49] M. Ruf, M. Weaver, S. van Dam, and R. Hanson, Phys. Rev. Appl. **15**, 024049 (2021).
- [50] E. Dennis, A. Kitaev, A. Landahl, and J. Preskill, Journal of Mathematical Physics **43**, 4452–4505 (2002).
- [51] A. Yimsiriwattana and S. J. L. J. au2, Generalized ghz states and distributed quantum computing (2004), arXiv:quant-ph/0402148 [quant-ph].
- [52] D. J. Reilly, npj Quantum Information **1**, 15011 (2015).
- [53] A. Gold, J. P. Paquette, A. Stockklauser, M. J. Reagor, M. S. Alam, A. Bestwick, N. Didier, A. Nersisyan, F. Oruc, A. Razavi, B. Scharmann, E. A. Sete, B. Sur, D. Venturelli, C. J. Winkleblack, F. Wudarski, M. Harburn, and C. Rigetti, npj Quantum Information **7**, 142 (2021).
- [54] O. Crawford, J. R. Cruise, N. Mertig, and M. F. Gonzalez-Zalba, npj Quantum Information **9**, 13 (2023).
- [55] Y. Tomita and K. M. Svore, Phys. Rev. A **90**, 062320 (2014).
- [56] R. Chao and B. W. Reichardt, Phys. Rev. Lett. **121**, 050502 (2018).
- [57] C. Cabillo, J. I. Cirac, P. García-Fernández, and P. Zoller, Phys. Rev. A **59**, 1025 (1999).
- [58] S. D. Barrett and P. Kok, Phys. Rev. A **71**, 060310 (2005).
- [59] L. Childress and R. Hanson, MRS Bulletin **38**, 134 (2013).
- [60] R. E. Evans, M. K. Bhaskar, D. D. Sukachev, C. T. Nguyen, A. Sipahigil, M. J. Burek, B. Machielse, G. H. Zhang, A. S. Zibrov, E. Bielejec, *et al.*, Science **362**, 662 (2018).
- [61] G. Thiering and A. Gali, Physical Review X **8**, 021063 (2018).
- [62] S. Castelletto and A. Boretti, Journal of Physics: Photonics **2**, 022001 (2020).
- [63] M. Radulaski, M. Widmann, M. Niethammer, J. L. Zhang, S.-Y. Lee, T. Rendler, K. G. Lagoudakis, N. T. Son, E. Janzen, T. Ohshima, *et al.*, Nano letters **17**, 1782 (2017).
- [64] S. Ritter, C. Nölleke, C. Hahn, A. Reiserer, A. Neuzner, M. Uphoff, M. Mücke, E. Figueroa, J. Bochmann, and G. Rempe, Nature **484**, 195 (2012).
- [65] A. Reiserer and G. Rempe, Reviews of Modern Physics **87**, 1379 (2015).
- [66] S. Welte, B. Hacker, S. Daiss, S. Ritter, and G. Rempe,

- Phys. Rev. Lett. **118**, 210503 (2017).
- [67] A. S. Sørensen and K. Mølmer, Phys. Rev. Lett. **90**, 127903 (2003).
- [68] B. Hensen, H. Bernien, A. E. Dréau, A. Reiserer, N. Kalb, M. S. Blok, J. Ruitenber, R. F. L. Vermeulen, R. N. Schouten, C. Abellán, W. Amaya, V. Pruneri, M. W. Mitchell, M. Markham, D. J. Twitchen, D. Elkouss, S. Wehner, T. H. Taminiau, and R. Hanson, Nature **526**, 682 (2015).
- [69] F. Rozpędek, R. Yehia, K. Goodenough, M. Ruf, P. C. Humphreys, R. Hanson, S. Wehner, and D. Elkouss, Phys. Rev. A **99**, 052330 (2019).
- [70] P. C. Humphreys, N. Kalb, J. P. J. Morits, R. N. Schouten, R. F. L. Vermeulen, D. J. Twitchen, M. Markham, and R. Hanson, Nature **558**, 268 (2018).
- [71] M. Pompili, S. L. N. Hermans, S. Baier, H. K. C. Beukers, P. C. Humphreys, R. N. Schouten, R. F. L. Vermeulen, M. J. Tiggelman, L. dos Santos Martins, B. Dirkse, S. Wehner, and R. Hanson, Science **372**, 259 (2021).
- [72] A. Dahlberg, M. Skrzypczyk, T. Coopmans, L. Wubben, F. Rozpundefineddek, M. Pompili, A. Stolk, P. Pawełczak, R. Knegjens, J. de Oliveira Filho, R. Hanson, and S. Wehner, in *Proceedings of the ACM Special Interest Group on Data Communication, SIGCOMM '19* (Association for Computing Machinery, New York, NY, USA, 2019) p. 159–173.
- [73] T. Coopmans, R. Knegjens, A. Dahlberg, D. Maier, L. Nijsten, J. de Oliveira Filho, M. Papendrecht, J. Rabbie, F. Rozpędek, M. Skrzypczyk, L. Wubben, W. de Jong, D. Podareanu, A. Torres-Knoop, D. Elkouss, and S. Wehner, Communications Physics **4**, 164 (2021).
- [74] M. K. Bhaskar, R. Riedinger, B. Machielse, D. S. Levonian, C. T. Nguyen, E. N. Knall, H. Park, D. Englund, M. Lončar, D. D. Sukachev, and M. D. Lukin, Nature **580**, 60 (2020).
- [75] N. Delfosse and N. H. Nickerson, Quantum **5**, 595 (2021).
- [76] R. Chao and B. W. Reichardt, PRX Quantum **1**, 010302 (2020).
- [77] C. Chamberland, G. Zhu, T. J. Yoder, J. B. Hertzberg, and A. W. Cross, Phys. Rev. X **10**, 011022 (2020).
- [78] S. Bravyi, A. W. Cross, J. M. Gambetta, D. Maslov, P. Rall, and T. J. Yoder, Nature **627**, 778 (2024).
- [79] C. Gidney and M. Ekerå, Quantum **5**, 433 (2021).
- [80] S. Singh, F. Gu, S. de Bone, E. Villaseñor, D. Elkouss, and J. Borregaard, Source code and data underlying the publication “modular architectures and entanglement schemes for error-corrected distributed quantum computation”; (2024).
- [81] O. Higgott, T. C. Bohdanowicz, A. Kubica, S. T. Flammia, and E. T. Campbell, Phys. Rev. X **13**, 031007 (2023).
- [82] N. H. Nickerson, J. F. Fitzsimons, and S. C. Benjamin, Phys. Rev. X **4**, 041041 (2014).
- [83] A. Jamiolkowski, Reports on Mathematical Physics **3**, 275 (1972).
- [84] M. McEwen, D. Bacon, and C. Gidney, Quantum **7**, 1172 (2023).
- [85] S. de Bone, R. Ouyang, K. Goodenough, and D. Elkouss, IEEE Transactions on Quantum Engineering **1**, 1 (2020).
- [86] A. Reiserer and G. Rempe, Rev. Mod. Phys. **87**, 1379 (2015).
- [87] D. E. Chang, A. S. Sørensen, E. A. Demler, and M. D. Lukin, Nature physics **3**, 807 (2017).
- [88] C. E. Bradley, J. Randall, M. H. Abobeih, R. C. Berrevoets, M. J. Degen, M. A. Bakker, M. Markham, D. J. Twitchen, and T. H. Taminiau, Phys. Rev. X **9**, 031045 (2019).
- [89] C. Wang, J. Harrington, and J. Preskill, Annals of Physics **303**, 31 (2003).
- [90] J. Edmonds, Canadian Journal of Mathematics **17**, 449–467 (1965).